SEPARATION OF OXYGEN ARGON MIXTURE BY PRESSURE SWING ADSORPTION (PSA)

XU JIN

NATIONAL UNIVERSITY OF SINGAPORE

2003

SEPARATION OF OXYGEN ARGON MIXTURE BY PRESSURE SWING ADSORPTION (PSA)

XU JIN
(*B. Eng, Zhejiang University*)

A THESIS SUBMITTED

FOR THE DEGREE OF MASTER OF ENGINEERING

DEPARTMENT OF CHEMICAL AND ENVIRONMENTAL ENGINEERING

NATIONAL UNIVERSITY OF SINGAPORE

2003

Acknowledgements

I would like to take this opportunity to thank those people who have helped me during my Master of Engineering study in the National University of Singapore.

Firstly, I would like to express my sincere gratitude to Assoc. Prof. Shamsuzzaman Farooq for his encouragement, trust and consideration throughout my research work. His mastery over the subject and meticulous supervision helped me solve many difficult problems I have faced. His exemplary personality has influenced me a lot and will surely be continually influencing me in the future.

I owe thanks to the instruction of Dr. Malek, whose patient demonstration about the PSA experiments and valuable advice in the simulation work were very helpful for my research study.

I appreciate the assistance provided by my labmates and technicians. Also appreciated are the support and help from my parents and my friends.

Financial support from the National University of Singapore in form of research scholarship is gratefully acknowledged.

No word can express my loving gratitude to my wife for her love, support and encouragement.

Table of Contents

Summary

Four potential adsorbents for the separation of oxygen-argon mixture by kinetically controlled PSA were compared based on adsorption equilibrium and kinetics measured in the linear range. The equilibrium and kinetics of argon in the chosen adsorbent, Takeda II Carbon Molecular Sieve (CMS), were measured in the pressure range of 0 to 6 bar. Volumetric method was used in all the measurements. The linear range data were verified with breakthrough experiments. The parameters of the Langmuir model were extracted by fitting experimental isotherms at different temperatures. Similarly, the transport model parameters were obtained by fitting the fractional uptake curves at different levels of adsorbate loading. PSA experiments were carried out to concentrate argon from an oxygen-argon mixture (95: 5 based on mole fraction) using a single-bed, 3-step cycle operated in $0-3$ atm pressure range. PSA simulations were conducted using a bidispersed PSA model including the dual transport resistance with strongly concentration dependent thermodynamically corrected transport parameters in the CMS micropores to capture the experimental phenomena of the system featured by kinetically controlled separation, high proportion of faster component in the feed mixture and vacuum operation. The performance of the single-bed, 3-step cycle at different operation conditions was systematically studied using the PSA simulation model validated by experimental results. The feasibility of other two cycles was also studied through numerical simulation and the effects of different operating conditions on these cycles were investigated.

Nomenclature

A, AX, AY -collocation matrices for the first derivative

A_B -adsorption bed area [cm^2]

a_1, a_2 -constants in Eq (5.25)

b -Langmuir constants in equilibrium isotherm equations [cc/mmol]

b_0 -preexponential constant for temperature dependence q b_0 [cc/mmol]

B -collocation matrix for the second derivative

C -total concentration in the fluid phase [mmol/cm^3]

c_p -concentration in the macropores [mmol/ cm^3]

C -total concentration in the gas phase [mmol/ cm^3]

d_p -particle diameter [cm]

D -diffusivity [cm^2/s]

D_c -micropore diffusivity [cm^2/s]

D_L -axial dispersion coefficient [cm^2/s]

D_m -molecular diffusivity [cm^2/s]

D_p -macropore diffusivity [cm^2/s]

E_D, E_k -activation energy [kcal/mol]

F -flow rate [cm^3/s at 1 atm]

ΔH -adsorption heat [kcal/mol]

K -Henry's law constant based on particle volume [mmol/ml]

k_b -mass transfer coefficient [s^{-1}]

K_c -Henry's law constant based on micropore volume

k_f -fluid phase mass transfer coefficient [s^{-1}]

L -column length [cm]; constant in Eq (2.39)

M	-molecular weight [g/mol]
P	-pressure [bar]
P_H	-the highest pressure in PSA operation [bar]
P_L	-the lowest pressure in PSA operation [bar]
q_c	-concentration in the micropores [mmol/ml]
$\bar{q}$	-average concentration in the micropores [mmol/ml]
q_s	-saturated concentration in the Langmuir model
$\bar{\bar{q}}$	-average concentration in the adsorbent particles [mmol/ml]
r_c	-micropore radius [cm]
R	-macropore radius [cm]; universal gas constant [1.987 cal/mol/K]
R_p	-adsorbent particle radius [cm]
t	-time [s]
T	-dimensionless time
$\bar{t}$	-mean residence time [s]
T_0	-temperature [K]
v	-gas velocity [cm/s]
V	-volume [cm^3]
x	-mole fraction in the fluid phase
X	-constant of the solenoid valve in the volumetric setup [mol/s/bar]
z	-axial position in the column [cm] (0: the feed end; L: the product end)

Greek letters

β	-dimensionless constant accounting for the strong concentration dependence of the thermodynamically corrected transport parameters

ρ_g	-gas density [g/cm^3]
ρ_s	-particle density [g/cm^3]
ε	-bed voidage
ε_p	-particle voidage
λ	-constant in Eq (1.6)
θ	-dimensionless adsorbate loading

Subscript

0	-initial value
A	-component A
a, ads	-adsorbent; adsorption
B	-component B
b, barrier	-barrier model
bd	-blowdown
c	-micropore
des	-desorption
e	-exit
hp	-high pressure adsorption
i	-component *i*
p, pore	-pore model
pr	-pressurization
r	-raffinate
t	-at time, *t*
∞	-infinity

List of Figure

List of Tables

Chapter 1   Introduction

1.1 Pressure Swing Adsorption

Any separation must be based on some property differences among the components in the mixture to be separated. Adsorption processes exploit adsorbents that preferentially adsorb one component (or a family of related components) over the other(s). Any adsorption process involves two essential steps, namely, the adsorption step and the regeneration step. During the adsorption step, the preferentially adsorbed component goes into the adsorbent particles while the less adsorbed component is concentrated in the fluid phase and is collected as the "raffinate" product. During the regeneration step, the adsorbed component is removed to clean the adsorbent particles for use in the next cycle. The regeneration step may also be used to collect "extract" product (normally at the feed end of the bed) enriched in the more strongly adsorbed component.
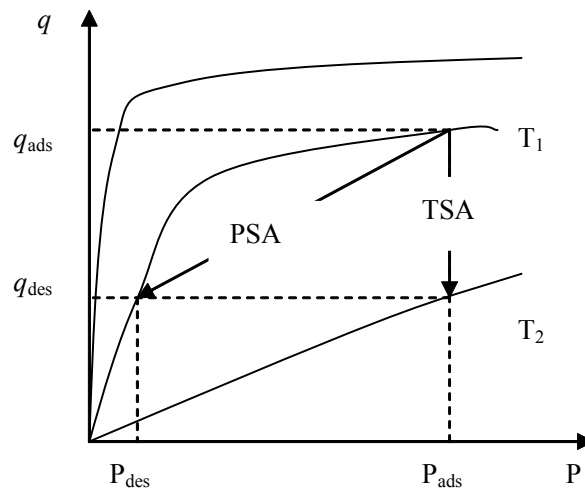
Figure 1.1 The concepts of PSA and TSA.

Regeneration can be achieved by increasing the temperature or lowering the (total or partial) pressure, which is illustrated in Figure 1.1. As such, adsorption

separation processes operate either between two temperatures or between two pressures and fall into two major classes, namely, Thermal Swing Adsorption (TSA) and Pressure Swing Adsorption (PSA). Inert purge is also used in almost all TSA processes, which enhances regeneration by reducing partial pressure of the strongly adsorbed component. Nevertheless, PSA is more widely used because, as compared to TSA, it has the advantage that the pressure can be changed much more rapidly than the temperature, hence making possible much faster cycle, which increases the productivity of the adsorbent bed. However, the application of PSA processes is not suitable for very strongly adsorbed species, the efficient removal of which requires an uneconomically high vacuum. The general features of PSA processes together with the advantages and limitations have been discussed in detail by Ruthven et al. (1994a)

Air separation, air drying and hydrogen purification, which were foreseen and demonstrated by Skarstrom who invented PSA in 1950s, remain the first three most important practical applications of this technology. Some new processes such as carbon dioxide recovery and natural gas purification are gaining increased acceptance (Ruthven et al. 1994a). Most recently, attempts have been made to concentrate trace components such as rare gases in air (Yoshida et al., 1997), SO_2 in air (Kikkinides and Yang, 1991) and H_2 in He (Ruthven and Farooq, 1994b). It may be expected that accompanied with the continuous emergence of new adsorbents and deeper study of cycle operations, PSA processes will be more and more versatile and have more and more applications for gas separation.

1.2 Separation Factor and Selectivity

The adsorptive selectivity may depend on either a difference in equilibrium capacities or a difference in diffusion rates. The separation factor is normally defined as:

$$\alpha_{AB} \equiv \frac{q_A/c_A}{q_B/c_B} \tag{1.1}$$

where *A*, *B* denote two components, *c* and *q* are the concentrations in the fluid phase and adsorbed phase, respectively. For an equilibrium controlled separation and for a linear or Langmuir system, this factor is simply equivalent to the ratio of Henry's law constants.

In the case of a kinetically controlled process, the selectivity depends on both equilibrium and kinetic effects. When the kinetics is controlled by pore diffusion and equilibrium follows Henry's law, kinetic selectivity at short time region is given by the following equation (Ruthven et al., 1994a):

$$\left(\alpha_K\right)_{pore} = \frac{K_A}{K_B}\sqrt{\frac{D_A}{D_B}} \tag{1.2}$$

where *K* is Henry's law constant and *D* is diffusivity. Following the same approach, it can be easily shown that for a linear driving force (LDF) model the kinetic selectivity is given by Eq (1.3):

$$\left(\alpha_K\right)_{barrier} = \frac{K_A}{K_B}\frac{k_A}{k_B} \tag{1.3}$$

where *k* is LDF coefficient. Clearly, kinetic selectivity depends on both equilibrium and kinetic parameters. Details of equilibrium and kinetic models are discussed in Chapters 2 and 3.

1.3 Oxygen and Argon Separation

Commercialized PSA processes for oxygen production from air are normally equilibrium controlled using some suitable adsorbents that preferentially adsorb nitrogen to oxygen. The oxygen product purity in such a process is typically limited to 95% by the presence of argon, which accounts for 1% in feed air and shows practically the same adsorption equilibrium behavior as oxygen on all adsorbents used for equilibrium controlled PSA air separation. Some relative physical properties of oxygen and argon are listed in Table 1.1. Table1.2 gives some reported equilibrium data of N_2, O_2 and Ar on several commercially used adsorbents.

Table 1.1 Some relative physical properties of argon and oxygen.

	P	ε/κ	σ	QM
N_2	1.76	95	3.7	0.31
O_2	1.60	118	3.5	<0.11
Ar	1.64	121	3.4	0

P :   polarizability in $10^{-24} cm^3$
ε/κ: Lennard_Jones force constant in K
σ: collision diameter in Å
QM :   quadrupole moment in $Å^2$

Table 1.2 Equilibrium data of atmospheric gases on some commercially
used adsorbents at 303 K.

Adsorbent	Henry's Law Constant, *K*			Equilibrium Separation Factor	
	N_2	O_2	Ar	N_2/O_2	O_2/Ar
CaX[a]	39	4.3	3.5	9.0	1.3
SrX[a]	29	5.5	4.0	5.4	1.4
CaY[a]	21	3.1	2.7	6.8	1.1
Ag-mordenite[a]	195	9.8	11.7	20.2	0.83
4A zeolite[b]	4.9	1.4	-	3.5	-
5A zeolite[b]	8.1	2.0	1.6	4.1	1.3
CMS[b]	5.8	5.8	6.1	1.0	0.95

a: dimensionless
b: in mmol/Torr/g

To meet the need for high purity oxygen, for example, in medical uses, in ferrous metal cutting and welding, etc., further removal of argon becomes important. Since the supply of air is almost infinite, the enriched oxygen stream containing ~5% argon is also a source for argon production. Hence, an efficient and economic method for oxygen-argon separation will be of practical significance.

Currently, three methods are commercially used for O_2 and Ar separation. (1) *Cryogenic distillation*: Both high purity O_2 (99.5%) and Ar (99.9%) can be obtained (Xu and Hopkins, 1998) by this method. But since the boiling points of pure oxygen and pure argon are very close, a very high reflux ratio and a large number of theoretical stages are required, which decreases the productivity and increases capital costs. (2) *Catalytic hydrogenation*: O_2 is removed as water by reacting with H_2 and hence O_2 recovery is not possible. Moreover, the addition of hydrogen increases the operating cost. This method is only practical as a polishing step to remove trace or small concentration of O_2 from a crude Ar stream. (3) *Cryogenic adsorption*: The adsorption equilibrium selectivity of oxygen to argon on 4A zeolite becomes sufficiently large at a very low temperature (-150^0C to -190^0C) to enable adsorption separation (Kovak, 1992). However, the process will be highly energy intensive.

It has also been found that O_2 and Ar have different magnetic properties. They are paramagnetic and diamagnetic, respectively. In other words, in a strong magnetic field, the force acting on O_2 molecules is opposite to that acting on Ar atoms. This seems to provide another direction for separating O_2/Ar mixture along which some research work has been reported (Horie et al., 2001). However, the operation in a strong magnetic field requires a complicated system, especially a superconductor as a filter, which must be operated at temperatures lower than 100 K.

For the purification of oxygen by PSA, it is ideal to choose an adsorbent selective to Ar (Ruthven, 1994a). Most commonly used zeolites are mildly oxygen selective (Table 1.1). Probably due to its somewhat higher polarizability, Ar is preferentially adsorbed by silver exchanged zeolites, which generally show relatively higher affinities for the monatomic gases (Boniface and Ruthven, 1993). Silver exchanged zeolite type X (Ag-mordenite) was, therefore, recommended for the separation of Ar from O_2. Although 99% oxygen purity was achieved, the corresponding recovery was only 25% (Kandybin et al., 1995). Such a result is expected for a low separation factor (see Table 1.1).

While an equilibrium-based PSA process will fail to efficiently separate O_2 and Ar because of the near unity separation factor on all known adsorbents, kinetically controlled PSA seems to be promising. It has been shown that in some adsorbents O_2 diffusion is so much faster than that of Ar that they can be used to lead the desired separation.

Hayashi et al. (1996) carried out a 2-stage experimental study with direct air feed using Takeda 3A CMS in the first stage to remove Ar and Ca-X zeolite in the second stage to remove N_2. The purity of O_2 was reported to be 99% with a recovery of 50%. In another study, Hayashi et al. (1985) described an argon process using 5A zeolite to remove N_2 and 3A CMS to remove O_2. It was claimed that the purity of Ar product was 99% with recovery of 40%.

Rege and Yang (2000) theoretically studied the feasibility of separating a 95% O_2 and 5% Ar (mole %) mixture using BF CMS, which was reported to have a higher diffusivity ratio of O_2 to Ar than Takeda CMS. Two different modes of PSA operation, namely a 5-step cycle giving high purity of Ar as product, and a 4-step cycle to obtain high purity O_2 product were suggested. Better results compared to the studies by

Hayashi et al. (1985) were claimed. However, contrary to intuitive expectation at cyclic steady state based on mass conservation, argon concentrations in both "raffinate" product and "extract" product were higher than that in the feed in the 5-step cycle. Although there was another waste stream in this cycle, it cannot still explain the mass balance problem.

The results of experimental study are normally more reliable, but they do not normally represent optimum performance. On the other hand, while simulation can be easily conducted over a wide range for a full search, such results without experimental validation remain doubtful. The best strategy is a combined approach in which the model is first verified with experimental results and then a full search is conducted using the verified simulation model.

1.4 Carbon Molecular Sieves (CMS)

Carbon Molecular Sieve differs from activated carbon mainly in the pore size distribution and surface area. While activated carbon has a broad range of pores, with an average pore diameter typically ~20 Å, CMS has a much narrower pore size distribution, with pore size in the range 3~5 Å. Bergbau-Forschung GmbH (BF) and Takeda Chemical Industries Ltd. are the two leading manufacturers of CMS in the world market. In the literature, these products are identified as BF CMS and Takeda CMS. CMS can be produced from different raw materials by a variety of methods. By carefully controlled carbon deposition onto a microporous substrate, it is possible to create constrictions, which are responsible for separation selectivity, while preserving a high micropore volume, which is responsible for the high adsorption capacity.

The effective structure of CMS is extremely sensitive to the manufacturing conditions. This makes it relatively easy to tailer a CMS for a specific separation. On the other hand, this also brings trouble for CMS study because samples from different

sources may be significantly different. It was reported that the difference exists even from batch to batch (Freitas and Figueiredo, 2000).
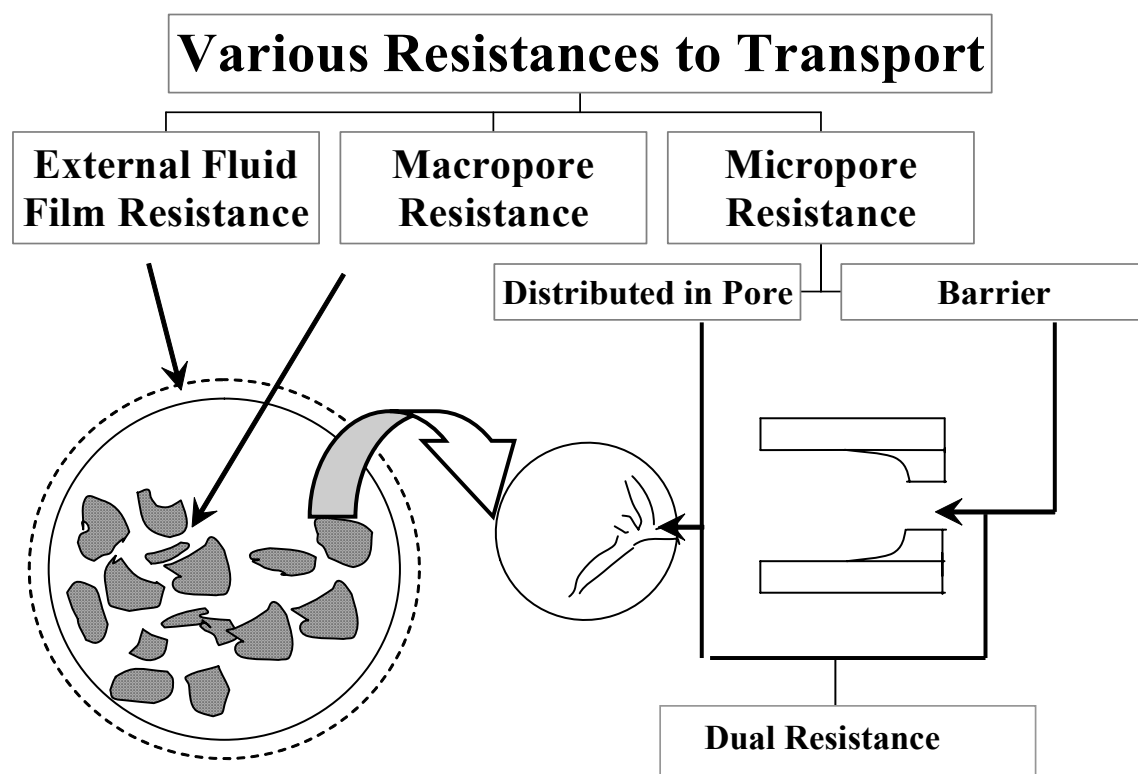
Figure 1.2 Schematic diagram showing various resistances to transport of adsorbate gas in a CMS particle.

CMS has been widely studied and commercially used for air separation by kinetically controlled PSA because of their remarkably high kinetic selectivity between oxygen and nitrogen. An accurate mass transfer model is essential for the simulation of processes based on kinetic selectivity. Figure 1.2 gives various resistances like external film resistance, macropore resistance and micropore resistance that are possible in CMS. While it is generally agreed that in CMS adsorbents, the dominant resistance is in the micropores, three different mechanisms have been suggested for the transport in the micropores: distributed pore interior resistance (pore model), barrier resistance confined at the pore mouth (barrier model) and the combination of both resistances (dual model).

Kawazoe et al. (1974) and Chihara et al. (1978) measured the diffusion of nitrogen and propylene, respectively, in Takeda MSC 5A using pulse chromatographic method. They concluded that the micropore resistance was distributed in the micropore interior. Ruthven et al. (1986, 1992) and Chen et al. (1994) gravimetrically measured the diffusion of oxygen and nitrogen in BF CMS and were able to fit their data with a pore diffusion model. LaCava et al. (1989) used gravimetric and batch column adsorption methods to measure diffusion of oxygen and nitrogen, while Srinivasan et al. (1995) measured the diffusion of the same sorbates using the volumetric method. The manufacturers of the samples used in these studies were, however, not disclosed. In these studies, fit of the barrier resistance model was very clear. Diffusion of oxygen and nitrogen was also measured by Loughlin et al. (1993) in BF CMS using volumetric, gravimetric and pulse chromatographic methods and by Rynders et al. (1997) using isotope exchange technique in Takeda CMS. While the former study advocated a dual resistance model, barrier model fitted the data presented in the latter study. Liu and Ruthven (1996) gravimetrically measured the diffusion of oxygen, nitrogen, argon, methane and carbon dioxide in BF CMS. They found that for oxygen, nitrogen and argon, the data were consistent with distributed pore diffusional resistance. The data for methane was consistent with barrier resistance and carbon dioxide showed transition from barrier resistance control at lower temperatures to diffusion control at higher temperatures. The study showed that for large pore to molecule diameter ratios, diffusion is the main mechanism, while for small ratios surface barrier dominates. They concluded that the results perhaps suggested a dual resistance model with varying importance of the two components depending on pressure and temperature. Reid et al. (1998) have reported linear driving force (equivalent to barrier) model for the uptake of oxygen, nitrogen, argon and krypton on a CMS sample received from Air Products and

Chemicals Inc. Their uptake data for neon, however, followed a dual resistance model. Rutherford and Do (2000) found the uptake of carbon dioxide in a sample of Takeda 5A to be controlled by pore diffusional resistance distributed in the micropore interior. In another study, Nguyen and Do (2000) fitted the uptake of oxygen, argon and nitrogen in a Takeda 3A sample with a dual Langmuir kinetic model.

The reported differences in mechanisms in the studies summarized in the preceding paragraph cannot be linked to the manufacturers of the adsorbent or the adsorbate gas. However, all the studies in which the concentration dependence of micropore diffusivity was explored seem to conform closely with the Darken's equation, which follows from the chemical potential gradient as the driving force for diffusion (Chihara et al., 1978; Kawazeo et al., 1974; Rutherford and Do, 2000; Ruthven, 1992):

$$\frac{D_c}{D_{c0}} = \frac{d\ln c}{d\ln q} \tag{1.4}$$

D_{c0} is called the limiting diffusivity which is the diffusivity in the Henry's law region of the isotherm (i.e., fractional coverage, $\theta \to 0$). For a Langumir isotherm,

$$\frac{D_c}{D_{c0}} = \frac{1}{1-\theta} \tag{1.5}$$

One exception to the above is the study by Chen and Yang (1992), which used kinetic theory approach to obtain:

$$\frac{D_c}{D_{c0}} = \frac{1}{1-(1-\lambda)\theta} \tag{1.6}$$

The reported values of λ for oxygen and nitrogen in a sample of Bergbau_Forschung (BF) CMS were 0.05282 and 0.01287, respectively (Chen et al., 1994). More recently, Wang et al. (2001) have reported that the concentration dependence of the diffusivity of carbon dioxide in a CMS membrane was much stronger than that predicted by Darken's equation.

Liu and Ruthven (1996) found that the barrier coefficient of carbon dioxide transport in BF CMS micropores depended on the adsorbent loading according to the following equation derived from Langmuir kinetic model:

$$\frac{k_b}{k_{b0}} = \frac{1}{1-\theta} \qquad\qquad (1.7)$$

LaCava et al. (1998) had earlier shown that the Langmuir kinetics model was a good useful approximation of the more general slit potential rate model. Analogous to D_{c0} in Eq (1.4), k_{b0} is the limiting barrier coefficient, which is obtained from uptake measured in the linear range of the isotherm. Both D_{c0} and k_{b0} have the usual exponential temperature dependence. The same form of concentration dependence of barrier coefficient may also be derived from the chemical potential gradient as the driving force for diffusion with adsorption equilibrium represented by Langmuir isotherm (Srinivasan et al. 1995).

For a Langmuir isotherm, Eq (1.7) may also be written as:

$$\frac{k_b}{k_{b0}} = 1 + bc \qquad\qquad (1.8)$$

where c is the adsorbate concentration in the gas phase and b is the Langmuir isotherm constant. A number of studies (Liu and Ruthven, 1996; Reid and Thomas, 2001:

Rynders et al., 1997) have reported increasing barrier coefficients of oxygen and nitrogen in CMS with increasing sorbate partial pressures.

In order to reconcile the disagreement on the transport mechanism of gases in CMS micropores, a detailed study was undertaken in this laboratory. In that study (Huang et al., 2003a; 2003b), adsorption and diffusion of oxygen, nitrogen, carbon dioxide and methane were measured in a BF CMS sample and in a Takeda CMS sample (designated as Takeda I). Similar measurements were also made for oxygen and nitrogen in a second Takeda CMS sample (designated as Takeda II).

A dual resistance model was shown to be the desirable unified approach that fitted the experimental results in the entire range covered in that study. As expected, the two transport parameters of the dual resistance model were observed to be functions of the adsorbed phase concentration. However, surprisingly, the functions were significantly stronger than those predicted from the use of chemical potential gradient as the driving force for diffusion with constant intrinsic mobility. In other words, the thermodynamically corrected transport parameters were also stronger functions of the adsorbate concentration in the adsorbent. To account for the concentration dependence of the thermodynamically corrected transport parameters, an empirical but simple and effective procedure was proposed. The limiting (i.e., thermodynamically corrected) transport parameters, D_{c0} and k_{b0}, have been generally found to be independent of fractional coverage, θ, in zeolite where the pore size is uniform. In CMS adsorbents, since micropore sizes are distributed and the pore connectivities are not fully understood, it appeared logical to assign each pore size its own characteristic D_{c0} and k_{b0} values. This argument combined with the fact that pores are filled in the order of increasing size requires D_{c0} and k_{b0} to be increasing functions of θ. The following forms were validated for unary diffusion:

$$D_{c0} = D_{c0}^* \left(1 + \beta_p \frac{\theta}{1-\theta} \right) \qquad (1.9)$$

$$k_{b0} = k_{b0}^* \left(1 + \beta_b \frac{\theta}{1-\theta} \right) \qquad (1.10)$$

The above forms satisfy the expected behavior at $\theta \to 0$. β_p and β_b were obtained by fitting experimental D_c / D_{c0}^* vs. θ and k_b / k_{b0}^* vs. θ data, respectively. D_c and k_b are related to D_{c0} and k_{b0} by the Darken equation ($D_c / D_{c0} = d \ln c / d \ln q$) and its equivalent for barrier coefficient ($k_b / k_{b0} = d \ln c / d \ln q$). The above hypothesis was experimentally verified with single component integral uptake data for oxygen, nitrogen, carbon dioxide and methane in BF and Takeda I CMS.

More importantly, the following multicomponent extensions of Eqs (1.9) and (1.10) were also proposed and validated with binary/ternary integral uptake experiments of oxygen-nitrogen and methane-carbon dioxide-nitrogen mixtures in both the adsorbents:

$$(D_{c0})_i = D_{c0}^* \left(1 + \sum_{j=1}^{n} \beta_{pi} \frac{\theta}{1 - \sum_{j=1}^{n} \theta_j} \right) \qquad (1.11)$$

$$(k_{b0})_i = k_{b0}^* \left(1 + \sum_{j=1}^{n} \beta_{bi} \frac{\theta}{1 - \sum_{j=1}^{n} \theta_j} \right) \qquad (1.12)$$

where $\theta_i = q_i / q_{si}$ and i=1,2,…,n.

The above muticomponent extensions are based on the assumption that the contribution of components in a multicomponent system are linearly additive. It is

important to note that in both studies, D_c / D_{c0}^* vs. θ and k_b / k_{b0}^* vs. θ were obtained from unary differential uptake measurements and no additional fitting parameters was involved when the proposed empirical model was applied to predict unary, binary and ternary integral uptake results.

1.5 Reported Adsorption Data of Oxygen and Argon

In a kinetically controlled separation process, the selectivity depends on both kinetic and equilibrium effects. Hence, both kinetic and adsorption equilibrium data are required for process design. Because interest in CMS has been stimulated mainly due to its ability to separate O_2 and N_2, both kinetic and equilibrium data for these two sorbates in CMS have been reported in many studies, some of which were mentioned in the previous section. On the other hand, data for Ar adsorption and diffusion are very limited.

Reid et al. (1998) measured adsorption equilibrium and kinetics of Ar on a CMS sample supplied by Air Products and Chemicals Inc. using gravimetric method. In that study, the Henry's law constant calculated from extrapolation of virial equation for a wide range isotherm (0-900 kPa) was in good agreement with that obtained from low pressure range measurements (0-9 kPa). The results also showed that the kinetics for Ar on this sample followed a linear driving force model.

In another study, Ma et al. (1991) measured the adsorption and diffusion data of Ar on three different CMS samples (Takeda 5A, Takeda 3A and BF CMS). The experiments were carried out in two gravimetric setups, one for high pressure and the other for low pressure. Henry's law constants obtained from the two ranges were generally inconsistent. The uptake was well described by Fick's law.

Perhaps due to its success in separation of O_2 and N_2, only CMS adsorbent has received some attention for exploring O_2 and Ar separation by kinetically controlled PSA. The feasibility of 4A zeolite for O_2/Ar separation has not been studied. In fact, it is the adverse equilibrium rather than diffusivity ratio that makes 4A zeolite unsuitable for O_2 and N_2 separation. The adverse equilibrium has been reduced somewhat in a modified version of 4A zeolite called RS-10 (Farooq et al., 1995). In case of O_2 and Ar, the equilibrium isotherms of the two gases are very close and the diffusivity ratio on 4A zeolite was reported to be ~400 at 273 K (Ruthven and Derrah, 1975), which is much higher than most reported values on CMS samples. Hence, 4A zeolite also appears to be a suitable adsorbent for kinetic separation of O_2/Ar mixture.

Some reported adsorption equilibrium and kinetic data on some potential adsorbents for O_2 and Ar separation are summarized in Table 1.3, together with the kinetic selectivity values calculated according to Eqs (1.2) and (1.3).

1.6 Models for PSA Simulation

Since the introduction of PSA, many simulation methods have been suggested, based on varying degrees of simplifying assumptions, to facilitate the understanding, design and optimization of such processes.

The simplest and the earliest approach to the modeling of a PSA separation process is the equilibrium theory, which assumes local equilibrium without any consideration of dispersive effects. This approach is theoretically important because it gives analytical solution in some cases, which provides the first insight into the system behavior and qualitative guidance for process design. However, the mathematical simplicity is achieved at the expense of accuracy. Equilibrium theory normally fails to give quantitatively satisfactory results since the assumption of negligible dispersive

Table 1.3 Reported equilibrium and kinetic data of O_2 and Ar in some adsorbents.

Adsorbent	Temp. (K)	$K(10^6$mol/kg·Pa) O_2	Ar	D/r^2 $(10^{-4}$s$^{-1})$ O_2	Ar	α_{pore} or $\alpha_{barrier}$	Reference
Takeda CMS 3A	273	13.20[a] / 10.40[b]	8.23[a] / 7.10[b]	20	1.9	5.15 / 4.75	Ma et al., 1991
	303	4.64[a] / 3.99[b]	5.64[a] / 4.63[b]	47	3.6	2.98 / 14.2	
	323	4.66[a] / 3.67[b]	3.65[a] / 3.24[b]	84	5.9	4.81 / 4.27	
Takeda CMS 5A	273	9.53 / 7.79	8.09 / 6.95	14	5.4	1.9 / 1.12	
	303	3.53 / 3.49	5.52 / 4.52	65	9.7	1.65 / 2.00	
BF CMS	303	4.24 / 3.95	3.17 / 2.66	52	1.7	7.4 / 8.21	
CMS[c]	313	2.50	2.77	K $(10^{-4}$s$^{-1})$ 196.1	5.4	36.3	Reid et al., 1998
4A zeolite	303	-	-	D $(10^{-8}$cm^2/s) 3.5	0.0077	~21[d]	Ruthven and Derrah, 1975

a, b: In the study by Ma et al. (1991), Langmuir and VSM equations were used to fit the experimental isotherm over a wide range and Henry's constants were calculated from the extracted parameters of the models. The different values are all listed here: a denotes values from Langmuir model, b denotes values from VSM model. c: Sample supplied by Air Products and Chemicals Inc. d: Calculated based on the assumption that the ratio of K values is 1.

effects is valid for only few idealized systems. A detailed review of modeling of equilibrium theory of PSA separation is given by Ruthven et al. (1994a).

Side by side with the equilibrium theory, many dynamic models have also been developed to account for the mass transfer resistance, which is generally present in real systems, even when equilibrium controlled. The growth of dynamic PSA modeling has followed the route of gradual development by progressive elimination of the simplifying restrictions.

The earliest dynamic models dealt with systems in which the strongly adsorbed component is in a trace amount from an inert product, such as the removal of CO_2 from He using silica gel (Mithchell and Shedalman, 1973; Raghvan and Ruthven, 1985) and drying of air using activated alumna and silica gel (Chihara et al., 1983). Such systems are relatively easy to model for the following three reasons:

1. The separation is equilibrium controlled and simple linear driving force (LDF) model gives adequate approximation for the secondary effects of mass transfer resistance.

2. Since the adsorbate is present in trace amount in the feed, the velocity change along the bed is negligible.

3. For a trace system, isothermal behavior can be assumed. Of course, it has been shown in some studies that heat effect can be important even in trace systems (Chihara and Suzuki, 1983; Farooq et al., 1989).

The above simplifications, however, do not apply for bulk separations and kinetically controlled processes. Further significant improvements of the dynamic approach include consideration of axial dispersion, variation of fluid velocity due to adsorption/desorption, and very detailed kinetic models that are more realistic.

A detailed kinetic model to account for the transport resistance in the intra-particle porous network is most important for the simulation of kinetically controlled PSA separation. While LDF model with properly chosen Ω values has been shown to give varying degrees of qualitative success (Fatehi et al., 1995; Kapoor and Yang, 1989; Farooq and Ruthven, 1990), more detailed pore diffusion model is certainly more realistic and quantitatively superior (Farooq et al., 1993).

Shin and Knaebel (1988) presented a constant diffusivity micropore diffusion model for PSA air separation on RS-10. Good match between theory and experiment was obtained over a wide operating pressure range by fitting the micropore diffusion coefficient. The fitted diffusivity values were significantly different from the experimental values measured in the linear range. This was due to the well known concentration dependence of micropore diffusivity. Farooq and Ruthven (1991) then developed a model for bulk binary kinetic separation taking account of this concentration dependence based on the gradient of chemical potential as true mass transfer driving force and adsorption equilibrium represented by Langmuir isotherm. In a subsequent study, Farooq et al. (1993) applied their concentration dependent diffusivity model to Shin and Knaebel's system with equilibrium and kinetic parameters measured independently. The simulation results showed a generally good match with the experimental data. This model was then extended to a bidispersed model that included the transport resistance in the macropores, which becomes important in some operating regimes of a PSA process (Gupta and Farooq, 1999). The bidispersed pore model was further modified to include dual transport resistance in the micropores (Huang et al., 2001)

Any dynamic model consists of a system of coupled partial differential equations and the solution normally requires a numerical method, such as finite

difference, orthogonal collocation, etc. In a comparative study, Raghavan and Ruthven (1985) showed that the solution obtained by finite difference and collocation methods agreed well and the collocation method was much faster for the same level of accuracy.

1.7 Objectives and Scope of the Study

The primary objectives of this study were to identify a suitable adsorbent and to develop a feasible PSA cycle to separate O_2-Ar mixture. This involved the following four steps:

1. Comparison of different adsorbents based on linear range equilibrium and kinetic measurements. A total of four adsorbent samples were screened. The samples included one BF CMS, two Takeda CMS (designated as Takeda I and Takeda II for easy reference to the previous study from this laboratory) and one modified 4A zeolite called RS-10. Starting material for Takeda I was coconut shell, according to the accompanying material safety data sheet. The staring material for Takeda II was not specified.

2. Complete equilibrium and kinetic measurements over a wide pressure range for argon on Takeda II CMS, the adsorbent sample that gave the largest selectivity in step 1.

3. PSA O_2/Ar separation experiments on Takeda II CMS.

4. A PSA simulation model was developed to explain the experimental results. The experimentally verified simulation model was then used to study effects of different operating conditions such as pressure, feed velocity and step duration on PSA performance.

The thesis is structured in such a way that chapters 2-5 following this introductory chapter sequentially deal with the four stages of this study, as outlined above. Relevant background information and related theories are discussed in the

respective chapters. The conclusions and recommendations are given in chapter 6. A

detailed account of the numerical simulation of the PSA model is given in the appendix.

Chapter 2   Screening of Adsorbents

In a kinetically controlled separation process, the selectivity depends on uptakes and equilibrium capacities of the mixture components to be separated. The equilibrium and kinetics of the components in the linear range are normally used to carry out the initial screening of adsorbents, although many PSA processes operate outside the linear range (Ruthven et al., 1994a).

As discussed in Section 1.4, oxygen was one of the four gases for which extensive equilibrium and kinetic data was measured in all three CMS samples in a recently conducted study in the laboratory. Equilibrium and kinetics of oxygen in RS-10 were also available from a previous study (Huang et al., 2003a). Hence, equilibrium and kinetics of argon adsorption on three CMS samples and one zeolite sample were carried out in this study.

Adsorption measurement can be carried out either by static methods, such as gravimetric and volumetric methods, or by dynamic methods, such as column breakthrough and chromatographic methods. Generally speaking, compared to static methods, dynamic methods have the advantages of greater reliability due to the large amount of adsorbent used but suffer from elaborate experimental procedure and data analysis. In addition, each breakthrough curve gives only one point of equilibrium and kinetic data. As such, measurement over a wide pressure range may be very time consuming. In this study, the equilibrium and kinetic data of Ar in the four adsorbents were measured in the linear range for the purpose of screening. Both volumetric method and column breakthrough method were employed and the results were consistent.

2.1 Volumetric Method

2.1.1 Constant Volume Apparatus

The constant volume apparatus was designed to measure adsorption equilibrium and kinetics simultaneously. A schematic diagram of the apparatus is shown in Figure 2.1.

DC: Dose Chamber (350 cc)
TC: Test Chamber (350 cc)
RC: Reference Cylinder (150 cc)
DPT1, 2 : Differential Pressure Transmitters
P1   : Pressure Gauge (-1~15 bar)
P2   : Pressure Gauge (-1~ 0 bar)
PT : Pressure Transducer (0~300 psig)
V1- 4: Ball Valves (1/8")
V5, 6: Ball Valves (1/4")
V7, 8: Ball Valves (1/2")
SV: Solenoid Valve (1/4")
VP: Vacuum Pump
T : Thermocouple
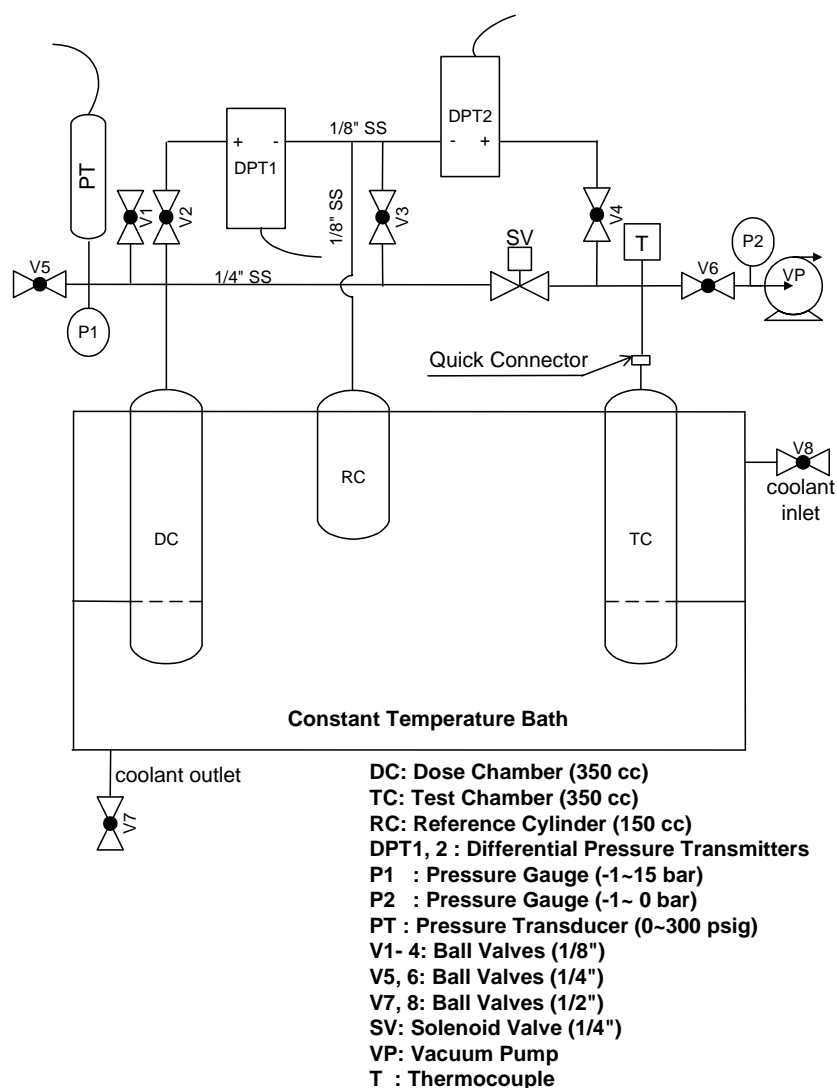
Figure 2.1 Schematic diagram of the volumetric apparatus.

The apparatus basically consisted of two cylindrical chambers, called test (TC) and dose (DC) chambers, connected by an on/off solenoid valve (Asco/Joucomatic,

Model 71235S) controlled with a DC power supply (Topward Electric Instruments, Model TPS-4000). The use of a solenoid valve made the opening very sharp. It helped minimize the dynamics associated with manual opening, which should not have any impact on equilibrium measurement, but could affect the early part of the uptake curve. Early part of the uptake data is very crucial for making distinction between possible transport mechanisms in the micropores. The adsorbent was placed in the test chamber. In order to facilitate more effective regeneration and to perform equilibrium measurements in the sub-atmospheric pressure range, a vacuum pump (Edwards, two-stage, Model M3), VP, was also connected to the system. Prior to beginning the experiment and between runs conducted at differential temperatures, CMS sample placed in the test chamber was regenerated at 200 $^{\circ}$C under high vacuum for 8-10 hours. Particular care was taken to purge the system with helium before heating the adsorbent to 200 $^{\circ}$C. Our limited experience seems to suggest that adsorption kinetics in CMS may be affected by heating at high temperature in presence of oxygen. The system was also flushed with helium a few times during heating to increase the effectiveness of regeneration. The zeolite sample was regenerated at 350 $^{\circ}$C.

In a system of known constant volume containing adsorbent, the response to a step perturbation in pressure by a known quantity contains information on both equilibrium and dynamics. A pressure transducer (Endress+Hauser, Model PMP131-A2201R4S, range: 0-300 psig), PT, was connected to the dose side to measure the initial and final system pressures, which were necessary to carry out the mass balance and calculate the equilibrium adsorbed amount. In addition to this absolute pressure transducer, there were two differential pressure transmitters (Validyne, Model P55D-1-N-2-38-S-4-A, range: -8 to +8 psig), DPT1 and DPT2, on the dose and the test sides and their reference ports were connected to a common cylinder (RC). The differential

pressure transmitters were necessary to track the change in pressure on the two sides of the solenoid valve until the system reached new equilibrium following the introduction of a known pressure step. The pressure transmitters were periodically calibrated using a digital pressure calibrator (Fluke, Model 700P07) to ensure accuracy of the pressure signals. The transient pressure signals monitored on the dose and test sides were combined to generate fractional uptake data for kinetic study. The voltage signal from the absolute pressure transducer was directly read on a multimeter (Hewlett Packard, Model 34401A) that could read up to 0.1 mV accurately. The signals from the two differential pressure transmitters were continuously recorded on a two-pen chart recorder (Yokogawa, Model LR4220). The chart range was appropriately chosen to capture the change with sufficient resolution. The dose, test and reference chambers were immersed in a constant temperature bath to maintain steady temperature at a desired level during measurements. A digital temperature controller (Lauda RK8 KS) was used for the purpose. Water was the heating/cooling medium. Since any change in the operating temperature had direct impact on the system pressure, tight control of the temperature at the desired level for the entire period of measurement was very important. In order to ensure that the system was completely leakproof, it was pressurized to about 10 atm or evacuated to nearly absolute vacuum without absorbent in place and all the outlet valves were closed to see if the pressure level was retained. The criterion used for pressure retention was constant voltage reading (within $\pm$ 0.0001 v) from the absolute pressure transducer for at least 2-3 hours.

Calculation of equilibrium and kinetic data from constant volume experiments also depended on the measured system volume. Hence, volumes of the dose and test sides including associated tubes were carefully measured and good accuracy was

24

ensured by checking reproducibility for a few times. Volumes of the dose and test sides were 340.2 and 364.9 cm^3, respectively.

Amount of adsorbent used in constant volume measurements was a compromise between the need to ensure that the change in pressure due to adsorption was measurable with sufficient resolution and yet the adsorbents were sufficiently spread out so that all the particles were uniformly exposed to the gas. This was not important for equilibrium measurement but was a crucial factor in the kinetic measurement in order to ensure uniform surface boundary condition for all the absorbent particles. Amounts of BF, Takeda I, Takeda II and RS-10 samples used in the present study were 8.7, 8.2, 7.6 and 16.6g, respectively. These weights were taken after regeneration. According to the material data sheet, density of the three CMS samples based on external volume (i.e., not including the helium pore volume) were 0.988 g/ cm^3 (BF), 1.02 g/ cm^3 (Takeda I) and 1.0 g/ cm^3 (Takeda II). Density of the RS-10 sample was 1.1 g/cm^3.

2.1.2 Experimental Procedures

After regenerating the adsorbent at 200 ^{o}C for CMS and 350 ^{o}C for RS-10 under vacuum, the valve connecting to the vacuum pump, VP, was closed and the system was brought to the desired experimental temperature using the constant temperature bath. A steady voltage output from the absolute pressure transducer (PT) was taken as the measure of thermal equilibrium. By then, the temperature reading of the thermocouple, T, placed in the test chamber also attained that of the constant temperature bath. At this point, the system pressure and temperature were noted and the solenoid valve, SV, was closed to separate the test side from the dose side. Let us denote this system pressure and temperature by $P^\infty(j-1)$ $[P_d^\infty(j-1) = P_u^\infty(j-1)]$ and

T_s , respectively. The subscripts *d* and *u* represent dose side and test side, respectively, and the superscript denotes complete equilibrium. j in the argument is the pressure step indicator and is introduced to develop a general data processing algorithm in the next section. Valve V3 was also closed to lock the pressure in the reference cell. Known amount of adsorbate gas was then added to the dose side through valve V1 and some time was allowed for the gas to attain the system temperature. Let this new pressure of the dose side be denoted by $P_d^{0+}(j)$ when the temperature stabilized to T_s. The solenoid valve was turned on and left in that position to allow the pressures on the dose and test sides to be equalized, and system to reach new equilibrium. Let the new equilibrium system pressure be $P^\infty(j)$ $[P_d^\infty(j) = P_u^\infty(j)]$. The reading of the thermocouple, T, placed inside the test chamber was found to remain practically unchanged at the set system temperature. The solenoid valve was closed after recording the new equilibrium system pressure. Valve V3 was then opened briefly to equalize the pressure of the reference chamber with that of the dose side. Fresh supply of adsorbate gas in known amount was added to the dose side and the rest of the steps were repeated in the same sequence as described above. This was continued until equilibrium system pressure reached up to the target upper range. For the screening study, the measurements were carried out in the vacuum range to remain within the linear isotherm range. Isotherms were measured up to approximately 6 bar for the chosen adsorbent (Takeda II CMS). Change of pressure on the dose and test sides [$P_d(j)$ and $P_u(j)$, respectively] following the opening of the solenoid valve were also followed until new equilibrium was reached, when desired, by continuously recording voltage output signals from the two differential pressure transmitters, DPT1 and DPT2, on a chart recorder. Approach to new equilibrium following the pressure

perturbation could be a very slow process depending on the system temperature and adsorbate gas in use. Hence, sufficiently long time (the reading of PT was oscillating between less than ±0.0001 v for at least 20 minutes) was allowed in each run to ensure complete equilibrium.

The magnitude of perturbation introduced in each step depended on the amount of fresh gas added each time to the dose side. For the screening study, starting from full vacuum, three pressure steps of ~0.1 bar were used for the equilibrium and kinetic measurements.

2.1.3 Data Processing

Calculating the amount adsorbed was a matter of straightforward material balance. Assuming that ideal gas law was valid in the pressure range for the gases in question, the following mass balance was applicable for the jth equilibrium step:

$$\{P_d^{0+}(j) - P^\infty(j-1)\}\frac{V_d}{R_g T_s} = \{P^\infty(j) - P^\infty(j-1)\}\frac{V_u - V_a}{R_g T_s} + \Delta n(j) \tag{2.1}$$

$$\Delta n(j) = n(j) - n(j-1) \tag{2.2}$$

where $j = 1, 2, 3, \ldots\ldots$

In Eq (2.1), V_d, V_u and V_a were volumes of the dose side, test side and adsorbent particles, respectively. $\Delta n(j)$ was the number of moles adsorbed by the adsorbent particles as a result of pressure perturbation in step j. $n(j)$ was the total number of moles adsorbed up to the jth step and was in equilibrium with the adsorbate at pressure $P_d^\infty(j) [= P_u^\infty(j)]$. Since the material data sheet provided adsorbent density based on contour volume, V_a calculated from the measured mass and given density, in fact, gave external particle volume (i.e., helium pore volume was not included). Hence

$n(j)$ included the moles of gas that were occupying the macropores of the adsorbent. Although CMS and zeolite particles have a bidispersed pore structure with clearly distinguish macropore and micropore resistances to the transport of sorbates, the macropores do not contribute to the adsorption capacity of this adsorbent. At equilibrium, the macropore voids have the same gas as in the bulk phase. Since the focus of the present study was transport of gases in the micropores, it was more convenient for the modeling study to use equilibrium adsorbed concentration expressed on the basis of microparticle volume. Equilibrium adsorbed concentration per unit microparticle volume, q_c, was related to adsorbed concentration per unit macroparticle volume, q_p, by the following equation:

$$q_p = (1 - \varepsilon_p)q_c + \varepsilon_p c \tag{2.3}$$

In the above equation, ε_p is the macropore voidage and c is the gas phase concentration with which the adsorbent had attained equilibrium. In this study, macropore voidage of 0.33 was assumed for all the three CMS samples. Macropore voidage for the RS-10 sample was 0.29 (Farooq, 1995). In terms of the variables used to describe equilibrium data processing, $q_p = n(j)/V_a$ and $c = P^\infty(j)/R_g T_s$. All the isotherms measured in this study have been presented as q_c vs. c plots.

Brandani (1998) has presented a detailed analysis of kinetic measurement in a constant volume apparatus for the case of pore diffusion control. It has been shown that the presence of a maximum in pressure vs. time plot for the test side is a clear evidence of kinetic control, which has led to the conclusion that pressure response of the test side should be used for extracting kinetic data. We do not disagree with this conclusion and had used the suggested criterion to confirm that our experiments were indeed in the kinetically controlled region. However, we decided to use fractional uptake plots

by combining the pressure responses from the two sides according to the following equation:

$$\frac{m_t}{m_\infty}(j) = \frac{\left\{P_d^{0+}(j) - P_{dt}(j)\right\} - \left\{P_{ut}(j) - P^\infty(j-1)\right\}{(V_u - V_a)}\Big/{V_d}}{\left\{P_d^{0+}(j) - P^\infty(j)\right\} - \left\{P^\infty(j) - P^\infty(j-1)\right\}{(V_u - V_a)}\Big/{V_d}} \tag{2.4}$$

Fractional uptake, $\dfrac{m_t}{m_\infty}$, plotted against square root of time had more distinct attributes to distinguish among possible transport mechanisms. The mathematical basis for this behavior is discussed in the next section.

2.2 Effect of Transport Mechanism on Fractional Uptake

Fractional uptake, following a step change in gas phase concentration, is defined as:

$$\frac{m_t}{m_\infty} = \frac{\overline{q_t} - q_0}{q_\infty - q_0} \tag{2.5}$$

where q_0 is initial concentration and $\overline{q_t}$ is the average concentration in adsorbed phase at time t:

$$\overline{q} = \frac{3}{r_c^3}\int_o^{r_c} q r^2 dr \tag{2.6}$$

For simplicity, only micropore transport is considered in this part of the discussion. Since the macropore resistance is not significant for the gases of our interest in the chosen adsorbents, the above simplification will not affect the conclusions drawn at the end of this section. Also, constant transport parameters and

constant gas phase concentration are assumed. Subjected to these assumptions, the analytical expressions of single component fractional uptake for different transport mechanisms have been well established in the literature (Ruthven et al., 1994a; Loughlin et al., 1993)

For transport controlled by diffusion in the micropore interior, the uptake is given by:

$$\frac{m_t}{m_\infty} = 1 - \frac{6}{\pi^2} \sum_{n=1}^{\infty} \frac{e^{-n^2 \pi^2 D_c t / r_c^2}}{n^2} \tag{2.7}$$

For a pore model, the fraction uptake is normally plotted against dimensionless time, $D_c t / r_c^2$. The theoretical plot of m_t / m_∞ vs. $D_c t / r_c^2$ is independent of diffusional time constant, which allows easy determination of this parameter from experimental data interactively on a spreadsheet.

The 1st and 2nd derivatives of Eq 2.7 with respect to $\sqrt{t}$ are:

$$\frac{d\left(m_t / m_\infty\right)}{d\sqrt{t}} = 12\sqrt{t} D_c / r_c^2 \sum_{n=1}^{\infty} e^{-n^2 \pi^2 D_c t / r_c^2} > 0 \tag{2.8}$$

$$\frac{d^2\left(m_t / m_\infty\right)}{d\left(\sqrt{t}\right)^2} = 12 D_c / r_c^2 \sum_{n=1}^{\infty} \left[e^{-n^2 \pi^2 D_c t / r_c^2} \left(1 - 2n^2 \pi^2 D_c t / r_c^2\right) \right] < 0 \tag{2.9}$$

The inequality in Eq (2.9) can be proven numerically.

The above discussion means that the fractional uptake curve based on a pore model is monotonically increasing and always convex upwards.

In case of transport controlled by a restriction at the pore mouth rather than the pore interior, the uptake rate is given by:

$$\frac{d\overline{q}}{dt} = k_b\left(q^* - \overline{q}\right) \tag{2.10}$$

Eq (2.10) is the barrier resistance model (mathematically equivalent to the LDF model) and k_b is the barrier transport coefficient. Fractional uptake for barrier resistance controlled transport and its derivatives with respect to $\sqrt{t}$ are:

$$\frac{m_t}{m_\infty} = 1 - e^{-k_b t} \tag{2.11}$$

$$\frac{d(m_t / m_\infty)}{d\sqrt{t}} = 2k_b\sqrt{t}e^{-k_b t} > 0 \tag{2.12}$$

$$\frac{d^2(m_t / m_\infty)}{d\left(\sqrt{t}\right)^2} = 2k_b e^{-k_b t}\left(2k_b t - 1\right) \tag{2.13}$$

The fractional uptake curve is still monotonically increasing but has a turning point at time, $t = 1/(2k_b)$. This feature manifests as S-shape when $\frac{m_t}{m_\infty}$ is plotted against $\sqrt{t}$.

The conclusion from the above discussion is that experimental $\frac{m_t}{m_\infty}$ plotted against $\sqrt{t}$ is a definite way of detecting the presence of barrier resistance.

Representative experimental uptake data for Ar in the four adsorbents are shown in Figure 2.2. Consistent with our understanding from vast literature studies on uptake of gas in zeolite adsorbents, uptake of Ar in RS-10 is pore diffusion controlled. The S-shape in the early part of the uptakes in the CMS samples is a clear sign of the presence of barrier resistance. This observation is in line with the behavior of oxygen,

nitrogen, methane and carbon dioxide in the CMS samples reported in another study from this laboratory (Huang et al. 2003a).
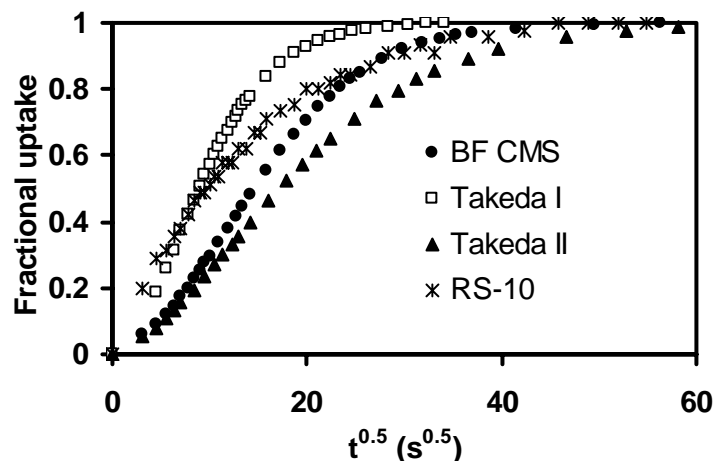
Figure 2.2 Representative experimental uptake data for Ar in the four adsorbents.

2.3 Adsorption Equilibrium: Henry's Law Constants

Adsorption equilibrium in the four adsorbents was measured in the linear range at three temperatures. At each temperature, three small pressure steps, each of which was about 0.1 bar, were given to make sure that the measurements were within the linear range where Henry' law applies:

$$q_c = K_c c \tag{2.14}$$

where K_c is dimensionless Henry's law constant. Figure 2.3 shows the q_c vs. c plots, which, as expected, form straight lines passing through the origin. The slopes of these lines directly gave the respective K_c values.
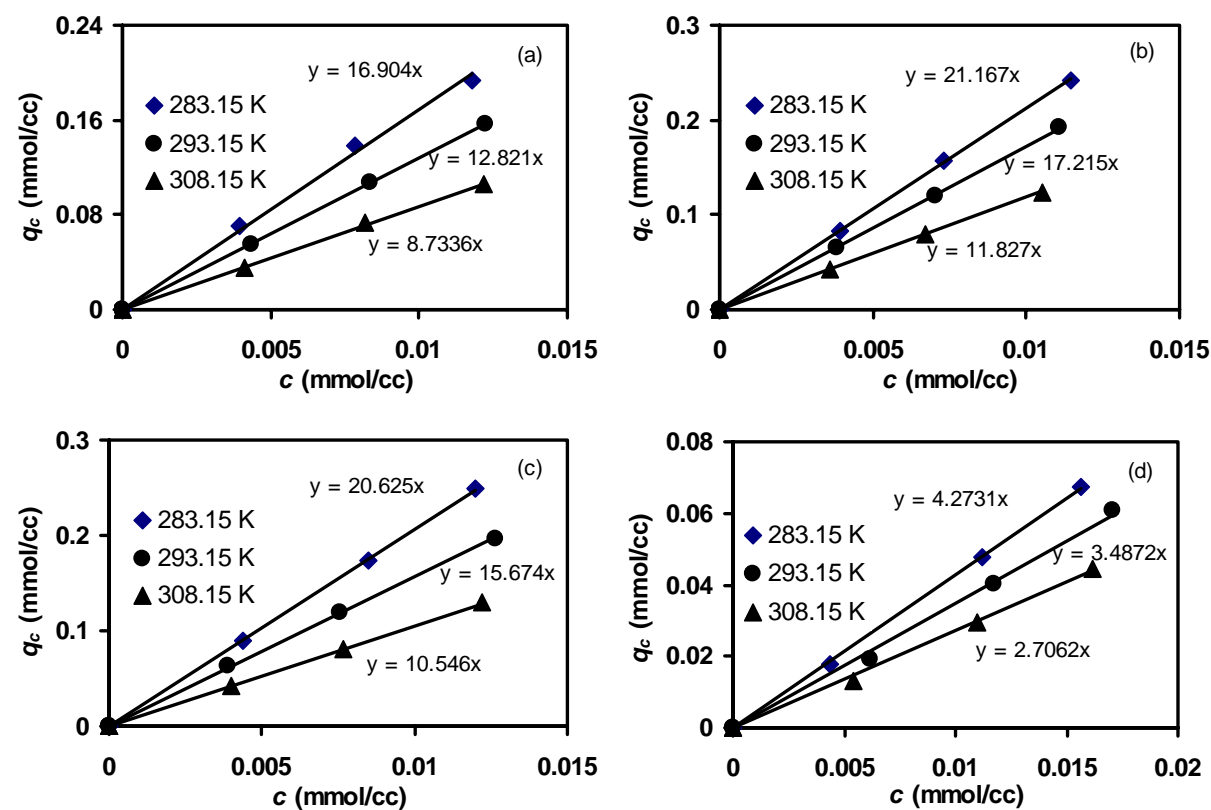
Figure 2.3 Plots of q_c vs. c in the linear range (a) BF CMS (b) Takeda I (c) Takeda II (d) RS-10.

The temperature dependence of Henry's law constant follows Arrhenius law:

$$K_c = K_0 e^{(-\Delta U / RT)} \tag{2.15}$$

where ΔU (kcal/mol) is the change in internal energy due to adsorption, K_0 is the preexponential constant, T (K) is temperature and R (kcal/mol/K) is the universal gas constant. Figure 2.4 shows the plots of K_c vs. $1/T$ on semi-log axes, which, as expected, give straight lines with intercept of K_0 and slope of $-\Delta U/R$.
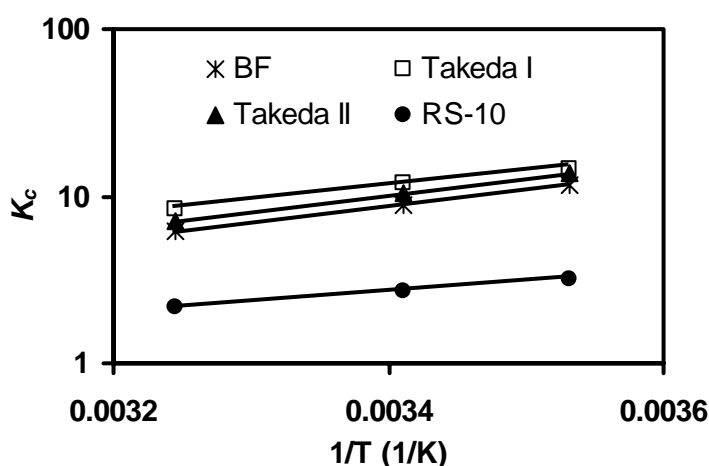
Figure 2.4 Temperature Dependence of Henry's Law Constants.

2.4 Adsorption Kinetics: Determination of the Transport Parameters

Although the gas diffusion in CMS and RS-10 is practically controlled by the resistance in the micropores, for the sake of completeness, macropore diffusional resistance was also taken into account in the model used in this study. Since pure gas was used, there was no external film resistance to gas transport.

2.4.1 Assumptions

The following assumptions were made in the model development:

(1) The ideal gas law applied and the system was considered isothermal.

(2) Only molecular diffusion was assumed for the transport in the macropores.

(3) Both macroparticles and microparticles were assumed to be spherical.

(4) The segment of isotherm covered in a differential step change was taken as linear and the kinetic parameters were assumed to remain constant over the small segment.

(5) The opening time of the solenoid valve was assumed to be negligible compared to the time of observation.

(6) An approximate linear form of a quadratic driving force was assumed to represent the dynamics of the solenoid valve separating the dose and test chambers.

2.4.2 Model Equations

In the constant volume apparatus, there was a solenoid valve separating the two sides. To account for the influence of the solenoid valve, if any, on the measured adsorption kinetics, the following equation was used:

$$\frac{dn_v}{dt} = X(P_d - P_u) \tag{2.16}$$

where n_v is the number of moles of gas flowing through the valve and X is the valve constant. Blank experiments (i.e., without any adsorbent on the test side) conducted with helium, oxygen and nitrogen to calibrate the valve constant, X, gave fairly constant value, which was an indication that the assumption of a linear driving force was reasonable.

The pressures on the two sides were functions of time in the volumetric measurement and are given by the following mass balance equations between the two sides of the apparatus:

Test or uptake cell mass balance:

$$\begin{cases} \varepsilon V_u \dfrac{dp_u}{dt} = R_g T \left(-3 \dfrac{D_p}{R_p} \varepsilon_p V_a \dfrac{dc_p}{dr_p}\bigg|_{r_p = R_p} + \dfrac{dn_v}{dt} \right) \\[2ex] P_u\big|_{t=0} = P_u^0 \end{cases} \tag{2.17}$$

Dose cell mass balance:

$$\begin{cases} V_d \dfrac{dP_d}{dt} = -R_g T \dfrac{dn_v}{dt} \\[2ex] P_d\big|_{t=0} = P_d^{0+} \end{cases} \tag{2.18}$$

In the above equations, P_u, P_d, P_u^0 and P_d^{0+} have the same meaning as $P_u(j)$, $P_d(j)$, $P_u^\infty(j-1)$ and $P_d^{0+}(j)$, respectively, introduced in the section on data processing.

The macropore mass balance equation and the boundary conditions have the following form:

$$\frac{\partial c_p}{\partial t} + \frac{1 - \varepsilon_p}{\varepsilon_p} \frac{\partial \overline{q}}{\partial t} = \frac{1}{R^2} \left[\frac{\partial}{\partial R} \left(R^2 D_p \frac{\partial c_p}{\partial R} \right) \right] \tag{2.19}$$

$$\frac{\partial c_p}{\partial R}\bigg|_{R=0} = 0 \tag{2.20}$$

$$c_p\big|_{R=R_p} = c = \frac{P_u}{R_g T} \tag{2.21}$$

The boundary condition at the centre of the macroparticle follows from geometrical symmetry. $\overline{q}$ is the average adsorbed phase concentration in the micropore, which is related to the adsorbate flux at the micropore mouth by the following equation:

$$\frac{\partial \bar{q}}{\partial t} = \frac{3}{r_c} D_c \frac{\partial q}{\partial r}\bigg|_{r=r_c}$$

(2.22)

The mass balance in the micropore presents different expressions depending on different transport mechanism.

D_p is related to the molecular diffusivity, D_M, by the following relation: $D_p = D_M / \tau$, where τ is the tortuority factor. In the absence of any better data, τ was taken as 3 in this study. The binary molecular diffusivity was estimated from the Chapman-Enskog equation (Ruthven, 1984). For binary gas mixture, binary molecular diffusivity is given by:

$$D_m = \frac{0.00158 T^{3/2} \left(\frac{1}{M_1} + \frac{1}{M_2} \right)^{1/2}}{P \sigma_{12}^2 \Omega(\varepsilon / kT)}$$

(2.23)

In the above equation, M_1, M_2 are the molecular weights of the two components in the binary gas mixture, P is the total pressure in atmospheres, σ_{12} is the average Lennard-Jones diameter in Angstroms, and dimensionless Ω is a function of $\varepsilon/\kappa T$, where $\varepsilon = \sqrt{\varepsilon_1 \varepsilon_2}$ is the Lennard-Jones force constant and κ is the Boltzmann constant. The tabulation of Ω and $\varepsilon/\kappa T$ are available in the literature (Bird et al., 2002). In pure gas study, the parameter values for argon were substitute to both components in the above equation.

The experimental results were analyzed using the pore diffusion model for the transport in RS-10 micropores and the barrier as well as the dual resistance models for transport in CMS micropores. Only the dual resistance model equations are presented here for reasons that will be discussed after presenting the equations. The mass balance equation for micropore diffusion is:

$$\frac{\partial q}{\partial t} = \frac{1}{r^2}\left[\frac{\partial}{\partial r}\left(r^2 D_c \frac{\partial q}{\partial r}\right)\right] \tag{2.24}$$

The boundary conditions are:

$$\frac{\partial q}{\partial r}\bigg|_{r=0} = 0 \tag{2.25}$$

$$\frac{3}{r_c} D_c \frac{\partial q}{\partial r}\bigg|_{r=r_c} = k_b \left(q^* - q\right)\bigg|_{r=r_c} \tag{2.26}$$

where q^* is in equilibrium with the macropore gas according Eq (2.27):

$$q^* = f(c_p) \tag{2.27a}$$

$$= K_c c_p \quad \text{(for a linear isotherm)} \tag{2.27b}$$

The barrier and pore models are actually two extreme cases of the dual model. The dual model solution reduces to that of the barrier model when a large value is assigned to the micropore diffusivity and vice versa. The dual model formulation thus allowed the flexibility of investigating both pore model and barrier model by appropriately adjusting the relevant parameters as discussed above.

The model equations were numerically solved by the method of orthogonal collocation.

2.4.3 Transport Parameters in the Linear Range

To understand the gas transport mechanism in CMS micropores and extract the transport parameters from the experimental uptake results, it is necessary to quantify valve resistance and investigate its impact on the shape of uptake. The resistance of the solenoid valve between the dose and test chambers was measured by conducting blank

runs (i.e., without any adsorbent in the test chamber) in a previous study (Huang et al., 2003a). The values obtained by varying the initial pressure levels on the two sides were nearly constant around a mean of 0.04 mol s^{-1} bar^{-1}. This value was used in this study for modeling the experimental uptakes of Ar in the four adsorbents. In the previous study, it was also shown that this valve resistance had negligible impact on the model solution for the uptake of various gases. This was demonstrated by assigning a large value to the valve constant ($X = 10$ mol s^{-1} bar^{-1}) to simulate valve resistance. A more direct experimental proof of the above conclusion may be seen from the uptake plots shown in Figure 2.2. The representation of the valve resistance is mathematically similar to the representation of the barrier resistance. Hence, if the valve resistance were important, it would result in an S-shape response in the early part of uptake in RS-10, which is well known to have pore interior diffusion controlled uptake. That no such signature is evident for the uptake in RS-10, confirms that the valve resistance was indeed negligible compared to the transport resistance.

The transport parameters for Ar in the four samples were extracted by optimizing the model fit to experimentally measured uptakes. The objective functions were to minimize the sum of squares of the residuals between model prediction and experimental results. Some representative optimized fits of the dual model and pore model in CMS and RS-10, respectively, to the experimental results are shown in Figure 2.5.

It should be highlighted that the residuals from the barrier model fit to the CMS data were consistently higher compared to those from the dual model fit. This observation is consistent with those reported by Huang et al. (2003a, 2003b) for other gases in these CMS samples.
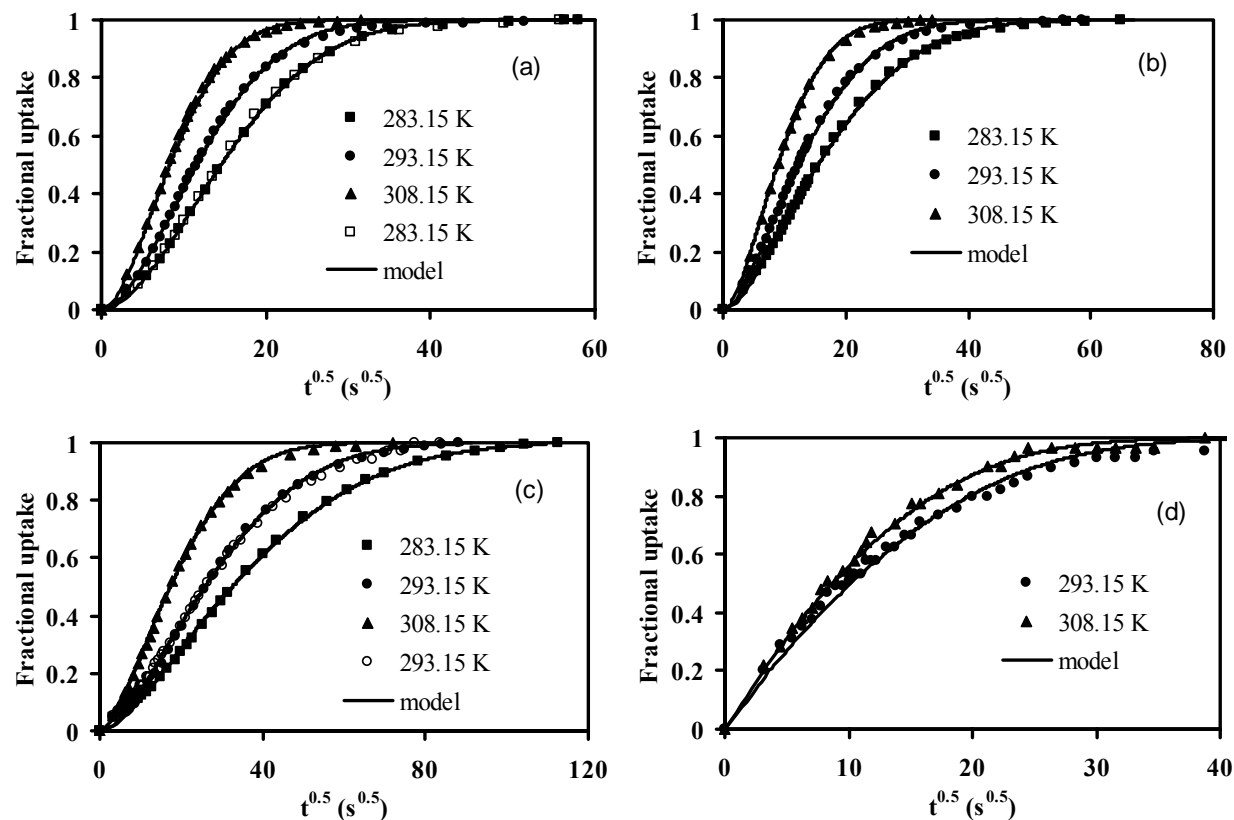
Figure 2.5 Experimental uptake curves in the linear range and model fits: (a) BF CMS (b) Takeda I (c) Takeda II (d) RS-10. The closed and open points in (a) at 283.15 K are experimental data at ~0.1 bar and ~0.2 bar, respectively. The open points in (c) at 293.15 K are experimental data measured by another volumetric set-up. These results present evidence of reproducibility of these measurements as well as isotherm linearity.

Figure 2.5 also shows that the experimental uptake curves at different subatmosphere pressure levels (within the linear range) converged very well, which is consistent with the theoretical prediction that in the linear range, kinetic parameters are independent of concentration (Ruthven, 1984). The reproducibility of uptake measurement is further validated by the consistence between the experimental uptake curves of argon in Takeda II CMS measured by two volumetric set-ups (see Figure 2.5).

The transport parameters also follow Arrhenius type temperature dependence and are given by the following equations:

$$k_b = k_b{}^0 e^{(-E_k/RT)} \qquad\qquad\qquad (2.28a)$$

$$D_c = D_c{}^0 e^{(-E_D/RT)} \qquad\qquad\qquad (2.28b)$$

where $k_b{}^0$ and $D_c{}^0$ are pre-exponential coefficients with physical meanings of transport parameters at $T \rightarrow \infty$, E_k and E_D in kcal/mol are activation energies. Figure.2.6 shows the k_b and $D_c/r_c{}^2$ plotted against $1/T$, which give straight line. Figure 2.6(b) is known as Eyring plot. The obtained E_D of BF, Takeda I, Takeda II CMS and RS-10 are 7.26, 9.93, 9.86 and 4.26 kcal/mol. The obtained E_k of BF, Takeda I and Takeda II CMS are 8.57, 6.65and 8.60 kcal/mol.

The equilibrium and kinetic parameters of Ar in the four adsorbents in the linear range measured in this study are summarized in Table 2.1. Similar data for oxygen, taken from another study in this laboratory, are also included for easy reference.
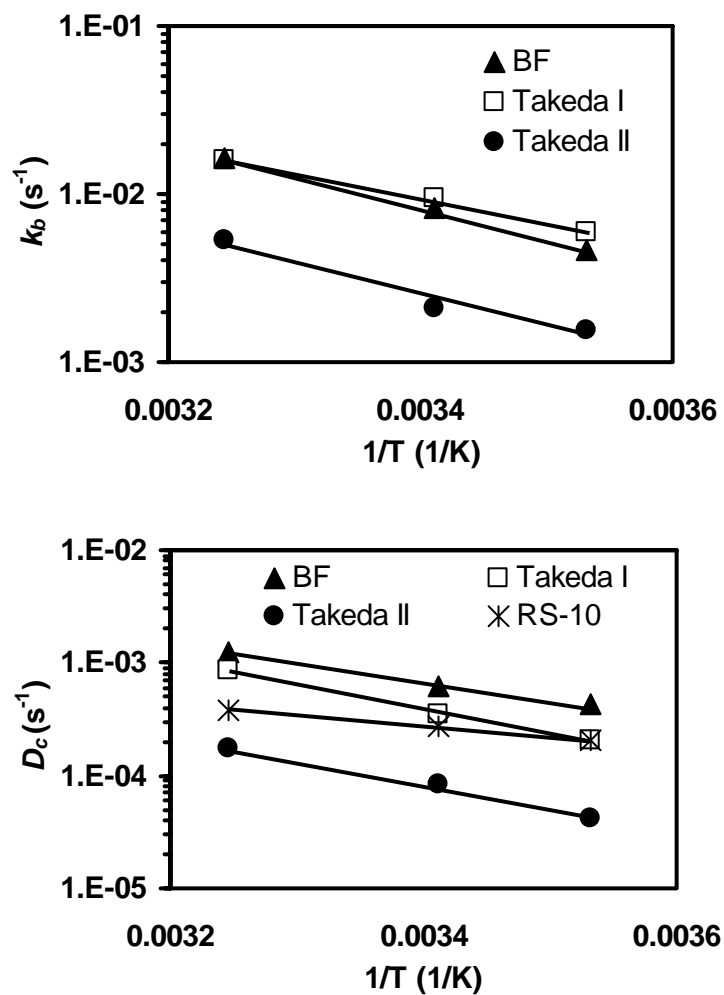
Figure 2.6 Temperature dependence of micropore transport parameters of Ar in the four adsorbents in the linear range.

Table 2.1 Equilibrium and kinetic parameters of Ar and O_2 in the CMS and RS-10 adsorbents in the linear range.

	BF CMS				Takeda I			
	Ar			O_2^ζ	Ar			O_2^ζ
Temp (K)	283.15	293.25	308.15	293.15	283.15	293.15	308.15	293.15
K (CV method)	16.9	12.8	8.7	11.8	21.2	17.2	11.8	14.9
K (DCBT method)	16.2	13.5	9.7	-	21.4	17.2	12.2	-
D_{co}^*/r_c^2 (10^{-4} s^{-1})	4.29	6.23	12.2	58.4	2.02	3.54	8.47	108
k_{bo}^* (10^{-3} s^{-1})	4.68	8.15	16.2	170	6.01	9.36	15.8	201
$L/5$	0.72	0.87	0.88	1.94	1.99	1.76	1.24	1.24
	Takeda II				RS-10			
K (CV method)	20.6	15.7	10.6	14.8	4.3	3.5	2.7	4.2
K (DCBT method)	19.6	13.4	10.2	-	-	-	-	-
D_{co}^*/r_c^2 (10^{-4} s^{-1})	0.42	0.84	1.78	85.3	2.07	2.78	3.85	109
k_{bo}^* (10^{-3} s^{-1})	1.56	2.07	5.29	98.4	-	-	-	-
$L/5$	1.99	2.26	1.98	0.77	-	-	-	-

ζ: oxygen data are from Huang et al., 2003a.
$L/5$: a parameter showing the relative importance of barrier and pore resistance. Please see Section (2.6).

2.5 Dynamic Column Breakthrough (DCBT) Study

DCBT is a useful experimental method and can also determine adsorption equilibrium and kinetic data simultaneously. The experiment involves measuring a series of breakthrough curves in a column packed with the adsorbent corresponding to step changes in the feed composition at the column inlet. In this study, DCBT method was used to validate equilibrium and kinetic data of Ar in the CMS samples.

2.5.1 DCBT Apparatus

A pre-existing DCBT apparatus was used in this study. A schematic diagram of the DCBT apparatus is shown in Figure 2.7. The apparatus mainly consisted of a column packed with pellets of adsorbent, a concentration detector and the necessary process control devices including a digital temperature controller (Polyscience, Model 9101) to circulate the heating/cooling medium, two mass flow controllers (Brooks

5850, 2SLPM and 10SLPM) to control the gas flow rates, a back pressure regulator (Go Inc., Range 0-250 psig) to maintain the system pressure at the desired operating level and a thermal conductivity detector (TCD) to continuously measure the exit concentration.

BF: Bubble Flowmeter
BPR: Back Pressure Regulator
C1: Adsorption Column
FM: Flowmeter
MFC1,MFC2: Mass Flow Controllers
GC: Gas Chromatagrophy
P1, 2: Pressure Gauges (0 - 15 bar)
TCD: Thermal Conductivity Detector
V1-10: 1/8" Ball Valves
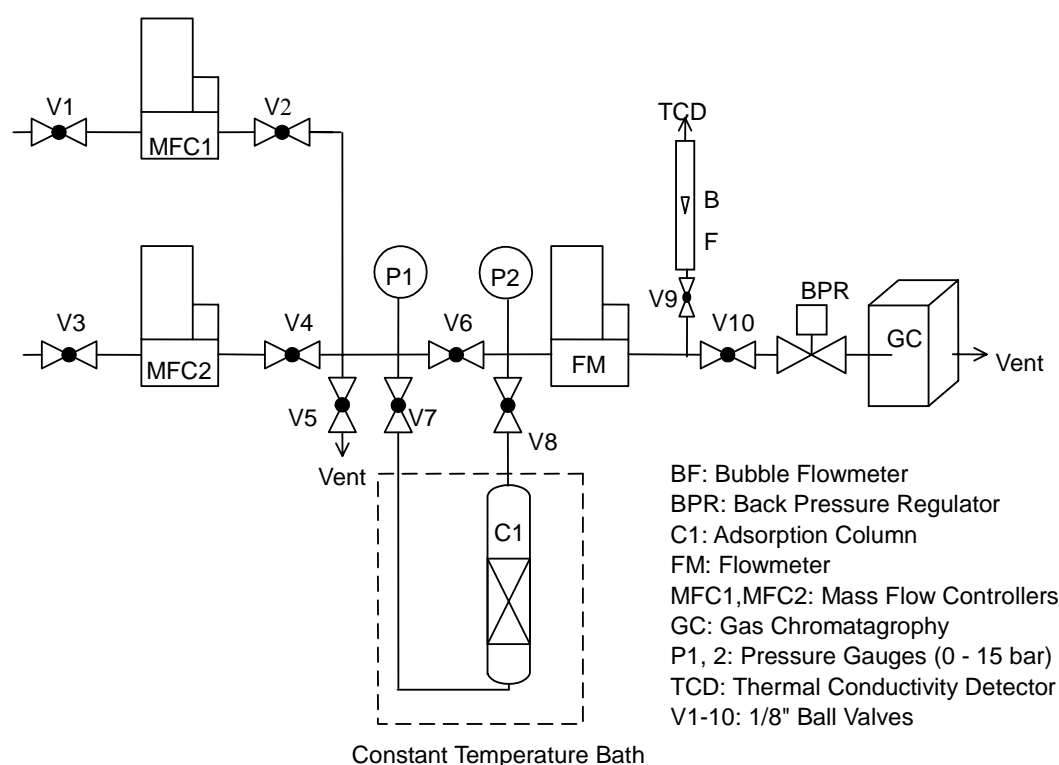
Figure 2.7 Schematic diagram of the DCBT apparatus.

Before the experimental runs, each column packed with CMS adsorbent particles was regenerated at 200 ^{o}C for more than 10 hours with a continuous purge of helium, which is necessary to prevent the CMS structure from being damaged in an oxygen environment at high temperature. The column was then cooled down to the room temperature under helium purge after which it was immersed in a constant temperature bath maintained at the desired experimental temperature. Sufficiently long time was allowed to ensure thermal equilibrium between the column and the bath. Helium flow was maintained all along.

For the single component runs, Ar was fed by mixing with helium, which is considered inert and, therefore, did not adsorb in the adsorbents. The column pressure was controlled slightly higher than atmosphere, and the concentration of argon was controlled at a low level of about 3 mole %. This corresponding partial pressure level was well within the linear range. At such a low concentration level, it was reasonable to assume negligible velocity change due to adsorption, which made the data analysis much simpler.

In this study, both adsorption and desorption breakthrough curves of argon on the CMS samples were measured at the same three temperatures as in the volumetric experiments. In the linear range of isotherm and provided the change in velocity due to adsorption/desorption is negligible, adsorption and desorption curves should be mirror image of each other. Hence, measurements of both adsorption and desorption confirmed both linearity and equilibrium reproducibility at the same time. Column dimensions and operating conditions in the DCBT experiments are listed in Table 2.2.

Table 2.2 Operating parameters of the DCBT experiments.

	BF CMS	Takeda I	Takeda II
L_{column}(cm)	40	40	40
D(cm)	3.5	3.8	3.8
Bed voidage	0.29	0.35	0.29
v_0^1 (cm/s)	1.58	1.51	1.51
v_0^2 (cm/s)	1.63	1.57	1.57
v_0^3 (cm/s)	1.65	1.72	1.72

1: runs at 283.15 K
2: runs at 293.15 K
3: runs at 308.15 K

All the runs were corrected for dead volume by subtracting the blank response measured under the same flow, pressure and temperature conditions. Details on blank correction have been well described by Yuan (1997).

2.5.2 Equilibrium Data Analysis

Figure 2.8 shows an experimental breakthrough response for argon at low feed concentration. Here, exit concentration normalized with respect to the feed concentration (c/c_0) is plotted as a function of time. Adsorption equilibrium can be derived from the shaded area, which is in unit of time and is defined as mean residence time.
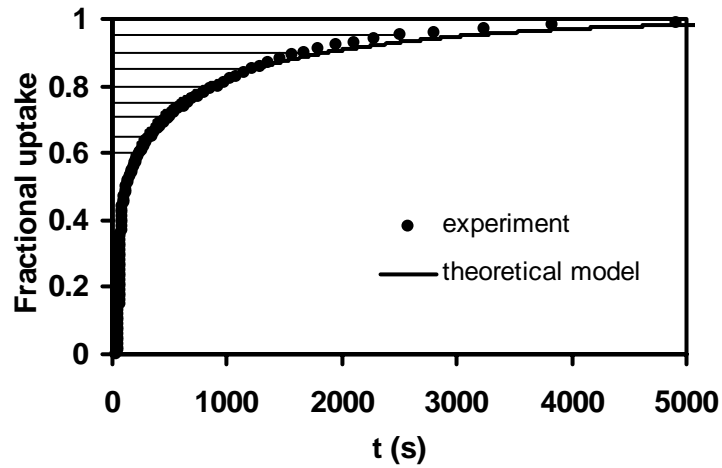
Figure 2.8 An example of argon breakthrough curve in the linear range of the isotherm.

The mean residence time of the adsorption or desorption process may be obtained from simple material balance leading to the following equations (Malek and Farooq, 1996b):

$$\text{Adsorption: } \bar{t}_{ad} = \int_0^\infty \left(1 - \frac{v_e c_e}{v_0 c_0}\right) dt \tag{2.29}$$

$$\text{Desorption: } \bar{t}_{ad} = \int_0^\infty \left(\frac{v_e c_e}{v_0 c_0}\right) dt \tag{2.30}$$

where v_o and v_e are the adsorbate inlet and outlet interstitial velocities, respectively, c_o and c_e are the feed adsorbate inlet and outlet concentrations, respectively, P is the

system pressure. When adsorbate gas concentration is very low, the velocity within the column can be assumed to be constant and the above equations reduce to:

$$\text{Adsorption: } \bar{t}_{ad} = \int_0^\infty \left(1 - \frac{c_e}{c_0}\right) dt \qquad (2.31)$$

$$\text{Desorption: } \bar{t}_{de} = \int_0^\infty \left(\frac{c_e}{c_0}\right) dt \qquad (2.32)$$

The integral in Eq (2.31) is the shaded area in Figure 2.8.

Hence, the equilibrium adsorption capacity, q_P^*, corresponding to the feed concentration of the adsorbate, c_0, is given by:

$$q_P^* = \left(\frac{v_0 \bar{t}}{L_b} - 1\right)\frac{\varepsilon_b}{1 - \varepsilon_b} c_0 \qquad (2.32)$$

where L_b is the column length and ε_b is the bed voidage, such that equilibrium adsorbed concentration is based on per unit particle volume.

q_p^* / c_0 is equal to the Henry's law constant K, when c_0 is in the linear range of the isotherm. The K is based on particle volume and is related to the Henry's constant based on micropore volume, K_c, by the following equation

$$K = \varepsilon_p + \left(1 - \varepsilon_p\right)K_c \qquad (2.33)$$

As may be seen from Table 2.1, the equilibrium constants from the two methods were in very good agreement.

2.5.3 Kinetic Data Analysis

While the shaded area in Figure 2.8 contains equilibrium information, the shape of the experimental concentration breakthrough curve contains kinetic information. The transport parameters can be extracted by matching the breakthrough curve with appropriate model, where the transport coefficients are the only unknowns.

The simulation of column dynamics may be viewed as an extension of constant volume apparatus. In a constant volume apparatus, the system pressure changed with time, which made the boundary condition at the surface a function of time. This is captured by the mass balance equation between the two sides (Eqs 2.16-2.18). At any time, however, all the particles had same condition at the surface. In case of column dynamics, the boundary condition at the adsorbent surface is a function of both time and location in the column, which may be obtained by solving the component mass balance equation for the external fluid phase. Assuming an axially dispersed plug flow model, the component mass balance for the external fluid phase is given by:

$$\frac{\partial c}{\partial t} = D_L \frac{\partial^2 c}{\partial z^2} - v_0 \frac{\partial c}{\partial z} - \frac{1-\varepsilon}{\varepsilon} \frac{\partial \bar{\bar{q}}}{\partial t} \tag{2.34}$$

The following Danckwerts boundary conditions for a dispersed plug flow system apply:

$$-D_L \frac{\partial c}{\partial z}\bigg|_{z=0} = v_0 \left(c_0 - c\big|_{z=0} \right) \tag{2.35}$$

$$\frac{\partial c}{\partial z}\bigg|_{z=L} = 0 \tag{2.36}$$

Ruthven (1985) has discussed the available correlations for estimating D_L. $\bar{\bar{q}}$ is the average adsorbate concentration in the particle, which is related to the adsorbate flux at the particle surface by the following mass balance equation:

$$\frac{\partial \bar{\bar{q}}}{\partial t} = \frac{3}{R_P} \varepsilon_p D_p \left.\frac{\partial c_p}{\partial R}\right|_{R=R_P}$$
(2.37)

The mass balance equations for macropore and micropore diffusion (Eqs 2.19 and 2.24) and the boundary conditions (Eq 2.20, 2.25 and 2.26), except the boundary condition at the particle surface, are also applicable for column dynamics. Since the adsorbate is fed to the column by mixing with inert carrier, there is a film resistance around the particle. Hence, a more appropriate boundary condition at the particle surface is given by:

$$\varepsilon_p D_p \left.\frac{\partial c_p}{\partial R}\right|_{R=R_P} = k_f \left(c - c_p\big|_{R=R_P}\right)$$
(2.38)

Ruthven (1985) has also discussed the available correlations for estimating k_f. The correlation of Wakao and Funazkri (1978) is more widely used.

A sensitivity analysis revealed that the axial dispersion and external film resistance estimated from the recommended correlations were not significant compared to the micropore resistance of Ar in the adsorbents under study.

The operating parameters of the experimental breakthrough curves are given in Table 2.2. The system of coupled equations described was numerically solved using the micropore transport coefficients obtained from the constant volume experiments compiled in Table 2.1. The model predictions obtained are compared with the experimental results in Figure 2.9. The good overall agreements indicate reliability of the kinetic data obtained from uptake measurements.
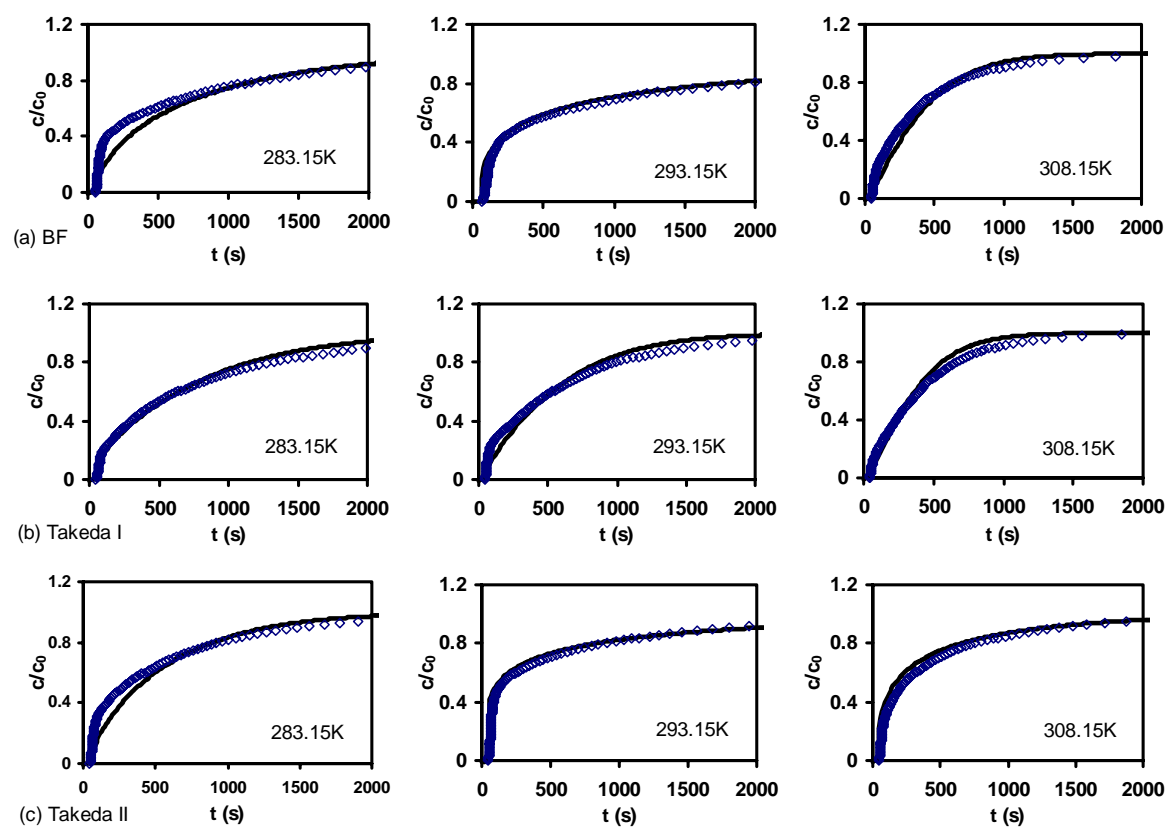
Figure 2.9 Comparison between experimental and predicted breakthrough in columns packed with (a) BF, (b) Takeda I and (c) Takeda II CMS adsorbents. The symbols are experimental points and the lines are model prediction.

2.6 Relative Importance of Pore Resistance and Barrier Resistance in CMS

Assuming negligible macropore resistance, fractional uptake for a dual resistance model for micropore transport is given by the following equation (Loughlin et al., 1993; Crank, 1956):

$$\frac{m_t}{m_\infty} = 1 - \sum_{n=1}^{\infty} \frac{6L^2 \exp(-\beta_n^2 D_c t / r_c^2)}{\beta_n^2 \left[\beta_n^2 + L(L-1)\right]} \tag{2.39}$$

where β_n are the non-zero roots of the equation

$$\beta_n \cot \beta_n + L - 1 = 0 \tag{2.40}$$

and

$$L = \frac{k_b}{3D_c / r_c^2} \tag{2.41}$$

Loughlin et al. (1993) also studied the overall mass transfer coefficient $k_{overall}$ for dual resistance system and derived the following relationship:

$$k_{overall} = 3\frac{D_c}{r_c^2}\left(\frac{5L}{5+L}\right) \tag{2.42}$$

where L is the dimensionless constant given by Eq (2.41), which represents the relative importance of the barrier resistance and the pore resistance (in the original paper, it is denoted by ζ). According to Gluekauf's approximation (Gluekauf, 1947), for an equivalent linear driving force representation of a pore diffusional problem, the linear driving force coefficient is given by $15\, D_c / r_c^2$. Therefore, based on Gluekauf's approximation, when L is equal to 5, barrier resistance and pore resistance have equal contribution to the overall resistance. Hence the value of $L/5$ may be used as a useful

measure of the relative importance of pore and barrier resistances. The $L/5$ values for Ar on the three CMS samples are in the range of 0.8-2.3. This indicates that both pore resistance and barrier resistance are important in the CMS samples. The actual values are given in Table 2.1.

It is well-known that Gluekauf's linear driving force representation of a pore diffusional problem is only approximate and cannot capture the true dynamics of a pore diffusion controlled process (Farooq et al., 2002). Hence, the $k_{overall}$ given by Eq (2.42) for a dual resistance system (pore mouth barrier followed by distributed diffusional resistance in the pore interior) does not provide an alternative to the full solutions, if the objective is to accurately capture the process dynamics.

2.7 Kinetic Selectivity of Oxygen-Argon in the Adsorbents Studied

It was briefly discussed in Section 1.2 that in order to estimate the efficiency of an adsorbent for gas separation, the selectivity is generally defined as:

$$\alpha_{AB} = \frac{\overline{q}_A / c_A}{\overline{q}_B / c_B}$$

(2.43)

where A and B denote the components to be separated.

For an equilibrium controlled separation, the above equation reduces, in the linear range of isotherm or when both the components obey Langmuir isotherm, to the ratio of the Henry's constant of the two components. For a kinetically controlled separation, Eq (2.42) may be manipulated to the following form:

$$\alpha_K = \frac{\left(\dfrac{m_t}{m_\infty}\right)_A \dfrac{q_A^*}{c_A}}{\left(\dfrac{m_t}{m_\infty}\right)_B \dfrac{q_B^*}{c_B}} \tag{2.44}$$

It is clear from the above equation that kinetic selectivity is time dependent and will ultimately approach the equilibrium selectivity. Assuming uncoupled equilibrium and kinetics, Ruthven et al. (1994) have shown that for short contact and pore diffusion controlled uptake, the kinetic selectivity is given by:

$$\left(\alpha_K\right)_{pore} = \frac{K_A}{K_B} \sqrt{\frac{\left(D_{c0}\right)_A}{\left(D_{c0}\right)_B}} \tag{2.45}$$

The analogous equation for barrier controlled uptake is:

$$\left(\alpha_K\right)_{barrier} = \frac{K_A}{K_B} \frac{\left(k_b\right)_A}{\left(k_b\right)_B} \tag{2.46}$$

The dual resistance controlled fractional uptake is given by Eq (2.39). It is obvious that this series solution will not reduce to simpler expression at short time. In order to compare the four adsorbents for oxygen-argon separation, the complete time history of kinetic selectivity was calculated using the analytical solution for $\dfrac{m_t}{m_\infty}$ by Eq (2.39). A FORTRAN program was used to evaluate the series solutions corresponding to the pore model and the dual model. Based on the findings reported in Section 2.4.3, pore model and dual model solutions were used for RS-10 and CMS, respectively. Number of terms in the series solutions was increased until difference between two consecutive summations differed by < 0.1%. The β_n values were solved by the Bisection Method with accuracy of 10^{-6}. The time histories of oxygen-argon kinetic

selectivity in the four adsorbents are shown in Figure 2.10. Selectivity according to Eq (2.46) is also plotted in the figure for the CMS adsorbents. It is evident that kinetic selectivity for dual resistance model reduces to Eq (2.46) at very short contact time.
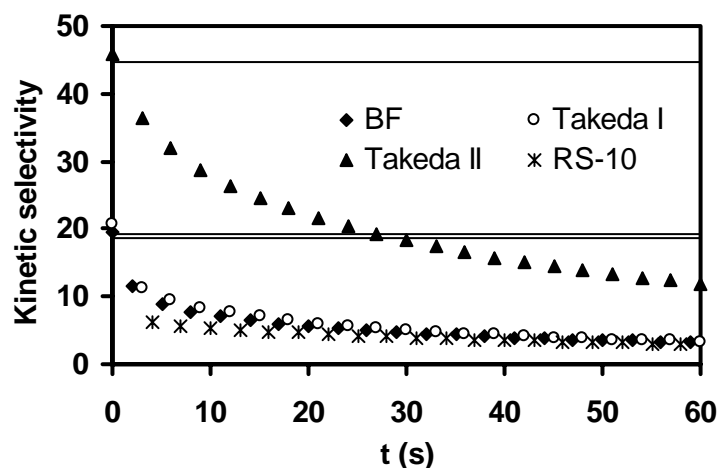
Figure 2.10 Comparison of calculated kinetic selectivity of the four adsorbents for O_2/Ar separation. Solid lines are the selectivity values calculated according to Eq (2.46) for the three CMS samples.

From the summary of adsorbents screening presented in Figure 2.10, it is clear that Takeda II showed significantly higher kinetic selectivity for oxygen-argon separation. Takeda II was therefore chosen for PSA separation study. A more detailed study on equilibrium and kinetics of argon adsorption in Takeda II CMS is presented in the next chapter.

Chapter 3   Detailed Equilibrium and Kinetics of Argon

Adsorption in Takeda II CMS

The linear range study detailed in the previous section showed that among the four adsorbents investigated, Takeda II CMS had the highest selectivity for O_2/Ar separation. However, since PSA processes may operate over a wide pressure range, adsorption data in the linear range are not enough for PSA study. Hence, equilibrium and kinetic measurements were conducted by the volumetric method up to 6 bar to gain a more complete understanding of Ar isotherm and its transport mechanism in Takeda II CMS.

3.1 Equilibrium

Equilibrium measurement at low pressure was described in detail in Section 2.1.3. Following the same procedure, equilibrium measurement of argon in Takeda II CMS was conducted up to 6 bar at 283.15K, 293.15K and 308.15K. In the equilibrium measurement, the step size is determined by the frequency of data points desired in the above pressure range. The step size also depends on the maximum pressure differential that differential transducers can withstand. Hence, during the equilibrium measurements with large pressure steps, valves V1, V3 and V4 (see Figure 2.1) were closed to isolate the pressure transducers and the reference chamber. Pressure step of approximate 1 bar was used in the equilibrium study of argon in Takeda II CMS. The other objective of this part of the study was to measure differential uptake of argon at various levels of adsorbent loading. Therefore, at chosen equilibrium levels, valves V1, V3 and V4 were opened and experiments were conducted with small step size (~0.1 bar) and pressure transients on the two sides were recorded on a data acquisition system. A data acquisition card (National Instruments, Model AT-M10-16E-10)

connected to a personal computer (Intel Pentium III) was used for this purpose. The frequency of data collection was 3 points per second. Replacing chart recorder with computer data acquisition was a contribution of this project. Small step size during kinetic measurements ensured linearity of the segment of isotherm traveled during the uptake so that the transport parameters could be assumed to remain approximately constant. How small a step size was small enough to ensure linearity depended on the curvature of the isotherm and hence some degree of trial and error was necessary.

3.1.1 Langmuir Model

The Langmuir model is widely used to represent adsorption equilibrium in PSA simulation studies due to its mathematical simplicity, thermodynamic reliability, ability to well fit most type I isotherms over a wide range (Ruthven, 1984) and simple, explicit extension to multi-component system. The Langmuir model assumes:

1. The adsorbed molecule or atom is held at definite, localized sites.

2. Each site can accommodate one molecule or atom.

3. The energy of adsorption is constant over all sites, and there is no interaction between neighboring adsorbates.

The equation is derived based on the concept of dynamic equilibrium between the rates of adsorption and desorption. For pure gas:

$$\frac{q_c}{q_s} = \theta = \frac{bc}{1+bc} \tag{3.1}$$

where q_c is adsorbed phase concentration (based on micropore volume) in equilibrium with gas phase concentration c, q_s is the monolayer saturation capacity independent of temperature, θ is called fractional coverage, and b is the Langmuir constant following Arrhenius temperature dependence:

$$b = b_0 e^{(-\Delta U / RT)} \tag{3.2}$$

At low concentration, the Langmuir isotherm approaches the Henry's law limit:

$$q_c = \lim_{c \to 0} \frac{(bq_s)c}{1+bc} = (bq_s)c = K_c c \tag{3.3}$$

For gas mixture adsorption, the Langmuir model can be extended based on the assumption that the components have the same saturation capacity (q_s):

$$\frac{q_i}{q_s} = \frac{b_i c_i}{1 + \sum_{i=1}^{n} b_i c_i} \tag{3.4}$$

$$b_i = (b_0)_i e^{(-\Delta U_i / RT)} \tag{3.5}$$

3.1.2 Langmuir Model Parameters from Linear Regression

Eq (3.1) can be rearranged to the following form:

$$\frac{c}{q} = \frac{c}{q_s} + \frac{1}{bq_s} = \frac{c}{q_s} + \frac{1}{K_c} \tag{3.6}$$

For data conforming to Langmuir model, plot of $\frac{c}{q}$ vs. c is expected to give straight line, the inverse of the slope and intercept of which give q_s and K_c, respectively. Figure 3.1 shows the results of c/q vs. c plots at different temperatures for argon adsorption in Takeda II. The plots are practically parallel, which suggests constant q_s, independent of temperature, and is consistent with the assumption of the Langmuir model. The intercepts of these plots give K_c at different temperatures. Figure 3.2 shows semilogarithmic plot of b ($=K_c/q_s$) vs. $\frac{1}{T}$, from which b_0 and ΔU were extracted

according to Eq (3.2). A summary of these equilibrium parameters is given in Table 3.1.
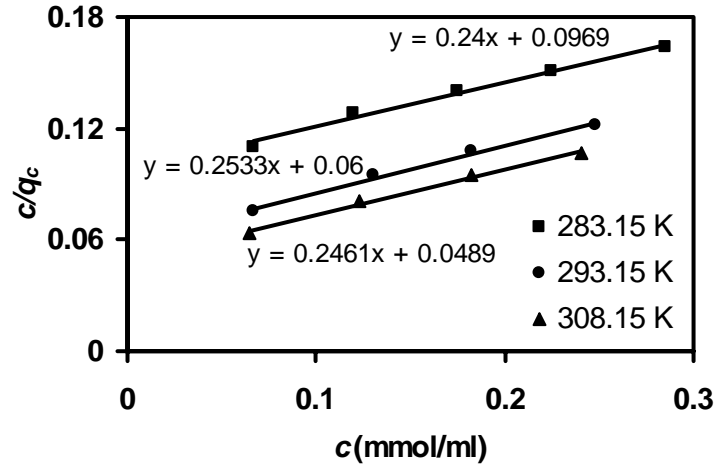
Figure 3.1 Plots of c/q_c vs. c.
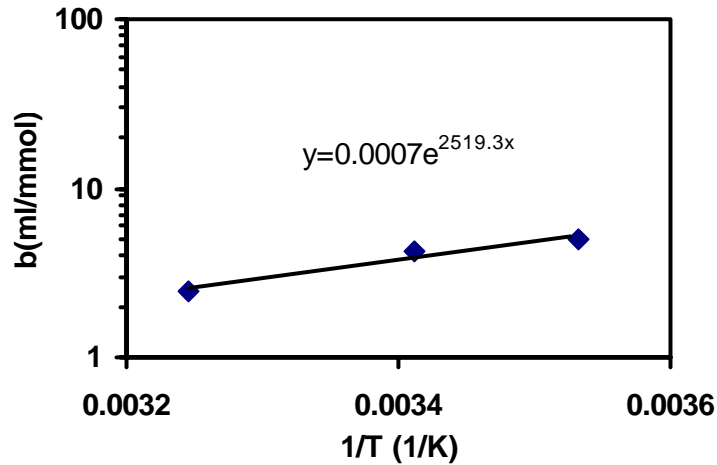
Figure 3.2 Temperature dependence of the Langmuir constant, b.

3.1.3 Langmuir Parameters from Nonlinear Regression

Experimental single component oxygen isotherms in Takeda II CMS up to 8 bar were measured at 253.15, 272.65 and 293.15 K in another study in this laboratory (Huang et al., 2003a). The extended Langmuir model is thermodynamically consistent (Rao and Sircar, 1999) only when the mixture components have the same saturation

capacity ($q_{si} = q_s$). Hence, the model parameters were extracted by performing a simultaneous nonlinear regression of the data for both oxygen and argon at different temperatures, subject to the constraint that both gases have the same saturation capacity, q_s.

Table 3.1 Langmuir isotherm parameters.

Adsorbate		b_0	$-\Delta U$	q_s
O$_2$	Non-	3.585	3.950	4.475
Ar	Linear	1.630	4.451	
Ar(283K)				4.063
Ar(293K)	Linear	0.7	4.727	3.948
Ar(308K)				4.167

b_0: 10^{-3} cc/mmol
q_s: mmol/cc
ΔU: kcal/mol

The following nonlinear objective function was used:

$$\text{Minimize } \sum_i \left[\frac{(q_{O_2})_i}{q_s} - \frac{(b_0)_{O_2} e^{-(\Delta U)_{O_2}/RT}(C_{O_2})_i}{1+(b_0)_{O_2} e^{-(\Delta U)_{O_2}/RT}(C_{O_2})_i} \right]^2$$

$$+ \sum_j \left[\frac{(q_{Ar})_i}{q_s} - \frac{(b_0)_{Ar} e^{-(\Delta U)_{Ar}/RT}(C_{Ar})_j}{1+(b_0)_{Ar} e^{-(\Delta U)_{Ar}/RT}(C_{Ar})_j} \right]^2 \tag{3.7}$$

where *i, j* denote the number of data points. The above function was minimized by varying five parameters, $(b_0)_{O_2}$, $(b_0)_{Ar}$, $(\Delta U)_{O_2}$, $(\Delta U)_{Ar}$ and q_s using the optimization routine "Solver" available in Microsoft Excel XP. The obtained parameters are also listed in Table 3.1. Figure 3.3 shows the optimized model fits to experimental isotherms of pure oxygen and argon. These parameters obtained by single component measurement were directly used to predict the binary equilibrium in this study. Thus,

adsorption equilibrium of oxygen and argon mixture at any temperature, pressure and mole ratio could be directly calculated.
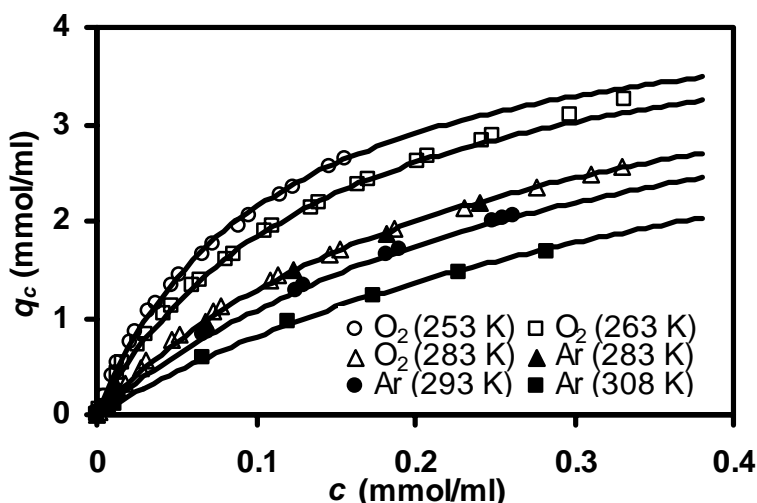
Figure 3.3 Experimental single component isotherms of oxygen and argon in Takeda II CMS are compared with Langmuir model fits. Oxygen data are from Huang et al., 2003a.

As mentioned in Section 3.1.1, the Langmuir model reduces to Henry's law in the low-concentration region and the product of b and q_s gives K_c. The calculated K_c values of Ar in Takeda II CMS at 283.15, 293.15 and 308.15 K are 20.5, 15.6 and 10.7, respectively. They are in good agreement with the Henry's law constants obtained directly in the linear range study described in Chapter 2 (20.6, 15.7 and 10.6 at 283.15 293.15 and 308.15K, respectively).

3.2 Kinetics

3.2.1 Uptake at Different Surface Coverage

Differential uptake measurements of argon in Takeda II CMS were conducted at various levels of adsorbent loading at 293 K. Representative experimental results are compared with the optimized dual model fit in Figure 3.4. The extracted
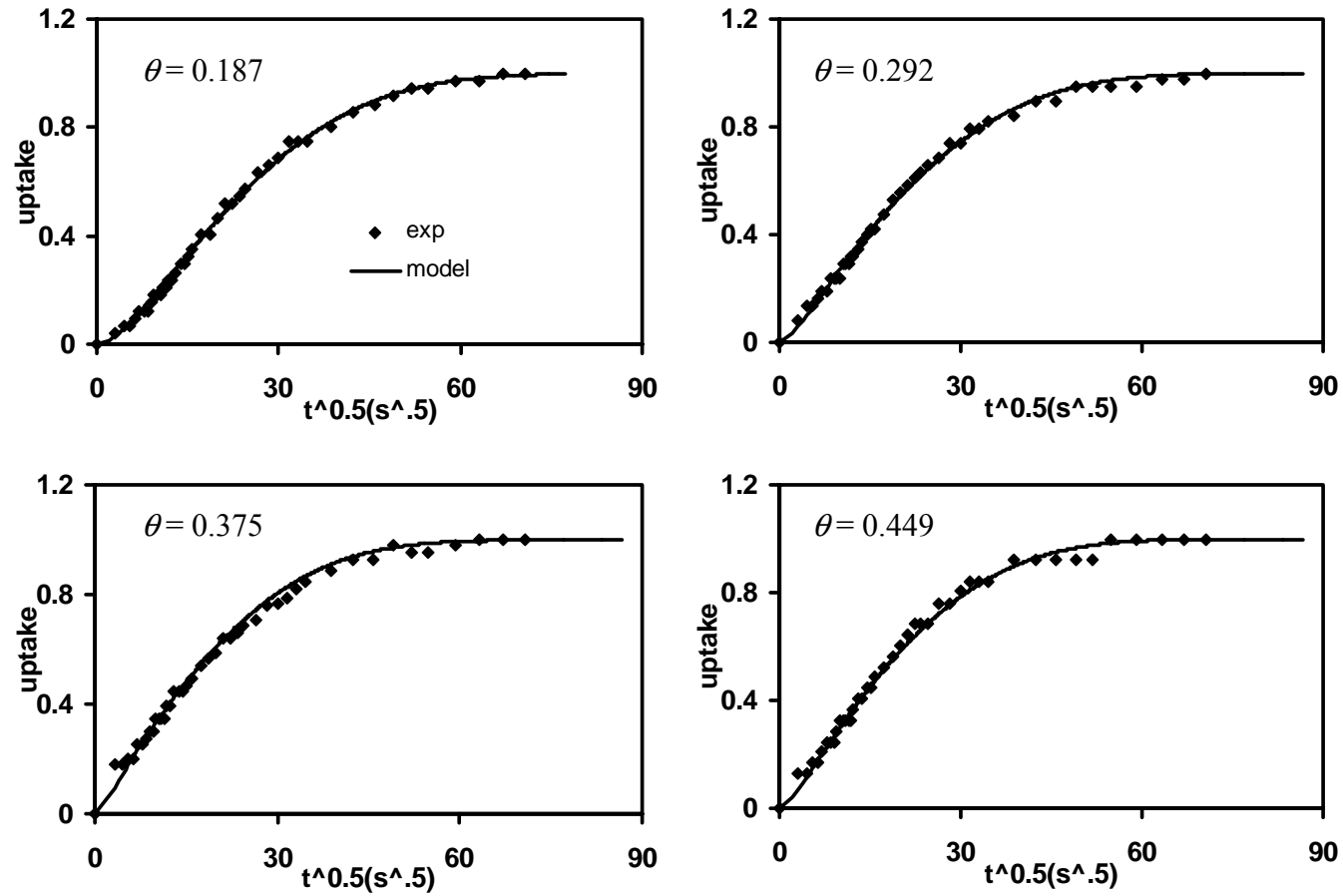
Figure 3.4 Fractional uptake curves of argon in Takeda II CMS at different levels of surface coverage. Symbols are experimental data and the lines are the optimized fits of the dual model.

parameters are listed in Table 3.2. The S-shape in the early part of the uptake curves in CMS samples in the linear range (Chapter 2) is still valid at high coverage. However, as the adsorbent loading is increased, the S-shape of the uptake curve becomes less obvious and the calculated $L/5$ value (introduced in Section 2.6) increases. These suggest that the importance of barrier resistance across the micropore mouth diminishes with increasing adsorbent loading, which is consistent with the findings in a previous study, for other gases, especially for oxygen (Huang et al, 2003a). Based on this observation and considering the pore model as an extreme case of dual model, the obvious conclusion is that the dual model provides a unified approach to capture the uptake behavior of argon in Takeda II CMS sample in the entire range.

Table 3.2 Obtained transport parameters of Ar in Takeda
II CMS at different loadings (293.15K).

θ	0.01	0.187	0.292	0.375	0.449
$D_c/r_c^2\,(10^{-4}\mathrm{s}^{-1})$	0.844	1.05	1.09	1.26	1.28
$k_b\,(10^{-3}\mathrm{s}^{-1})$	2.07	4.64	11.3	14.5	25.2
$L/5$	1.63	2.95	6.9	7.67	13.1

3.2.2 Concentration Dependence of Transport Parameters

The obtained transport parameters compiled in Table 3.2 are plotted as a function of surface coverage (θ) in Figure 3.5. θ values were chosen at the middle of the adsorbed concentration steps for kinetic measurement. It is obvious that both k_b and D_c/r_c^2 are increasing functions of the adsorbed phase concentration.

This concentration dependence of transport parameters was systematically studied in another study conducted in this laboratory (Huang et al., 2003a; Huang et al, 2003b), which was introduced in Section 1.4. The proposed approach to account for

this stronger concentration dependence was also discussed in Section 1.4. The equations are repeated here for easy reference:

$$D_c = D_{c0} \frac{1}{1-\theta} \tag{3.8}$$

$$D_{c0} = D_{c0}^* \left(1 + \beta_p \frac{\theta}{1-\theta}\right) \tag{3.9}$$

$$k_b = k_{b0} \frac{1}{1-\theta} \tag{3.10}$$

$$k_{b0} = k_{b0}^* \left(1 + \beta_b \frac{\theta}{1-\theta}\right) \tag{3.11}$$

Eqs (3.8) and (3.10) follow from chemical potential gradient as driving force for diffusion for a Langmuir isotherm system. Eqs (3.9) and (3.11) account for the concentration dependence of the thermodynamically corrected transport parameters, D_{c0} and k_{b0}. D_{co}^* and k_{b0}^* are the limiting transport coefficients measured in the linear range of isotherm (i.e., $\theta \to 0$). The values of β_p and β_b were extracted by optimizing the fitting of Eqs (3.8) and (3.9) to the $\dfrac{D_c}{D_{co}^*}$ vs. θ plot and Eqs (3.10) and (3.11) to $\dfrac{k_b}{k_{bo}^*}$ vs. θ plot as shown in Figure 3.5. The transport parameters of argon at 293.15 K obtained in this study are summarized in Table 3.3, together with those of oxygen from a previous study referred earlier.
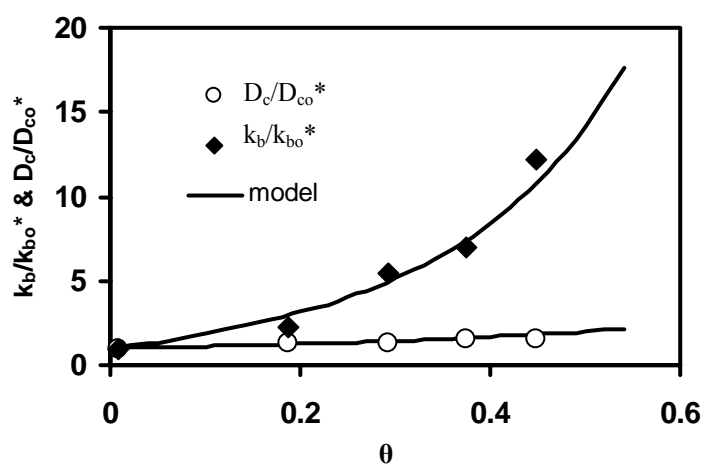
Figure 3.5 Concentration dependence of transport parameters of argon in Takeda II CMS at 293.15 K.

Table 3.3 Kinetic parameters of Ar and O_2 on Takeda II CMS.

Adsorbate	D_{c0}^{*}/r_c^2 $(10^{-4}s^{-1})$	k_{b0}^{*} $(10^{-3}s^{-1})$	β_b	β_p
Oxygen[1]	85.3	98.4	5.56	0
Argon	0.844	2.07	6.08	0

1: O_2 data are from Huang et al., 2003a.

Chapter 4   PSA Experiments

A comprehensive PSA study involves both simulation and experimental work. In this study, PSA experiments for argon production operated on a modified Skarstrom cycle were first conducted in the transatmospheric pressure range with adsorption at about 3 atm and desorption at different pressures lower than 1 atm. Then a bidispersed PSA model was used to capture the experimental phenomena. Upon model validation, further simulation was carried out to investigate feasible cycles for different product requirements and identify more favorable operating zones.

The experimental PSA set-up used in this study and detailed experimental procedure are presented in this chapter. Some of the experimental results are also briefly reported.

4.1 Skarstorm Cycle

Skarstorm cycle is one of the earliest developed PSA cycles for highly pure raffinate product. A typical Skarstorm cycle involves two beds and four steps, namely, pressurization, high pressure adsorption, blowdown and counter-current purge. The sequence of operation in a Skarstrom cycle is show in Figure 4.1. In step 1, bed 2 is pressurized with feed while bed 1 is blown down to the lower operating pressure. In step 2, the high-pressure feed flows through bed 2 where the more strongly adsorbed or faster diffusing component is preferentially removed, leaving a raffinate product enriched with the weekly adsorbed or slower component. At the same time, a fraction of the product from bed 2 is used to purge the product end of bed 1 at the lower operating pressure to improve the product purity of bed 1 in the next cycle. Step 3 and step 4 follow the same sequence but with the beds interchanged.
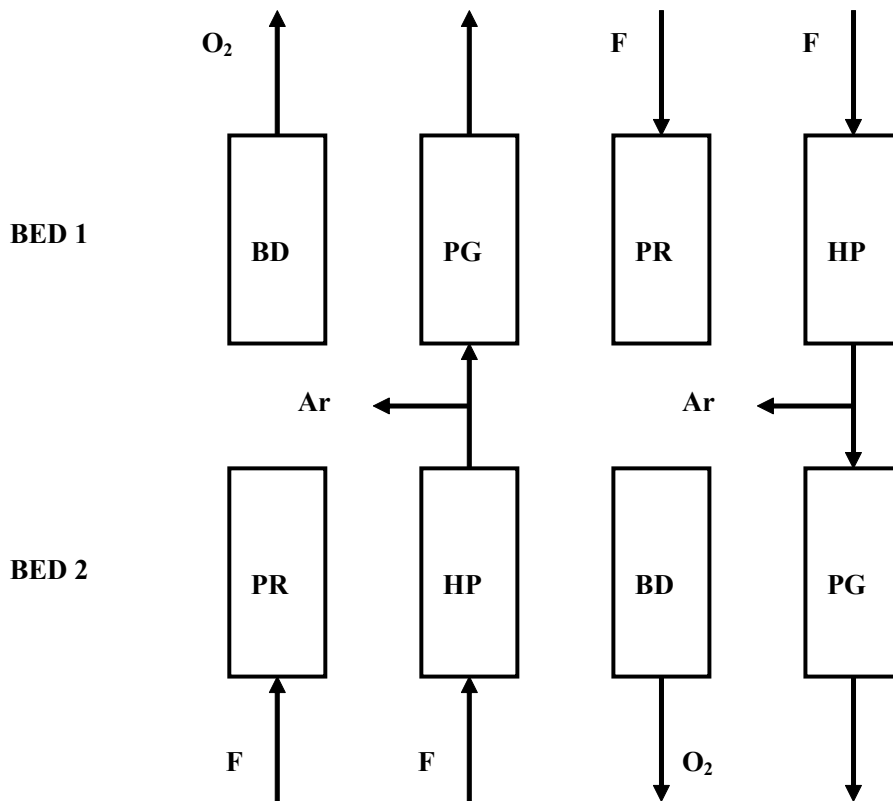
Figure 4.1 Schematic diagram of a Skarstrom cycle. PR: pressurization; HP: high pressure adsorption; BD: blowdown; PG: purge. F: feed mixture.

4.2 Modified Skarstrom Cycle (without External Purge)

For a kinetically controlled PSA process, to purge the product end using the product (the slower component) from another bed is not necessary. This is because the desorption of the slower component is diffusion controlled and lowering its partial pressure by purging with a stream enriched in the faster component is not beneficial for enhancing regeneration. By simply closing the product end and withdrawing gas from the feed end at low operating pressure, the faster component comes out first followed by the slower component, which acts to clean the faster component out of the void space in the column. This is known as self-purge operation exploited by kinetically controlled PSA separation (Ruthven et al., 1994a). Besides the improvement of concentration profile in the bed, self-purge, compared with external purge, has the

advantage that, since no extra slower component is introduced in the bed and adsorbed by the particles, the capacity for the faster component during the next cycle is enhanced. Moreover, the recovery of raffinate product is, of course, enhanced, which is especially important for the system in this study where the slower component, argon, only accounts for 5 percent in the feed mixture. Any possibility to save the product is thus highly preferable.
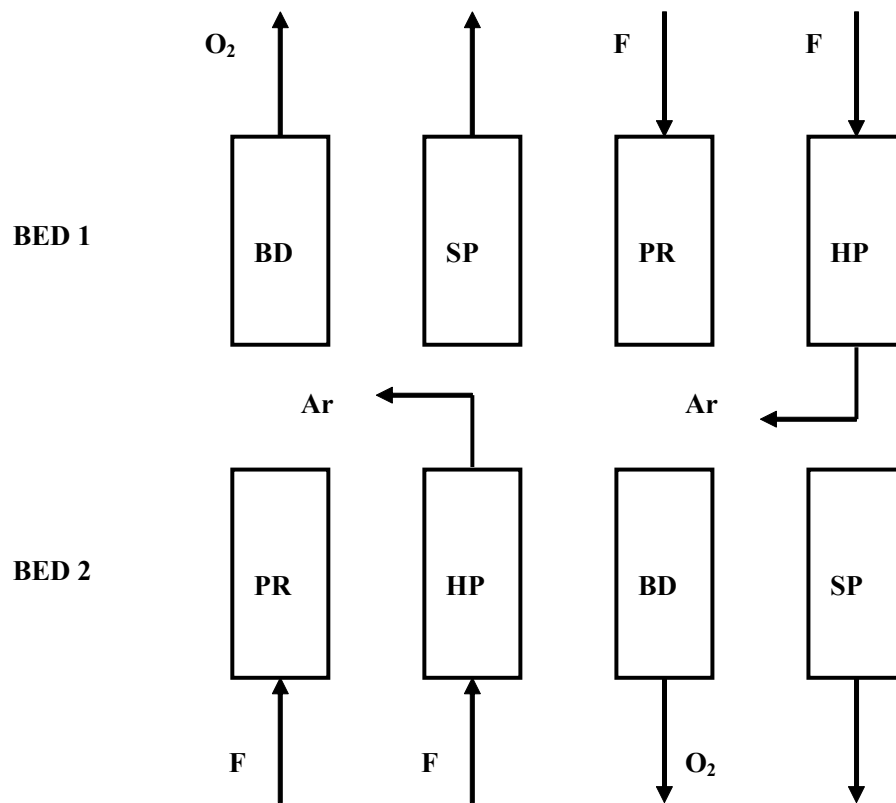
Figure 4.2 Schematic diagram of Skarstrom cycle without external purge showing that the two beds work independently. PR: pressurization; HP: high pressure adsorption; BD: blowdown; SP: self-purge. F: feed mixture.

As may be seen from Figure 4.2, without any external purge, the two beds in the Skarstorm cycle are completely independent. Hence, to understand the characteristics of the separation process, experimental and simulation study using only one bed is sufficient. Also, the operations of blowdown and self-purge steps are exactly the same and these two steps can be combined in the experimental study as well as in

the simulation. Hence, in this study, a single-bed, 3-step cycle as shown in Figure 4.3, was used for O_2-Ar separation. The 3-step cycle is significantly simpler and has the flexibility of varying the duration of the low pressure step (combined blowdown and self-purge steps in this case), independent of the high pressure steps.
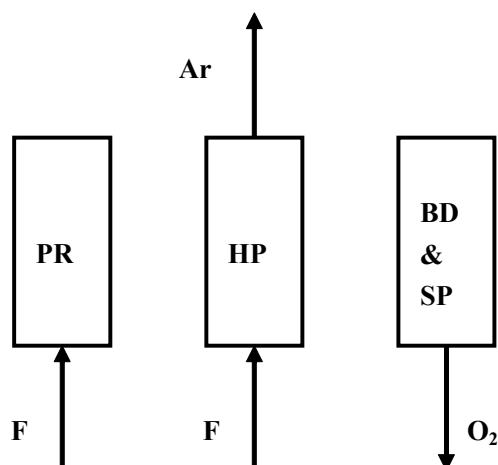
Figure 4.3 Schematic diagram of single-bed, 3-step cycle. PR: pressurization; HP: high pressure adsorption; BD: blowdown; SP: self-purge. F: feed mixture.

It should, however, be noted that a product tank must be used in a single-bed operation, if a continuous product flow supply is desired. The use of product tank will affect the approach to steady state, not the steady state performance.

4.3 PSA Experimental Setup

A schematic diagram of the experimental setup is shown in Figure 4.4. The original set-up was built in this laboratory with a 6-bed system for hydrogen purification study (Malek, 1996a). The modification of the original system to a two-bed system for kinetically controlled air separation study has been detailed by Gupta (2000). In this study, the set-up was further modified for single-bed operation in the range of $0-3$ atm. Some of the important features incorporated for the convenience of vacuum operation are highlighted here.
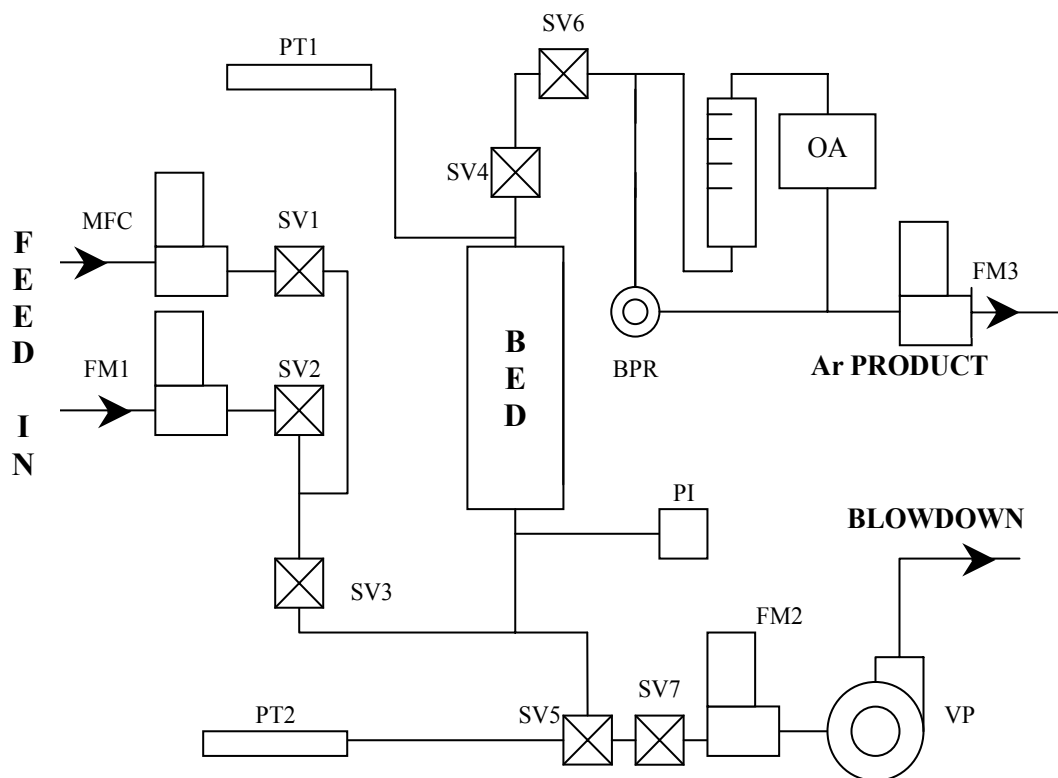
Figure 4.4 Schematic diagram of the experimental PSA set-up for a single-bed, 3-step cycle.

The adsorption column packed with Takeda II was taken from a previous study (Huang et al, 2002). Some relevant data on the column and adsorbent used are compiled in Table 4.1. During the experiments, the column was immersed in a temperature controlled water bath, which was also used in the DCBT study discussed earlier (Section 2.5), to maintain a constant temperature (20 ^{0}C).

The system had three main pipelines, namely, the product line connected to the top of the column, the feed line and the blowdown line connected to the bottom of the column. A back pressure regulator (GO BP3), BPR, was installed at the end of product line to maintain the high process pressure, which was maintained at ~3 atm. The blowdown line was connected to a vacuum pump (Edwards, two-stage, Model M3), VP, to obtain low subatmospheric pressure for effective regeneration. The feed and blowdown lines in the original setup were mainly 1/8 inch stainless steel tubes. Some of them were replaced by 1/4 inch PVC tubes as short as possible to reduce the pipeline

resistance. For vacuum operation, giving very small pressure driving force, the line resistance was still significant and the lowest pressure achieved in the column depended on the duration of the combined blowdown and self-purge steps.

Table 4.1 Adsorption column used in PSA experiments.

Column	Stainless steel
Bed Inside Radius	1.9 cm
Bed Length	40 cm
Bed voidage	0.35
Adsorbent	Takeda II Carbon Molecular Sieve
Particle Radius	0.159 cm
Particle Voidage	0.33
Feed	Oxygen and Argon Mixture
Mole Ratio	95 : 5 (O_2 : Ar)

The operation of switching from one step to the next in the PSA process was realized by controlling seven DC-operated Honeywell Skinner ON/OFF valves (SV1 - SV7). The valve operation and control will be discussed in Section 4.4.

Three mass flow meters, FM1 (Brooks Model 5861E, 0-12 SLPM) FM2 (Brooks Model 5861E, 0-100 SLPM), and FM3 (Microbridge, AWM5103N, 0-15 SLPM), were used to measure the flow rates of pressurization gas, product gas and blowdown gas, respectively. A mass flow controller, MFC (Brooks Model 5850E, 10 SLPM air), controlled by a Brooks 0152 panel, was used to control required feed flow rate (from a high pressure cylinder containing mixture gas) for the high pressure adsorption step. MFC was calibrated using a wet gas meter (100 ml) and a stop watch (with an accuracy of 0.01 s). FM1, FM2 and FM3 were calibrated using Humonics Optiflow 730 Digital Flowmeter (250 l/min).

Two pressure transducers were involved in the PSA experiments. PT1 (E&H Cerabar, 20 bar abs.) was directly connected to the column and there was no flow in

the small connecting tube. PT2 (TransInstrument, 6 bar abs.) served the dual purpose of measuring the pressure in the feed line during the pressurization and high pressure adsorption steps, and the pressure in the blowdown line during the blowdown step. These two pressure transducers were calibrated by a Fluke 716 pressure calibrator. This pressure calibrator, PI, was also directly connected to the bottom of the column during the PSA experiments. The locations of the pressure measurements are shown in Figure 4.4.

Oxygen concentration in the product was measured by a Servomex Oxygen Analyzer (Model 572), OA.

All the six measuring instruments, FM1, FM2, FM3, PT1, PT2 and OA, gave voltage outputs, which were read by a 12-bit A/D data acquisition card installed in an Intel Pentium 75 MHz personal computer. Between the measuring instruments and the data acquisition card was a connector with 8 connecting pins (numbered from 0 to 7), which were used to transfer the signals from those measuring meters to the card. The signals were collected in a data file and could also be directly monitored on the screen. On-screen display was useful to calibrate the measuring instruments. The switching of the solenoid valves was also controlled by this computer. The entire data acquisition/control system was programmed using Microsoft Visual Basic code.

4.4 Experimental Procedure

Preparation: The column packed with Takeda II CMS adsorbent particles was regenerated at 200 $^{\circ}$C for more than 8 hours with a continuous purge of helium, which is necessary to prevent the CMS structure from being damaged in an oxygen environment at high temperature (Huang et al., 2003a). The column was then cooled down to the room temperature under helium purge after which it was immersed in a constant temperature bath maintained at the desired experimental temperature.

Sufficiently long time was allowed to ensure thermal equilibrium between the column and the bath. During this period, the experimental column and the associated pipeline were pressurized to 6 bar with helium to check leakage. Before each PSA experimental run, the column was equilibrated with the feed mixture (95% O_2 and 5% Ar) at the high operating pressure (~3 atm).

Blowdown step: The cycle began with the blowdown step for a pre-determined duration. The vacuum pump, VP, which was connected to the blowdown line, provided nearly absolute vacuum (less than 10 mbar) to improve the effectiveness of blowdown. However, as mentioned earlier, due to the high line resistance relative to the low pressure driving force in the vacuum range, the lowest pressure of operation depended on the duration of blowdown step rather than on the vacuum level attained by the vacuum pump. Since the pump inside the Oxygen Analyzer was not strong enough to collect sample from a vacuum system, it was not possible to measure the oxygen concentration in the exit stream during this step. Only blowdown flow rate and system pressure were recorded as functions of time.

Pressurization step: The feed gas cylinder connected to the flow meter, FM1, was set at the highest pressure of operation (~3 atm) in order to limit the pressure rise to the desired level of high pressure operation. The determination of pressurization step duration was based on two considerations. If the duration was too short, the column would not be pressurized to the desired level due to the pipeline resistance. The line resistance limited the flow rate. Moreover, the faster component, oxygen, accounted for 95% in the feed mixture. These two factors contributed to the slower rate of pressurization. On the other hand, if the duration was too long, the adsorbent particles in the bed would be nearly saturated with oxygen, leaving very little capacity for the adsorption step, thus decreasing the product purity. After some trial runs, a

pressurization duration of 100 s was found reasonable and kept fixed in all the runs. During this step, the inlet flow rate and system pressure were recorded.

High pressure adsorption step: The feed gas cylinder connected to the mass flow controller, MFC, was set to be about 6 atm, which was necessary to ensure desired constant flow of feed mixture into the column maintained at 3 atm. The high pressure feed flow rate was controlled at 25 cm^3/s (at 1atm). During this step, the system pressure, product flow rate and oxygen concentration in the product stream were recorded.

The control of solenoid valves to realize the operation of each step is introduced in the next section. Five experimental runs were conducted in this study.

4.5 Valve Operation and Control

The switching of the solenoid valves was controlled using two 24-bit digital I/O card (PC LabCard Model 724). In the program, they were named as Port 1 and Port 2, each connected to a 24-channel Form C power relay output board (PC-LabCard Model 7225). The 24 channels in each port were equally divided into 3 groups, G0, G1 and G2. The above provisions were created for operating the original 6-bed process. For the single-bed, 3-step process used in this study, only seven solenoid valves were necessary. Every valve was controlled by specifying three identities, Port (1-2); Group (0-2); Valve No (0-7). The state of each valve was represented by one of the bits (0-7) in the 8-bit signal. The signals were given in the form of binary digits with 1 for 'off' and 0 for 'on'. Each line in the program was able to control up to 8 valves located in one group. Following is an example of one such line:
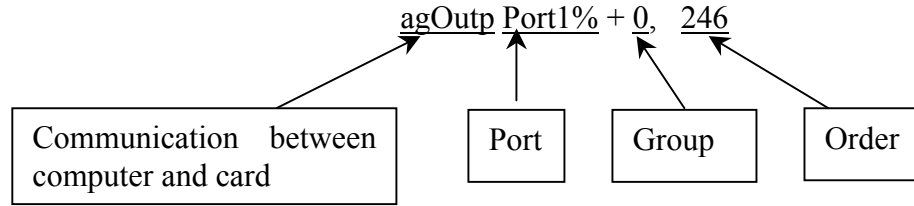
When all 8 valves in one group were off i.e. all binary digits were assigned 1, the order value (OV) was 255 ($= \sum_{N=0}^{7} 2^N$). Opening a valve numbered N was done by subtracting 2^N from the initial order value. For example, to open valve No. 0 and valve No. 3 would mean OV, $246 = 255 - 2^0 - 2^3$. As already mentioned, there were many valves in the PSA panel that were not used in the present study and these were left in the 'off' position. The locations of the seven valves involved in this study are listed in Table 4.2 and valve controls for each operating step are shown in Table 4.3.

Table 4.2 Valve locations.

SV	Port	Group	No.	2^N
1	1	0	0	1
2			3	8
3	2	0	0	1
4			2	4
5			4	16
6		1	2	4
7			3	8

Table 4.3 Valve control of each step of the single-bed, 3-step cycle.

	Port1/Group0			Port2/Group0				Port2/Group1		
	SV1	SV2	OV	SV3	SV4	SV5	OV	SV6	SV7	OV
BD	×	×	255	×	√	√	235	×	√	247
PR	√	×	254	√	√	√	234	×	×	255
HP	×	√	247	√	√	√	234	√	×	251

4.6 Data Analysis

The analog signals measured from all the six measuring instruments, FM1, FM2, FM3, PT1, PT2, and OA, were stored in a data file as functions of time. These values were then converted to the appropriate dimensional forms (cm^3/sec for flow rates, bar for pressures and mole fraction for concentration) using calibration equations obtained independently.

PSA performance was evaluated by purity, recovery and productivity of Ar product at steady state. These were calculated using the following integral equations:

$$purity = \frac{\int_0^{t_h} x_A F_r dt}{\int_0^{t_h} F_r dt} \times 100\% \qquad (4.1)$$

$$re\,cov\,ery = \frac{\int_0^{t_h} x_A F_r dt}{\left[F_{pr} t_{pr} + F_{fd} t_{hp}\right] x_{feed}} \times 100\% \qquad (4.2)$$

$$productivity = \frac{\int_0^{t_h} x_A F_r dt}{\left(t_{bd} + t_{pr} + t_{hp}\right) V_{ads}} \qquad (4.3)$$

% mass balance error in each run was calculated from the following equation:

$$Mass\ \ balance\ \ error = \frac{\int_0^{t_l} F_{bd} dt + \int_0^{t_h} F_r dt - \left[F_{pr} t_{pr} + F_{fd} t_{hp}\right]}{\left[F_{pr} t_{pr} + F_{fd} t_{hp}\right]} \times 100\% \qquad (4.4)$$

In above equations, adsorbent volume (V_{ads}) and feed concentration (x_{feed}) were fixed system parameters. Feed flow rate (F_{fd}) was controlled by the mass flow controller, FMC. The durations of different operation steps (t_{pr}, t_{hp} and t_{bd}) were input

parameters to the Visual Basic program. The raffinate product flow rate (F_r) and concentration (x_A), blowdown flow rate (F_{bd}), and pressurization flow rate (F_{pr}) were captured by the data acquisition system, as described in the previous section.

Microsoft Excel (XP Professional version) was used to integrate the above functions.

4.7 Experimental Profiles

Shown in this section are some representative transient and steady state profiles of flow and pressure that were recorded online at different positions during the course of an experimental run.

Figure 4.5 shows the steady state flow profiles measured by three flow meters (FM1, FM2 and FM3). As expected, during pressurization and blowdown step, the flow rate was very high at the beginning followed by a sharp drop. During the high pressure adsorption step, the product flow rate dropped initially before increasing continuously with time until the end of this step.

The locations of the pressure measurements were discussed in Section 4.3 and are clearly shown in Figure 4.4. It should be noted that PT2 and PI were measuring pressures at different points on the same pipeline that supplied gas to the column during the pressurization and high pressure adsorption steps, and carried gas out of the column during the counter-current blowdown step. The recorded pressure profiles at these three positions are plotted together in Figure 4.6 for one experimental run to better understand the pressure drops in the system. It may be seen in Figure 4.6 that the pressure profiles recorded by PT1 and PI completely overlap with each other, which indicates negligible pressure drop within the column during all the three steps. Another observation from Figure 4.6 is the deviation between the pressure profiles recorded by PT2 and PI (located on the same pipeline) during the early parts of the pressurization

and blowdown steps, which is consistent with the high flow rate (and therefore high velocity) in the early parts of these steps. It is clear that the faster pressurization and blowdown could be achieved by reducing the line resistance. It was discussed in Section 4.3 that some improvement in this regard was achieved by replacing the original $\frac{1}{8}$ " tubes with $\frac{1}{4}$ " tubes. Further improvement was not possible without major reconstruction of the set-up.

Figure 4.7 shows the approach of the product purity to steady state for a representative experimental PSA run. It can be clearly seen in Figure 4.7 that the cyclic steady state is reached in less than 10 cycles. Hence, the subsequent PSA experimental runs were conducted for 15 cycles.

A summary of the experimental results of all the five runs conducted are given in Table 4.4. The experimental PSA performance as well as profiles will be compared with the theoretical predictions for the validation of the PSA simulation model in the next chapter.
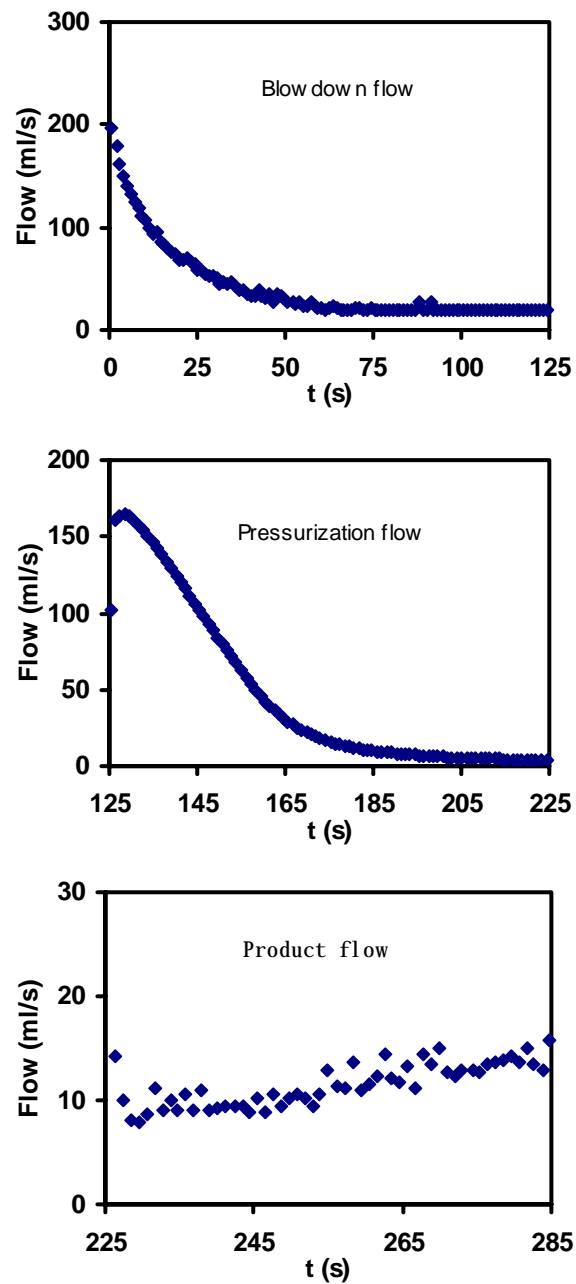
Figure 4.5 Experimental flow profiles during each of the three steps for a representative run. Blowdown: 125 s; Pressurization: 100 s; High pressure adsorption: 60 s. Flow rates are based on 1 atm pressure.
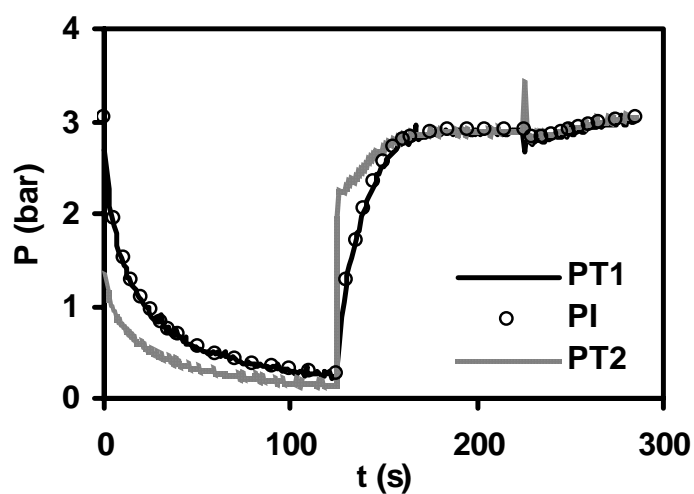
Figure 4.6 Experimental pressure profiles measured at different positions showing the pressure drops. Please see Figure 4.4 for the locations of the pressure measurements.
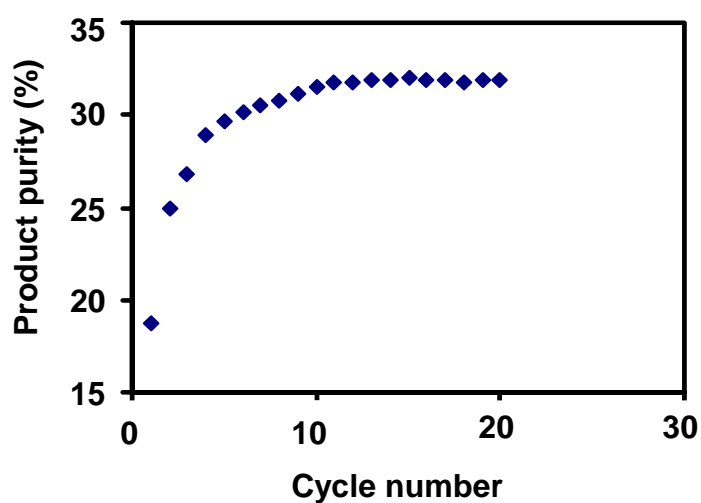
Figure 4.7 Approach of the purity of argon product to steady state. Blowdown: 125 s; Pressurization: 100 s; High pressure adsorption: 50 s.

Table 4.4 Summary of the experimental results of the single-bed, 3-step cycle for argon production.

Run No.	BD (s)	HP (s)	Gas going out of the bed during BD (cm^3)	Gas going into the bed during PR (cm^3)	Gas going into the bed during HP (cm^3)	Gas going out of the bed during HP(cm^3)	Ar going out of the bed during HP (cm^3)	Mass balance error (%)	Argon product		
									Purity (%)	Recovery (%)	Productivity (cc/hr/cc ads.)
1	125	70	4578.2	5220.5	1750	782.7	228.7	-5.14	29.1	72.9	11.2
2	125	60	5209.6	4566.3	1500	684.4	210.5	-2.84	30.6	68.8	10.3
3	125	50	5186.0	4656.5	1250	545.2	174.1	-2.97	31.9	58.9	8.5
4	150	50	5657.4	4738.9	1250	475.7	158.3	2.41	33.0	52.8	7.7
5	100	50	4639.7	4356.9	1250	551.7	173.6	-6.44	31.4	62.2	8.4

BD: blowdown step; HP: adsorption step; Pressurization step (PR): 100 s; High operating pressure: ~3 atm; Feed flow rate: 25 cm^3/s. The gas volumes are based on 1 atm pressure. Nearly absolute vacuum was achieved at the end of the blowdown line.

Chapter 5   PSA Simulation Study

The PSA experimental study is time consuming and difficult to conduct. Also, the PSA performance normally depends on the effects of many process variables coupled in a complex way, which restricts the possibility of optimizing the performance of a PSA process with limited experimental PSA results. Hence, reliable mathematical models are desired as a convenient tool for the design and analysis of PSA processes. In this chapter, a suitable model is first developed for the single-bed, 3-step PSA cycle for argon separation from its mixture with oxygen detailed in the previous chapter. The model predictions, using independently established equilibrium and kinetic parameters, are then compared with the experimental results. The experimentally verified model is then used to conduct an extensive study to understand the effects of various process parameters on the performance of the PSA cycle. Simulations are also carried out to investigate other cycle configurations for oxygen-argon separation.

5.1 Bidispersed PSA Model with Dual Resistance for Micropore Transport

A bidispersed PSA model including dual transport resistance in the micropores has been developed in this laboratory and applied to the study of kinetically controlled air separation on a CMS sample (Farooq et al., 2001). It was shown in chapter 3 that the kinetics of Ar in the micropores of Takeda II CMS also showed dual transport resistance. The PSA model of Farooq et al. (2001) was modified in this study to simulate the single-bed, 3-step PSA cycle for oxygen-argon separation experimentally studied in chapter 4. A detailed description of the PSA model is presented below:

5.1.1 Basic Assumptions

The following assumptions were made, many of which are common with many published PSA models:

(1) The ideal gas applies.

(2) The system is isothermal. The column was immersed in a water tank of constant temperature during the PSA experiments. Hence, it was reasonable to assume that heat effect, if any, did not have any major impact.

(3) Flow pattern is axially dispersed plug flow.

(4) Frictional pressure drop along the column is negligible.

(5) Langmuir isotherm applies.

(6) Adsorbent particles are spherical.

(7) Molecular diffusion dominates in macropores.

(8) Transport in micropores follows a dual resistance model in which a barrier resistance is confined at the pore mouth followed by a distributed diffusional resistance in the micropore interior.

(9) Chemical potential gradient is the driving force for micropore transport and the thermodynamically corrected transport parameters are also strong functions of adsorbent loading.

(10) The column pressure remains constant during adsorption and external purge steps (if any).

5.1.2 Model Equations

The mathematical representation of an isothermal PSA process is simply a series of mass balance equations. Flow from the feed end (0) to the product end (*L*) of the column is taken as positive. Flow from *L* to 0 is negative. Assigning sign to velocity based on the flow direction allows using the same component mass balance

equation for both forward and reverse flow steps. Only the boundary conditions are different.

5.1.2.1 Mass Balance in the Fluid Phase

1. Fluid phase component mass balance:

$$-D_L\frac{\partial^2 c_i}{\partial z^2}+\frac{\partial c_i v}{\partial z}+\frac{\partial c_i}{\partial t}+\frac{1-\varepsilon}{\varepsilon}\frac{\partial \overline{\overline{q_i}}}{\partial t}=0 \tag{5.1}$$

where c_i (mmol/ml) is the fluid phase concentration of component i (normally, A for the slower component and B for the faster), v (cm/sec) is the fluid velocity and $\overline{\overline{q}}_i$ (mmol/ml) is the average concentration in adsorbed phase. These three variables are all functions of time, t (sec), and axial position in the adsorption column, z (cm). The effects of all mechanisms that contribute to axial mixing are lumped into a single effective axial dispersion coefficient, D_L (cm^2/sec). ε is the bed voidage and is dimensionless. The four terms in the above equation represent axial dispersion, convection, accumulation in the fluid phase and adsorption by the adsorbent particles, respectively, for component i.

2. Continuity condition

$$\sum_i c_i = c_A + c_B = C \tag{5.2}$$

where C (mmol/ml) is the total concentration in gas phase. Based on assumptions 1, 2 and 4, it is independent of z ($\frac{dC}{dz}=\frac{1}{RT}\frac{dP}{dz}=0$). Based on assumption 10, it is constant during the high pressure adsorption step and changes with time during the pressurization and blowdown steps.

3. Overall mass balance

$$-D_L \frac{\partial^2 C}{\partial z^2} + \frac{\partial Cv}{\partial z} + \frac{\partial C}{\partial t} + \frac{1-\varepsilon}{\varepsilon} \sum_i \frac{\partial \overline{\overline{q_i}}}{\partial t} = 0 \qquad (5.3)$$

Eq (5.3) is simply the summation of Eq (5.1) for all the components in the mixture. As a result, it is necessary to solve only one component balance equation in a binary system. Here the slower component balance equation was solved. Since the total concentration is assumed to be independent of z ($\frac{dC}{dz} = 0$), the dispersion term can be eliminated from Eq (5.3) and the convection term becomes $C\frac{\partial v}{\partial z}$. Hence, in this model, Eq (5.3) reduces to:

$$C\frac{\partial v}{\partial z} + \frac{\partial C}{\partial t} + \frac{1-\varepsilon}{\varepsilon} \sum_i \frac{\partial \overline{\overline{q_i}}}{\partial t} = 0 \qquad (5.4)$$

For a binary system, the above three equations, (5.1), (5.2) and (5.4), are used to solve three unknowns, v, c_A, and c_B, as functions of t and z. The boundary conditions will be presented in a later section. In some studies, axial dispersion has been neglected and the dispersion term has been dropped from Eq (5.1). The average concentrations of A and B in the particle phase, $\overline{\overline{q_A}}$ and $\overline{\overline{q_B}}$, link the fluid phase mass balance equations to the mass balance equations in the adsorbent phase. The solution for total concentration, C, for the variable pressure steps is addressed in Section 5.1.2.3.

5.1.2.2 Mass Balance in Adsorbent Particles

In case of the bidispersed model with dual micropore resistance, $\overline{\overline{q_A}}$ and $\overline{\overline{q_B}}$ have the following forms:

4. Mass transfer rate across the external film

$$\frac{\partial \overline{\overline{q_i}}}{\partial t} = \frac{3}{R_P} k_f \left(c_i - c_{pi}\big|_{R=R_P} \right) = \frac{3}{R_P} \varepsilon_P D_p \frac{\partial c_{pi}}{\partial R}\bigg|_{R=R_p} \tag{5.5}$$

where k_f (s^{-1}) is the transport coefficient for film resistance, D_p (cm^2/s) is macropore

diffusivity, c_{pi} (mmol/ml) is the macropore concentration and is a function of radius

position in the particle, R (cm), and dimensionless ε_p is the particle voidage. In the

above equation, k_f and D_p are considered the same for both components.

5. Macropore mass balance

$$\varepsilon_p \frac{\partial c_{pi}}{\partial t} + \left(1 - \varepsilon_p\right)\frac{\partial \overline{q_i}}{\partial t} = \varepsilon_p D_p \left[\frac{\partial^2 c_{pi}}{\partial R^2} + \frac{2}{R}\frac{\partial c_{pi}}{\partial R} \right] \tag{5.6}$$

where $\overline{q_i}$ (mmol/ml)is the average concentration in micropore (different from $\overline{\overline{q_i}}$).

6. Mass transfer rate across the micropore mouth

$$\frac{\partial \overline{q_i}}{\partial t} = \frac{3}{r_c} k_{bi} \left(q_i^* - q_i\big|_{r=r_c} \right) = \frac{3}{r_c} D_{ci} \frac{\partial q_i}{\partial r}\bigg|_{r=r_c} \tag{5.7}$$

where q_i^* is in equilibrium with macropore concentration, q_i is the distributed

concentration in micropore, k_{bi} and D_{ci} are strongly concentration dependent micropore

transport parameters, which have been experimentally estimated in Chapters 2 and 3.

7. Diffusion in micropore

$$\frac{\partial q_i}{\partial t} = \frac{1}{r^2}\frac{\partial}{\partial r}\left(D_{ci} r^2 \frac{\partial q_i}{\partial r} \right) \tag{5.8}$$

These four equations, (5.5) to (5.8), are used to solve four unknowns, $\overline{\overline{q_i}}$ (t, z),

$c_{pi}(t, z, R)$, $\overline{q_i}$ (t, z, R) and $q_i(t, z, R, r)$, for each component, i. The second parts of Eqs

(5.5) and (5.7) are in fact two other independent equations, which are used as boundary conditions for Eqs (5.6) and (5.8), respectively, which will be discussed in Section 5.1.3. Equations (5.5)-(5.8) are written for all the components in the mixture. For a binary system, there are eight such equations.

5.1.2.3 Equations to Solve Total Concentration in the Fluid Phase

During constant pressure operation, total concentration, C, is a known constant. Two methods can be used to solve C as a function of time during the pressurization and blowdown steps. One commonly used method is to directly give experimental pressure-time history, normally expressed in the exponential forms shown in Eqs (5.9) and (5.10) (Farooq et al., 1993). The other method is to relate the pressurization or blowdown flow rate with column pressure.

Exponentially Changing Pressure History

$$P = f(t) = P_H - (P_H - P_L)e^{-a_1 t} \quad \text{(For pressurization)} \tag{5.9}$$

$$P = f(t) = P_L + (P_H - P_L)e^{-a_2 t} \quad \text{(For blowdown)} \tag{5.10}$$

where P_H and P_L are the high and low pressures of PSA operation; a_1 and a_2 are constants to be empirically determined. Based on the assumptions of ideal gas and isotherm system, C is simply proportional to P and is no more an unknown once the pressure history is given.

Pressurization and Blowdown Flow Rates

$$F_{PR} = v\big|_{z=0} A_B \varepsilon P = f_{PR}(P) \quad \text{(For pressurization)} \tag{5.11}$$

$$F_{BD} = -v\big|_{z=0} A_B \varepsilon P = f_{BD}(P) \quad \text{(For blowdown)} \tag{5.12}$$

where F_{PR} and F_{BD} in cm^3/s are the flow rates at standard pressure, A_B (cm^2) is the bed area. The two functions are system characteristics dependent on the upstream or downstream pressure and pipeline resistance. These functions are also empirically determined from experimental data.

Column mass balance equation

The integration of Eq. 5.4 from $z = 0$ to $z = L$ has the following form:

$$-\frac{v|_{z=0}}{L} + \frac{v|_{z=L}}{L} + \frac{1}{C}\frac{dC}{dt} + \frac{1}{C}\frac{1-\varepsilon}{\varepsilon}\sum \int_0^L \frac{\partial \overline{\overline{q_i}}}{\partial t} dz = 0 \tag{5.13}$$

This equation is called total column mass balance, in that the four terms represent gas going into the column, going out of the column, accumulated in gaseous phase and adsorbed by solid particles, respectively. During the pressurization and blowdown steps, since the product end is closed, $v|_{z=L}$ is equal to zero and Eq (5.13) reduces to the following equation:

$$-\frac{v|_{z=0}}{L} + \frac{1}{C}\frac{dC}{dt} + \frac{1}{C}\frac{1-\varepsilon}{\varepsilon}\sum \int_0^L \frac{\partial \overline{\overline{q_i}}}{\partial t} dz = 0 \tag{5.14}$$

At any time, the adsorption term, $\frac{1}{C}\frac{1-\varepsilon}{\varepsilon}\sum \int_0^L \frac{\partial \overline{\overline{q_i}}}{\partial t} dz$, can be calculated from Eq (5.5). Thus, either $\frac{dC}{dt}$ (or $\frac{dP}{dt}$) or the inlet velocity, $v|_{z=0}$, can be used to calculate the other.

It should be noted that Eq (5.13) is not a new equation but the integration of Eq (5.4). The independent equation affecting the solution of C is, in fact, any one of Eqs (5.9) – (5.12). In constant pressure step, it is replaced by $P = $ constant.

In all, the PSA model has eleven independent equations for a binary system. Correspondingly, there are eleven variables, c_A, C, v, $\overline{\overline{q_i}}$, c_{pi}, $\overline{q_i}$, and q_i ($i = A, B$), as functions of position (z, R, r) and time (t) to be solved. c_B is related to c_A and C by the continuity condition, Eq (5.2). Time derivatives, dC/dt, $d\overline{\overline{q_i}}/dt$ and $d\overline{q_i}/dt$, are related to some other variables through Eqs (5.14) and the boundary condition, Eqs (5.5) and (5.7), respectively. To solve the other six variables, besides the initial conditions given to c_A, c_{pi} and q_i, proper boundary conditions must be assigned to $c_A(z)$, $c_{pi}(R)$, $q_i(r)$, and $v(z)$ based on the characteristics of the PSA operations. It is not necessary to give initial conditions to fluid phase velocity since no derivative of v with respect to t is involved in the model.

5.1.3 Boundary Conditions

For Eq (5.1), standard Danckwert's boundary conditions for component A are:

$$D_L \left. \frac{\partial c_A}{\partial z} \right|_{z=0} = -v|_{z=0} \left(c_A|_{z=0^-} - c_A|_{z=0^+} \right) \tag{5.1a}$$

$$\left. \frac{\partial c_A}{\partial z} \right|_{z=L} = 0 \tag{5.1b}$$

For Eq (5.4), the velocity boundary conditions are given based on the flow features of different operations. In the pressurization and blowdown steps, the product end of the column is closed:

$$v|_{z=L} = 0 \tag{5.4a}$$

In high pressurization adsorption step, the feed velocity is given as an operating parameter:

$$v\big|_{z=0} = v_0 \tag{5.4b}$$

For Eqs (5.6) and (5.8), the second parts of Eqs (5.5) and (5.7) provide the surface boundary conditions and symmetric boundary conditions apply at the center:

$$\frac{3}{R_P} k_f \left(c_i - c_{pi}\big|_{R=R_P} \right) = \frac{3}{R_P} \varepsilon_P D_p \frac{\partial c_{pi}}{\partial R}\bigg|_{R=R_p} \tag{5.5a}$$

$$\frac{\partial c_{pi}}{\partial R}\bigg|_{R=0} = 0 \tag{5.5b}$$

$$\frac{3}{r_c} k_{bi} \left(q_i^* - q_i\big|_{r=r_c} \right) = \frac{3}{r_c} D_{ci} \frac{\partial q_i}{\partial r}\bigg|_{r=r_c} \tag{5.8a}$$

$$\frac{\partial q_i}{\partial r}\bigg|_{r=0} = 0 \tag{5.8b}$$

5.1.4 Model Parameters

For a binary system, a total of nine parameters, D_L, k_f, D_p, q_i^*, k_{bi} and D_{ci}/r_c^2 (i =A, B) are involved in the calculation of the PSA simulation study. Estimations of some of these parameters were discussed in Chapters 2 and 3. They are repeated here for easy reference.

D_p is correlated to molecular diffusivity, D_M, by $D_p = D_M/3$, where 3 is the assumed tortuosity factor in the absence of any better data for CMS adsorbents.

D_L is estimated by the following equation (Ruthven, 1984a):

$$D_L = 0.7 D_M + 0.5 v d_p \tag{5.15}$$

where d_p is the diameter of adsorbent particle.

k_f is calculated from the following correlation:

$$Sh = 2.0 + 1.1 Sc^{1/3} Re^{0.6} \tag{5.16}$$

where, $Sh = \dfrac{k_f d_p}{D_M}$; $\quad Sc = \dfrac{\mu}{D_M \rho_g}$; $\quad Re = \dfrac{\rho_g v \varepsilon d_p}{\mu}$.

Following Langmuir isotherm, q_i^* is given by:

$$\frac{q_i^*}{q_s} = \theta_i = \frac{b_i c_{pi}}{1 + \sum\limits_i b_i c_{pi}} \tag{5.17}$$

Micropore transport parameters are concentration dependent and are given by the following equations:

$$D_{cA} = \frac{(D_{c0})_A}{1 - \theta_A - \theta_B} \left[(1 - \theta_B)(q_A^* - q_A) + \theta_A \frac{\partial q_B / \partial r}{\partial q_A / \partial r} \right] \tag{5.18}$$

$$k_{bA} = \frac{(k_{b0})_A}{1 - \theta_A - \theta_B} \left[(1 - \theta_B)(q_A^* - q_A) + \theta_A \frac{\partial q_B / \partial r}{\partial q_A / \partial r} \right] \tag{5.19}$$

and
$$(D_{c0})_i = (D_{c0}^*)_i \left(1 + \sum_i \beta_{pi} \frac{\theta_i}{1 - \sum\limits_j \theta_j} \right) \tag{5.20}$$

$$(k_{b0})_i = (k_{b0}^*)_i \left(1 + \sum_i \beta_{bi} \frac{\theta_i}{1 - \sum\limits_j \theta_j} \right) \tag{5.21}$$

The total concentration in the gas phase is correlated to the column pressure by the ideal gas law:

$$C = \frac{P}{R_g T} \tag{5.22}$$

5.1.5 Numerical Method

All the variables and parameters, except pressure, were made dimensionless. The above set of partial differential equations were then converted to 1st order ordinary differential equations of dimensionless time by discretizing all the spatial variables (dimensionless forms of z, R and r) using Orthogonal Collocation Scheme with 9 internal points along the bed and 6 internal points along the radius. Given initial bed conditions, normally in equilibrium with the feed mixture at either the high or the low operating pressure, the system of ODEs were solved by FORSIM integration package developed in FORTRAN codes (Farooq et al., 1993). Details about the numerical method have been placed in the appendix.

5.2 Comparison of Model Prediction with Experiments

In this part, the effectiveness of the PSA model in predicting the experimental results obtained from the laboratory scale experimental unit is investigated. For this purpose, numerical simulations were conducted for the experimental conditions given in Table 4.4.

5.2.1 Flow Rate vs. Column Pressure

As mentioned in Section 5.1.2.3, either a given pressure history or flow rate as a function of column pressure is used to calculate the total concentration in fluid phase. In this part of the study, since low operation pressure (P_L) was not fixed while the column pressure and flow rate data were continuously measured in the PSA experiments, flow rate equations were first used for the validation of PSA model.

Figures 5.1 and 5.2 show the plots of experimentally measured flow rate vs. column pressure during the blowdown and pressurization steps, respectively. The column pressure in these two figures was recorded by the pressure transducer, PT1, at

the top of the column. Clearly, the plots for all the five runs converge to a single curve very well, which is expected for constant valve/line resistance.
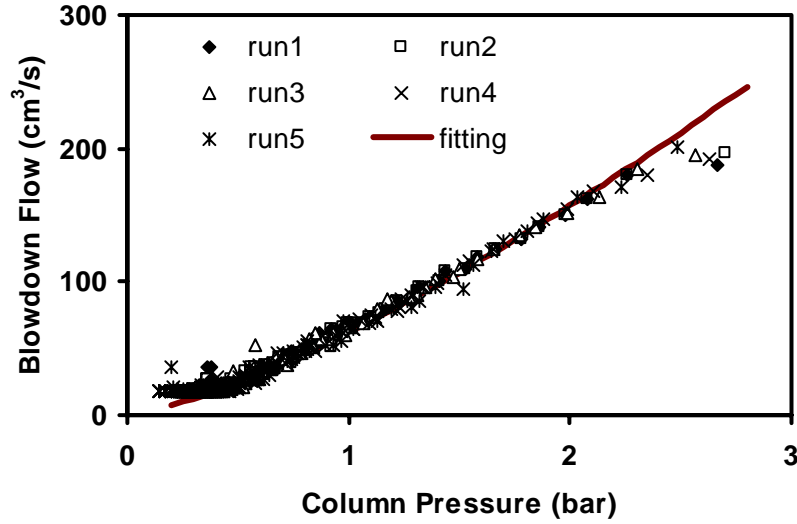

Figure 5.1 Fit of Eq (5.23) to experimental blowdown flow vs. column pressure.
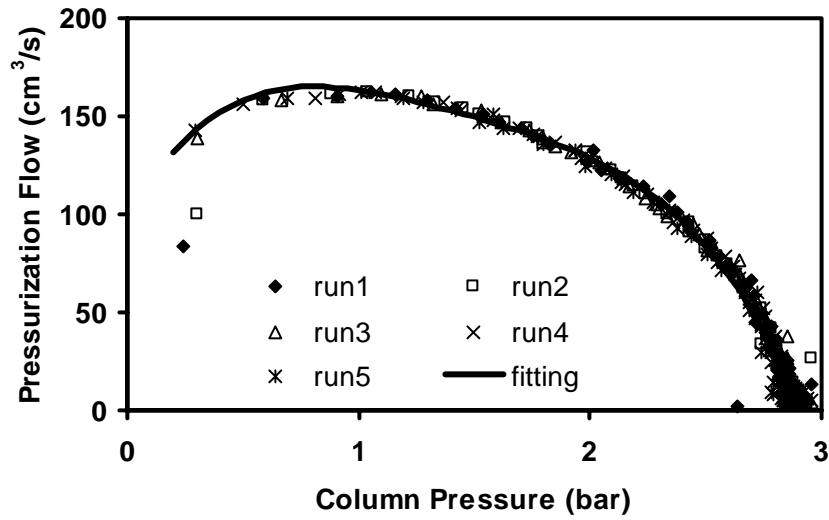

Figure 5.2 Fit of Eq (5.24) to experimental pressurization flow vs. column pressure.

The following power equation was used to express flow rate as a function of pressure for blowdown step:

$$F_{BD} = -v|_{z=0} P x_{area} \varepsilon_b = c_1 (P - P_V)^{c_2} \tag{5.23}$$

where F_{BD} is the blowdown flow rate, P is column pressure, P_V is the down stream pressure, which was controlled by a vacuum pump in the experiment and was very close to zero, c_1 and c_2 are constants. The value of c_1 and c_2 were extracted by fitting the experimental data using a spread sheet in Microsoft Excel (XP Professional). The fit of Eq (5.23) is also shown in Figure 5.1.

A power equation similar to Eq (5.23) cannot describe the pressurization flow rate vs. column pressure data very well since the curves in Figure 5.2 are too convex upwards and seem to have a maximum. A 4th order polynomial equation was used instead:

$$F_{PR} = v\big|_{z=0} Px_{area}\varepsilon_b = \sum_{i=0}^{4} d_i P^i \tag{5.24}$$

The five constants, d_i (i from 0 to 4), were obtained by fitting the above equation to the experimental data. The fit of Eq (5.24) to the experimental data is shown in Figure 5.2, which appears to be very good.

5.2.2 Integration of the Adsorption Term

The calculation of adsorption term in Eq (5.14) involves the integration of the adsorbed phase accumulation terms along the length of the column. In this study, linear approximation between two neighboring collocation points (a total of 11 points) was used.

In this study, the empirical equations relating $v\big|_{z=0}$ to P were used to calculate column pressure in the pressurization and blowdown steps from Eq (5.14). The obtained P vs. t was then used to calculate $v\big|_{z=0}$. Thus the agreement between the known v_0 and the calculated value by the later method was used to verify the accuracy

of the trapezoidal integration along the length of the column using 11 collocation points. Simulation results showed that the difference between the two values was normally less than 0.1%, which confirmed that the linear approximation did not introduce any significant error.

5.2.3 Prediction of Pressure Profiles during Pressurization and Blowdown Steps

The introduction of the flow rate equations allowed solving the column pressure as a function of time for the variable pressure steps. Using the flow rate equations and fitted constants obtained in Section 5.2.1, PSA simulations were carried out. The predicted pressure profiles are compared with experimental results in Figure 5.3. The agreement validates the reliability of the equilibrium and kinetic models used in PSA simulation.
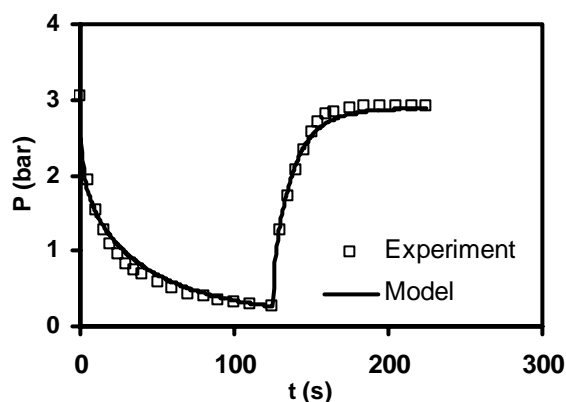
Figure 5.3 Comparison of model predicted pressure profiles and experimental results during blowdown and pressurization steps for run 2 listed in Table 4.4.

5.2.4 Purity and Recovery of Argon Product

Product purity and recovery at steady state are the main indicators of the process performance of a PSA cycle. As defined in Section 4.6, the product purity is the average argon concentration in the product collected during the high pressure adsorption step at cyclic steady state. The product recovery is the ratio of pure argon

94

collected in the product to the total amount of pure argon going into the bed during the pressurization and high pressure feed steps. The experimental and theoretical purity and recovery of argon product are compared for different blowdown and adsorption times in Figures 5.4 and 5.5, respectively. While the recovery prediction is good, it is clear that model underestimates the product purity. The possible reason is discussed in the following section by investigating the gas flow profiles during each step.

5.2.5 Gas Flow Profiles

In order to throw some useful insight into the reasons for significant quantitative discrepancy between experimental and predicted argon product purity, the experimentally measured blowdown, pressurization and product flow profiles at cyclic steady state for a representative run are compared with the theoretical predictions in Figure 5.6.

Generally speaking, the experimental flow rate profiles during pressurization and blowdown show good agreement with the model predictions, which is expected since the flow rate equations were obtained by optimizing their fits to the experimental flow vs. column pressure. However, the experimental product flow rate profile shows significant deviation from the model prediction. The cause of this deviation is investigated in the following section.
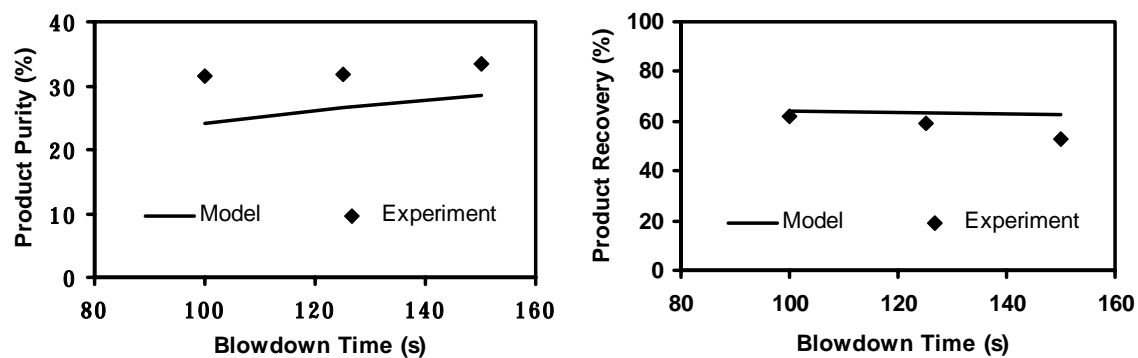
Figure 5.4 Effects of blowdown time on argon product purity and recovery.
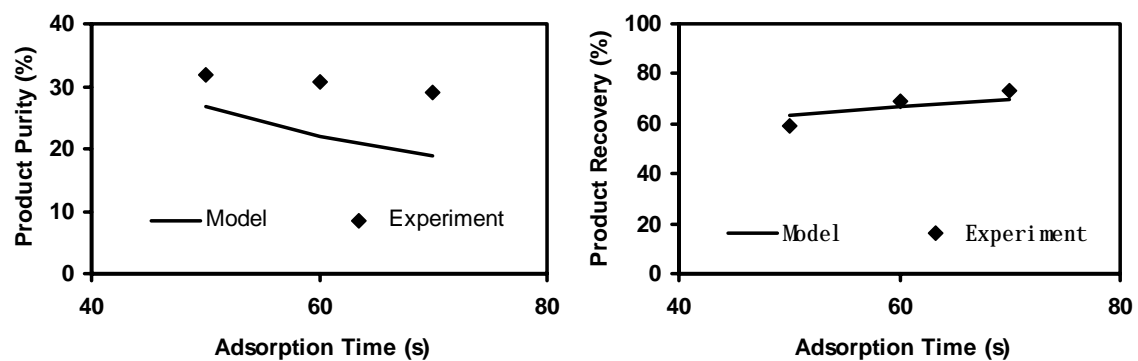

Figure 5.5 Effects of high pressure adsorption time on argon product purity and recovery.
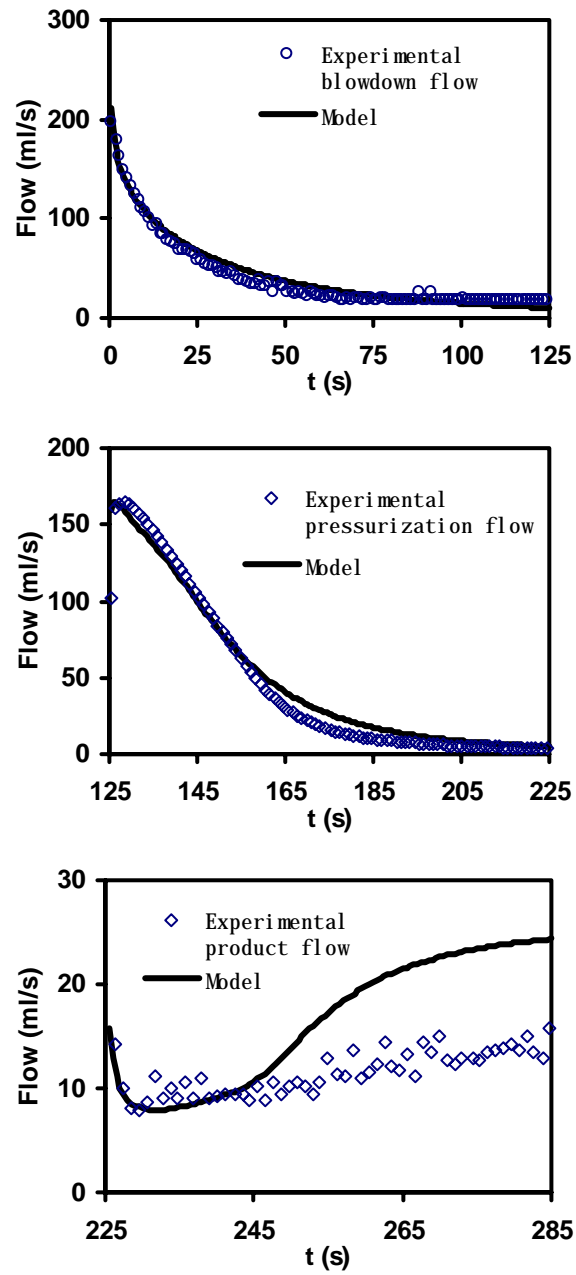
Figure 5.6 Comparison of the predicted flow rate profiles and experimental results. The points are experimental data of Run 2 in Table 4.4.

5.2.6 Effect of Changing Pressure in the High Pressure Adsorption Step

Figure 5.7 shows the experimental pressure profiles during the high pressure adsorption step using a magnified scale. It is important to note that in the PSA experiments, the column pressure was not constant as assumed in the PSA model (assumption 10 in Section 5.1.1), which may be due to the control delay limitation of the back pressure regulator. As shown in Figure 5.7, at the very beginning of the adsorption step, there was a sharp pressure drop from (~3 to ~ 2.8 bar), then the pressure slowly increased back to the level at the start of the adsorption step (~3 bar).
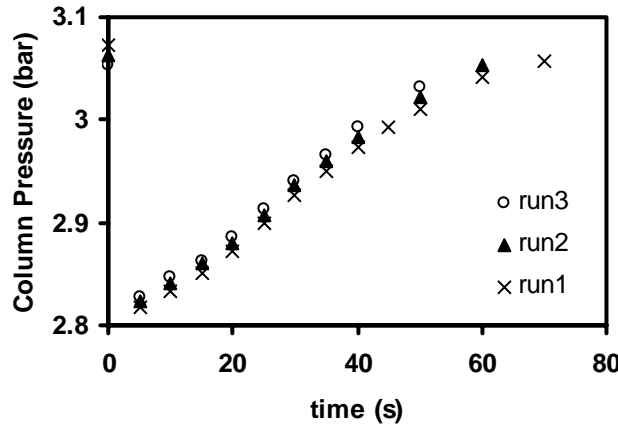
Figure 5.7 Pressure change in the high pressure adsorption step.

It is also seen from Figure 5.7 that the pressure rise in the column during the adsorption step was approximately linear. The following equation was used to describe the pressure change to capture this effect in the simulation.

$$\frac{dP}{dt} = \begin{cases} -a_1 & t \le 5s \\ a_2 & t > 5s \end{cases} \qquad (5.25)$$

where t is time in the adsorption step, a_1 and a_2 are positive constants determined from the experimental observation.

The above equation was used to replace the constant pressure assumption in the original PSA model ($P = P_H = \text{constant or } \dfrac{dP}{dt} = 0$). PSA simulations were then carried out to investigate the effect of the changing pressure during adsorption step. The product purities, recoveries and flow rates calculated by the original model and the modified model accounting for the pressure change during the adsorption step are compared with the experimental data in Figures 5.8-5.10. It is clear that, after accounting for the pressure change, the agreement between model prediction and experimental results for product purity and flow rate has improved significantly.

Simulation results from the two models are summarized in Tables 5.1 and 5.2. While the product flow calculated by the modified model is lower than that by the original model, the amounts of argon in the product stream calculated by the two models are quit close, since concentration of argon in the later is higher. As a result, argon recovery prediction is not significantly affected by the pressure change during the adsorption step.

It should be noted that the pressure change during the adsorption step improves the product purity. Thus, the assumption of constant pressure during the high pressure production step gives conservative prediction of the PSA performance, which is acceptable for the parametric study presented in the next section.
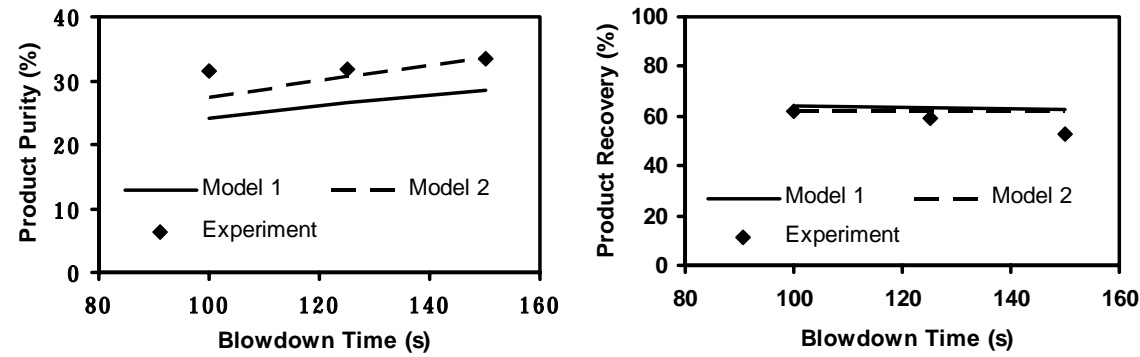
Figure 5.8 Effects of pressure change during the adsorption step on argon product purity and recovery for varying blowdown time. Model 1 assumes constant pressure and Model 2 accounts for the pressure change.
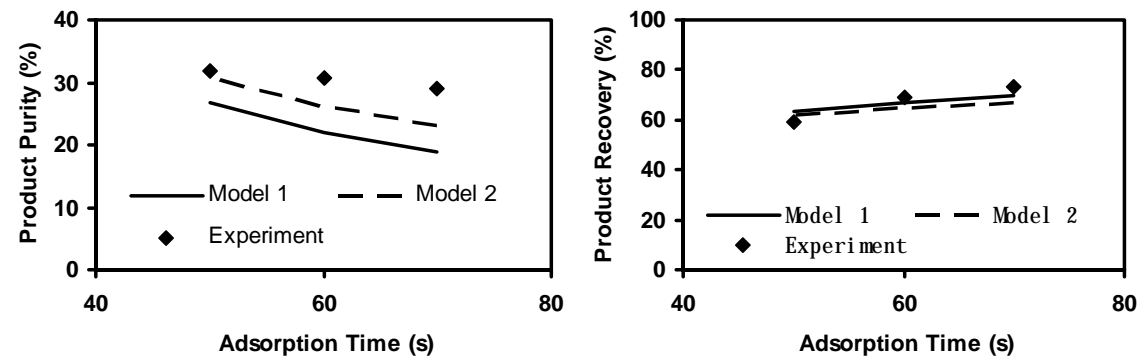

Figure 5.9 Effects of pressure change during the adsorption step on argon product purity and recovery for varying adsorption time. Model 1 assumes constant pressure and Model 2 accounts for the pressure change.
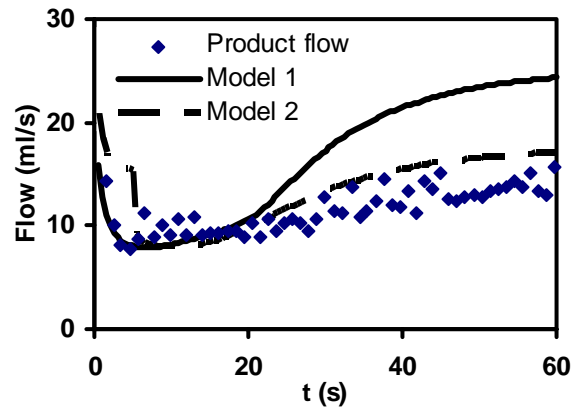
Figure 5.10 Effect of pressure change during the adsorption step on product flow rate. Model 1 assumes constant pressure and model 2 accounts for the pressure change during the high pressure adsorption step.

Table 5.1 Summary of the simulation results assuming constant pressure during the adsorption step.

Run No.	BD (s)	HP (s)	Gas going out of the bed during BD (cm³)	Gas going into the bed during PR (cm³)	Gas going into the bed during HP (cm³)	Gas going out of the bed during HP (cm³)	Ar going out of the bed during HP (cm³)	Mass balance error (%)	Argon product		
									Purity (%)	Recovery (%)	Productivity (cc/hr/cc ads.)
1	125	70	5491.6	4977.3	1750	1236.4	234.0	-0.37	18.9	69.6	9.7
2	125	60	5491.0	4968.8	1500	984.6	216.4	-0.29	22.0	66.9	9.3
3	125	50	5478.9	4961.1	1250	739.5	197.1	-0.30	26.7	63.5	8.8
4	150	50	5695.3	5135.0	1250	701.1	200.5	-0.35	28.6	62.8	8.2
5	100	50	5170.6	4702.2	1250	786.4	190.6	-0.21	24.2	64.0	9.3

BD: blowdown step; HP: high pressure production step. Pressurization step: 100 s; High operating pressure: ~3 atm; Feed flow rate: 25 cm³/. The gas volumes are based on 1 atm pressure. The experimental results are summarized in Table 4.4.

Table 5.2 Summary of the simulation results accounting for the pressure change during the adsorption step.

Run No.	BD (s)	HP (s)	Gas going out of the bed during BD (cm³)	Gas going into the bed during PR (cm³)	Gas going into the bed during HP (cm³)	Gas going out of the bed during HP (cm³)	Ar going out of the bed during HP (cm³)	Mass balance error (%)	Argon product		
									Purity (%)	Recovery (%)	Productivity (cc/hr/cc ads.)
1	125	70	5740.8	4963.6	1750	977.1	224.5	-0.34	23.0	66.9	9.3
2	125	60	5665.3	4960.7	1500	800.2	209.0	-0.35	26.1	64.7	9.0
3	125	50	5587.1	4956.1	1250	624.3	191.3	-0.35	30.6	61.6	8.5
4	150	50	5806.6	5134.3	1250	587.1	197.4	-0.45	33.6	61.8	8.0
5	100	50	5278.4	4695.9	1250	670.7	183.9	-0.24	27.4	61.9	9.0

For other details, see the footnotes in Table 5.1.

5.3 Parameter Effects on the PSA Performance of the Single-bed, 3-Step Cycle

With the confidence that the PSA model captures the main features of experimental phenomena, the effects of some operating parameters, such as duration of each step, L/v_0 ratio, and level of desorption pressure on the purity and recovery of argon product by the single-bed, 3-step cycle were investigated over a wide range of the parameters using the simulation model. In an industrial setting, the most likely source of the O_2-Ar feed mixture is equilibrium controlled PSA air separation unit. In order to simulate realistic industrial conditions, the high operating pressure in this study was chosen to be either 1 atm or 3 atm, the pressures of O_2 product in the two main industrial PSA air separation methods, VSA process and Lindox process, respectively (Ruthven et al., 1994a).

Since the restriction of pressurization and blowdown flow rates can be easily improved by using larger pipelines and valves with less resistance, exponential pressure profiles during pressurization and blowdown steps with constants $a_1 = a_2 = 0.6$ were used in this part of study for a more general search. The column pressure was assumed to be constant during the high pressure production step, which is a conservative approach as discussed in the previous section. Any other assumption is likely to introduce undesirable uncertainty. The simulation results are summarized in Table 5.3.

It may be seen from Table 5.3 that the purity of Ar in the high pressure PSA is limited to 50%. The purity and recovery can be improved further in subatmospheric cycles with a consequent loss of productivity. Figure 5.11 shows argon purity vs. recovery plot under different operating conditions for the subatmospheric 3-step cycle.

Clearly, PSA performance is significantly affected by the operating parameters and there is always a trade-off between argon purity and recovery.

When the feed velocity increases, more argon is collected during the given period of high pressure adsorption step and the recovery is improved. However, more oxygen travels to the product end and contaminates the product, thus diminishing argon purity.

With a lower desorption pressure, the bed is better regenerated and has higher capacity for oxygen in the following pressurization and high pressure adsorption steps. Hence, the purity of argon product is improved. This also increases argon adsorption, resulting in a lower recovery.

The longer blowdown time and shorter pressurization time have similar effects, which are opposite to the effects of lower desorption pressure. The improvement of recovery and loss of purity with longer duration of high pressure adsorption step is self-explanatory and easily understood. In a traditional Skarstrom cycle, the pressurization and blowdown times are equal and the net effect of changing both is likely to be negligible. Similar is the overall effect of high adsorption and self-purge steps. This may be seen from the simulation results of high pressure cycles listed in Table 5.3, which have the blowdown duration equal to pressurization plus high pressure adsorption and are in fact Skarstrom cycles without external purge (see Figure 4.2). For this reason, the single-bed, 3-step cycle, which has the flexibility of varying each step independently, is superior to traditional Skarstrom cycle for kinetically controlled PSA processes.

Figure 5.11 also shows that, among the operating parameters investigated, a low desorption pressure is the most efficient way to improve argon purity since the corresponding loss of recovery is relatively less compared to other cases.

Table 5.3 Simulation results of the single-bed, 3-step cycle for argon product.

Run No.	Operation Conditions						Argon product		
	P_H (atm)	P_L (atm)	PR (s)	HP (s)	BD (s)	L/v_0 (s)	Purity (%)	Recovery (%)	Productivity (cc/hr/cc ads.)
1	3.0	1.0	30	30	60	20	43.1	44.6	8.55
2			45	30	75	20	37.1	54.6	9.00
3			45	45	90	20	25.6	67.6	9.72
4			45	30	75	30	50.1	38.7	5.95
5			60	30	90	30	48.1	43.5	5.82
6			60	45	105	30	37.7	56.6	6.91
7	1.0	0.2	*45*	75	120	30	70.8	41.3	2.14
8			*60*	75	135	30	66.1	49.8	2.39
9			*75*	75	150	30	59.6	53.5	2.38
10			*90*	75	165	30	51.9	54.7	2.26
11			75	*45*	120	30	71.5	34.8	1.78
12			75	*60*	135	30	67.5	45.6	2.16
13			75	*90*	165	30	45.9	59.4	2.49
14			75	75	150	*10*	12.6	75.7	4.53
15			75	75	150	*20*	29.5	65.8	3.19
16			75	75	150	*40*	71.0	39.7	1.69
17		*0.05*	75	75	150	30	79.6	43.1	2.17
18		*0.1*	75	75	150	30	73.3	48.1	2.36
19		*0.3*	75	75	150	30	42.6	57.6	2.29
20		0.1	75	75	*90*	30	69.5	52.6	2.38
21			75	75	*120*	30	72.8	50.7	2.34
22			75	75	*180*	30	73.6	45.6	2.33

P_H: the highest operating pressure; P_L: the lowest operating pressure; PR: pressurization step; HP: high pressure adsorption step; BD: blowdown step; L/v_0: ratio of column length to feed velocity during the high pressure adsorption step.
Feed composition: 95% O_2 and 5% Ar on molar basis. Temperature: 293 K. Results presented are for the 25th cycle. For column dimensions, see Table 4.1.
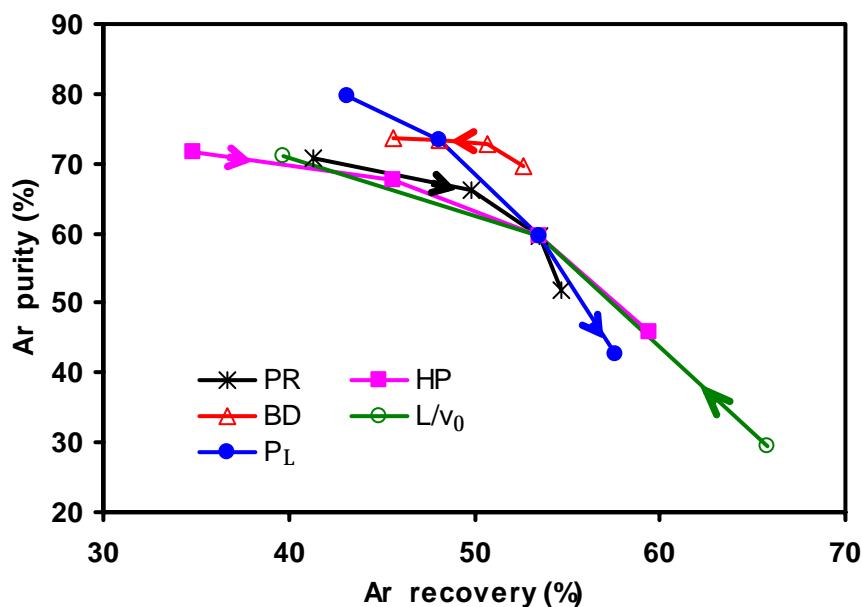
Figure 5.11 Plot of argon purity vs. recovery showing the effects of different operation conditions on PSA performance of the single-bed, 3-step cycle. The arrows indicate increasing direction of the operating parameters.

PR: pressurization step (45-90 s); HP: high pressure adsorption step (45-90 s); BD: blowdown step (90-180 s); L/v_0: ratio of column length to feed velocity during the high pressure adsorption step (10-40 s); PL: the lowest operating pressure (0.05-3 atm). The highest operating pressure: 1.0 atm. For column dimensions, see Table 4.1.

5.4 Simulation study for the Feasibility of Some Other cycles

In this section, the feasibility of two other cycles for O_2-Ar separation is investigated by simulation. The assumption of exponential pressure profiles with constants $a_1 = a_2 = 0.6$ is retained in this part of study and the pressures during the production and purge steps are assumed to remain constant.

5.4.1 2-bed, 5-Step Cycle for Ar Product
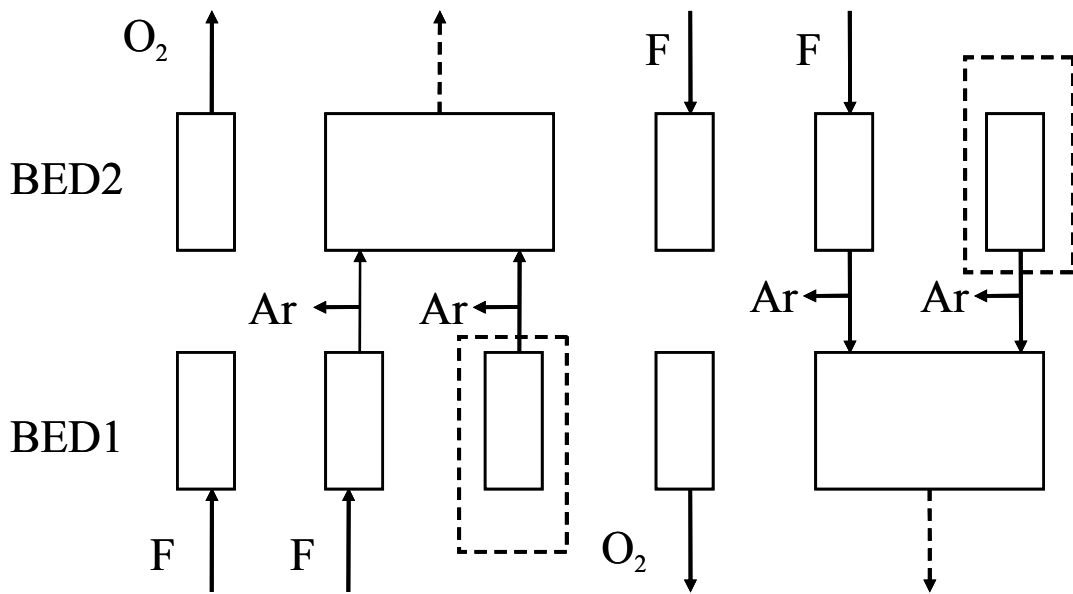
Figure 5.12 Schematic diagram of the 2-bed, 5-step cycle for argon product. The boxed step is co-current blowdown to an intermediate pressure. The dash arrow means gas discarded. F is feed mixture.

A 2-bed, 5-step cycle was suggested by Rega and Yang (2000) for kinetically controlled oxygen and argon separation using BF CMS. A schematic diagram of this cycle is shown in Figure 5.12. The operations of bed 1 (shown in the figure from left to right) are pressurization, high pressure adsorption, co-current blowdown to an intermediate pressure (P_{cd}), counter-current blowdown and counter-current external purge. The special feature of this cycle is the combination of co-current blowdown step to improve Ar recovery and counter-current external purge step to improve the purity.

However, any enhancement of recovery or purity sacrifices the other. In order to compare the effectiveness of the 2-bed, 5-step cycle of Rege and Yang (2000) with the single-bed, 3-step cycle discussed in the previous section, simulations were carried out on the former configuration using the same column size, operating conditions and adsorption equilibrium and kinetic parameters of this study. The simulation results are shown in Table 5.4.

Table 5.4 Simulation results of the 2-bed, 5-step cycle for argon product.

Run No.	Operating conditions					Argon product		
	PR/BD (s)	HP (s)	CB (s)	PGV (cm/s)	P$_{CB}$ (atm)	Purity (%)	Recovery (%)	Productivity (cc/hr/cc ads.)
1	75	*60*	5	0	0.85	40.5	62.7	2.86
2	75	*75*	5	0	0.85	34.8	64.8	2.77
3	75	*90*	5	0	0.85	29.2	69.0	2.80
4	*45*	60	5	0	0.85	45.4	61.4	3.04
5	*60*	60	5	0	0.85	47.9	62.9	3.09
6	75	60	*10*	0	0.85	34.2	64.5	2.84
7	75	60	*15*	0	0.85	31.4	66.3	2.83
8	75	60	5	0	*0.70*	16.5	72.1	3.07
9	75	60	5	0	*0.80*	31.9	63.1	2.88
10	75	60	5	0	*0.90*	52.8	59.4	2.70
11	75	60	5	0	*0.95*	64.0	53.6	2.44
12	75	60	5	1.33	0.85	44.8	56.6	2.59
13	75	60	5	2.67	0.85	47.4	49.5	2.30

PR/BD: the pressurization and counter-current blowdown steps have the same duration (45-75 s); HP: high pressure adsorption step (60-90 s); CB: co-current blowdown step (5-15 s); PGV: purge velocity (0-2.67 cm/s); P$_{CB}$: intermediate pressure during the co-current blowdown step (0.70-0.95 atm). P$_H$: 1atm; P$_L$: 0.2 atm. L/v_0: 30 s.
Feed composition: 95% O_2 and 5% Ar on molar basis. Temperature: 293 K. Results presented are for the 25th cycle. For column dimensions, see Table 4.1.

Compared with the simulation results of the single-bed, 3-step cycle listed in Table 5.3, the 2-bed 5-step cycle does not seem to show any advantage in term of argon product purity and recovery. The additional complexity of the cycle is also not desirable without any significant compensating advantage.

5.4.2 Single-bed, 5-Step Cycle for O$_2$ Product
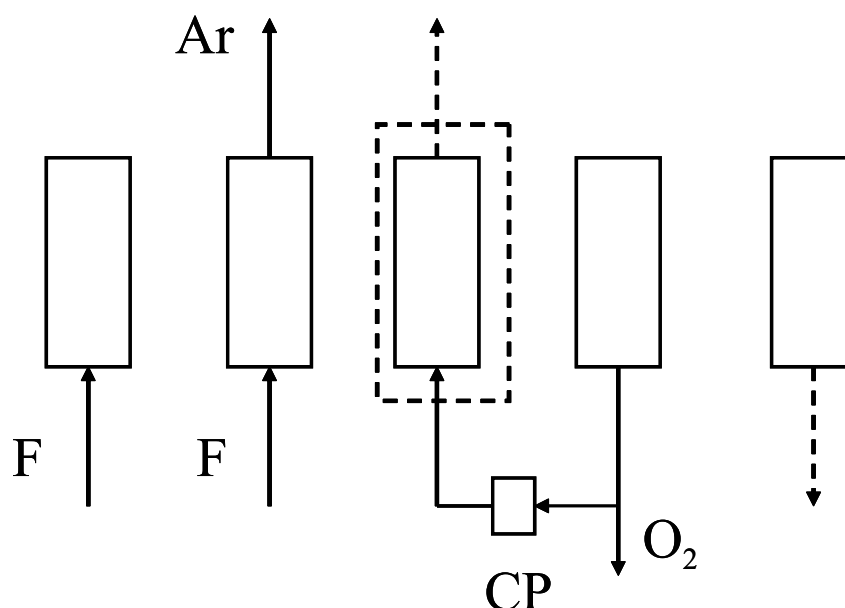
Figure 5.13 Schematic diagram of the single-bed, 5-step cycle for oxygen product. The boxed step is co-current purge at high pressure. The dash arrow means gas discarded. F is feed mixture. CP is a compressor.

A schematic diagram of a single-bed, 5-step cycle for oxygen product is shown in Figure 5.13. The operations, from left to right, are pressurization, high pressure adsorption, co-current purge, counter-current blowdown to collect oxygen product and co-current blowdown to regenerate the bed. The co-current purge step is a signature of cycles for the more strongly adsorbed species and was first introduced in a study of hydrogen-methane separation (Cen et al., 1986). Since the low pressure product is used to purge the high pressure column, a storage tank and a compressor must be introduced in this cycle. Unlike the oxygen cycle suggested by Rege and Yang (2000), only the first part of the blowdown gas is collected as product in this cycle to improve the oxygen purity because the later part of blowdown gas is enriched with argon, which is the slower desorbing component.

Table 5.5 Simulation results of the single-bed, 5-step cycle for oxygen product.

Run No.	Operating conditions					Oxygen product		
	PG (s)	PV (cm/s)	v_0 (cm/s)	P_L (atm)	TRC[4] (s)	Purity (%)	Recovery (%)	Productivity (cc/hr/cc ads.)
1	20	*1*	2	0.1	75	98.34	88.9	81.64
2	20	*2*	2	0.1	75	98.50	86.3	79.34
3	20	*3*	2	0.1	75	98.63	83.6	76.90
4	20	*4*	2	0.1	75	98.72	80.8	73.34
5	20	*6*	2	0.1	75	98.83	74.7	68.80
6	*10*	2	2	0.1	75	98.38	88.5	84.14
7	*30*	2	2	0.1	75	98.67	83.2	74.16
8	*40*	2	2	0.1	75	98.79	80.6	69.78
9	*60*	2	2	0.1	75	98.96	75.0	61.37
10	20	2	2	0.1	*18.75*	98.85	58.1	53.50
11	20	2	2	0.1	*37.5*	98.79	76.8	70.77
12	20	2	2	0.1	*100*	98.33	88.1	81.18
13	20	2	*1*	0.1	75	98.28	95.7	79.45
14	20	2	*3*	0.1	75	98.66	77.0	79.55
15	20	2	*4*	0.1	75	98.72	69.5	79.62
16	20	2	2	*0.2*	75	98.59	82.2	69.68
17	20	2	2	*0.3*	75	98.60	77.8	59.69
18	20	2	2	*0.4*	75	98.55	72.4	49.67
19	20	2	2	*0.5*	75	98.45	65.8	39.8
20	40	3	3	0.2	75	99.08	61.6	55.5

PG: purge step; PV: purge velocity; v_0: feed velocity during adsorption step; P_L: the lowest operating pressure; TRC: duration of oxygen product collection.
Pressurization step: 75 s. High pressure adsorption step: 75 s, total duration of blowdown: 150 s, the highest operating pressure: 1.0 atm. Feed composition: 95% O_2 and 5% Ar on molar basis. Temperature: 293 K. Results presented are for the 25th cycle. For column dimensions, see Table 4.1.

The simulation results of the single-bed, 5-step cycle for the adsorbent used in this study are summarized in Table 5.5 and the effects of some operating parameters on oxygen purity and recovery are shown in Figure 5.14. It may be seen from the effect of the product collection time (TRC curve in the figure) that the oxygen purity can be improved without significant loss of recovery by discarding a proper proportion of the later part of the blowdown gas. The most efficient way to increase O_2 purity is, as expected, to increase the purge time and velocity with a relatively less loss of recovery.
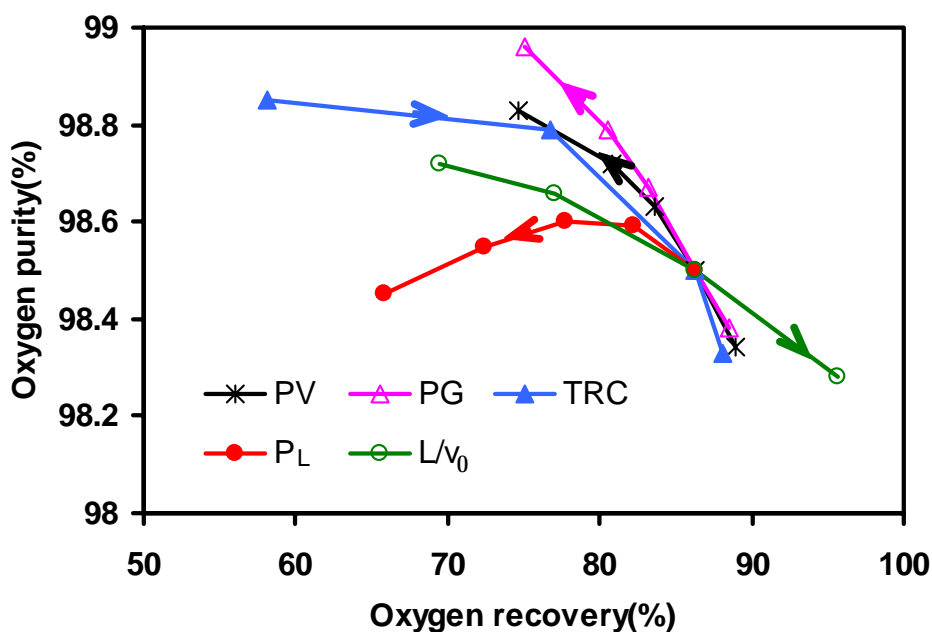
Figure 5.14 Plot of oxygen purity vs. recovery showing the effects of different operation conditions on PSA performance of the single-bed, 5-step cycle. The arrows indicate increasing direction of the operating parameters.
PV: purge velocity (1-6 cm/s); PG: purge step (10-60 s); TRC: duration of oxygen product collection (18.75-100 s); P_L: the lowest operating pressure (0.1-0.5 atm); L/v_0: ratio of column length to feed velocity during the high pressure adsorption step (10-40 s). The highest operation pressure: 1.0 atm. Pressurization step: 75 s. High pressure adsorption step: 75 s. Total duration of blowdown: 150 s. For column dimensions, see Table 4.1.

Another interesting finding is that the effect of low operating pressure on purity has a maximum value located between 0.2 and 0.3 bar, which is an exception to the normally observed trade-off between purity and recovery of the raffinate product (see Section 5.3). The poor PSA performance at low pressure ratio is easily understood – unless sufficiently regenerated, the bed has little capacity for the desired separation. On the other hand, prolonged blowdown at very low pressure results in argon desorption, thus contaminating the O_2 product. In fact, since the recovery of O_2 is generally very high (see Table 5.5), the purity is mainly determined by the recovery of Ar in

adsorption step, which can be seen from the following component mass balance equations at steady state. Here, step 4 and step 5 are combined without discarding any gas for simplicity.

$$\text{Re} \cos ery_{Ar} + \lambda \times \text{Re} \cos ery_{O_2} \times \frac{\left(1 - Purity_{O_2}\right)}{Purity_{O_2}} = 1 \qquad \text{(For argon)} \qquad (5.26)$$

$$\text{Re} \cos ery_{O_2} + \frac{1}{\lambda} \times \text{Re} \cos ery_{Ar} \times \frac{\left(1 - Purity_{Ar}\right)}{Purity_{Ar}} = 1 \qquad \text{(For oxygen)} \qquad (5.27)$$

where $\lambda = \dfrac{1 - x_{feed}}{x_{feed}}$ and x_{feed} is Ar concentration in the feed mixture.

When $\text{Re} \cos ery_{O_2}$ is very high (≈ 1), Eq (5.26), reduces to:

$$Purity_{O_2} \approx \frac{\lambda}{1 + \lambda - \text{Re} \cos ery_{Ar}} \qquad (5.28)$$

As a result, the operating conditions favoring the recovery of Ar can be used to improve O_2 purity.

Chapter 6   Conclusions and Recommendations

6.1 Conclusions

This project was aimed at choosing a suitable adsorbent and developing feasible cycles for the separation of oxygen-argon mixture. The study mainly involved five tasks, namely, (i) screening of different adsorbents, (ii) detailed equilibrium and kinetic measurements on the selected adsorbent, (iii) PSA experiments using a single-bed, 3-step cycle to validate the PSA model, (iv) PSA simulations to optimize the operating conditions of the single-bed, 3-step cycle for argon production, and (v) investigation of the feasibility of some other potential cycles. The major conclusions are summarized here.

1. Single component equilibrium and kinetics of argon in four adsorbent, BF, Takeda I, Takeda II CMS samples and RS-10 zeolite, were measured in the linear range using the volumetric method. The experimental uptake curves were plotted against square root of time to distinguish possible transport mechanisms in micropores. The transport of argon in micropores of the three CMS samples can be described by a dual resistance model, which accounts for both barrier resistance confined at the mouth of micropores and pore resistance distributed inside micropores. Both resistances in CMS samples are important in the linear range. The transport of argon in RS-10 zeolite can be described by the pore model, which is an extreme of the dual model when barrier resistance is negligible. The obtained equilibrium and kinetic parameters were validated by DCBT study and were then, together with the oxygen data obtained in another study, used to compare the kinetic selectivity of each adsorbent for oxygen-argon separation. Among the four adsorbents investigated, Takeda II CMS showed the highest kinetic selectivity.

2. The adsorption equilibrium and kinetics of argon in Takeda II CMS were detailed measured over a pressure range up to 6 bar. Isotherms of oxygen and argon measured at different temperatures were well represented by the Langmuir model with same saturation capacity for both components. The transport parameters of the dual resistance model were found to be strongly concentration dependent. This strong concentration dependence was accounted for following the proposal in another study conducted in this laboratory.

3. PSA experiments were conducted on a laboratory scale setup using a single-bed, 3-step cycle to concentrate argon from a feed mixture of 95% oxygen and 5% argon. An existing PSA model, developed earlier in this laboratory for kinetically controlled air separation, was modified to quantitatively predict the experimental behaviors of kinetically controlled oxygen-argon separation for argon production. Very high fraction of the faster component and vacuum regeneration were the challenging experiences of the experimental study. The generally good agreement validated the reliability of the PSA model.

4. Systematic simulations were conducted using the PSA model validated by experiments to optimize the argon cycle and search for a suitable oxygen cycle. PSA performance is significantly affected by the cycle design and operating conditions. A single-bed, 3-step cycle and a 2-bed, 5-step cycle were suggested for the production of high purity argon and oxygen, respectively.

6.2 Recommendations

This study was taken up as a MEng project that had to be finished within one and half years. Some promising avenues that deserved for further exploration could not

be undertaken due to time limitation. Some recommendations for future study are made here.

1. The resistance of pipeline has proven to have a significant effect on PSA performance. Although this does not affect the validation of simulation results, it will be more convincing if experimental data around optimized region are available. Reconstructing the PSA rig with larger diameter tubes and valves is recommended.

2. The PSA model has two major assumptions: isothermal system and uniform pressure within the bed. The effects of adsorption and desorption heat were accounted for in some other studies conducted in this group. Although it was found in this study that the pressure drop along the column was negligible in the operating range, consideration of pressure drop will make the simulation more realistic with respect to industrial processes.

REFERENCES

Arvind, R., S. Farooq and D. M. Ruthven. Analysis of a Piston PSA process for Air Separation, *Chem. Eng. Sci.,* 57, pp. 419-433, 2002.

Bird, R. B., W. E. Stewart, E. N. Lightfoot. Transport phenomena, New York : J. Wiley, 2002.

Boniface, H. A. and D. M. Ruthven. Selectivity of some zeolites for adsorption of atmospheric gases, *Gas. Sep. Purif.* 7(3), 1993.

Brandani, S.. Analysis of the Piezometric Method for the study of Diffusion in Miocroporous Solids: Isothermal Case, *Adsorption*, 4, pp. 17-24, 1998.

Cen, P. L. and R. T. Yang. A New Pressure Swing Adsorption Cycle for Separating the Binary Mixture into Two High-Purity Products. *Separation Sci. Tech*., 21(9), pp. 845-856, 1986.

Chen, Y. D., R. T. Yang and P. Uawithya. Diffusion of Oxygen, Nitrogen and Mixtures in Carbon Molecular Sieves, *AIChE J.*, 40, pp. 577-585, 1994.

Chihara, K., M. Suzuki and K. Kawazone. Adsorption Rate on Molecular Sieving Carbon by Chromatography, *AIChE J.*, 24(2), pp.237-245, 1978.

Chihara, K. and M. Suzuki. Air Drying by Pressure Swing Adsorption, *J. Chem. Eng. Japan*, 16(4), pp. 293-299, 1983.

Crank, J. The Mathematics of Diffusion, Oxyford University Press, London, UK, 1956.

Farooq, S. and D. M. Ruthven and HA Boniface. Numerical Simulation of a Pressure Swing Adsorption Oxygen Unit, *Chem. Eng. Sci.,* 44, pp. 2809-2816, 1989.

Farooq, S. and D. M. Ruthven. A Comparison of Linear Driving Force and Pore Diffusion-Model for a Pressure Swing Adsorption Bulk Separation Process, *Chem. Eng. Sci.,* 45, pp. 107-115, 1990.

Farooq, S. and D. M. Ruthven. Numerical Simulation of a kinetically Controlled Pressure Swing Adsorption Bulk Separation Process Based on a Diffusion Model, *Chem. Eng. Sci.*, 46, (9), pp. 2213-2224, 1991

Farooq, S., M. N. Rathor and K. Hidajat. A Predictive Model for a Kinetically Controlled Pressure Swing Adsorption Separation Process, *Chem. Eng. Sci.,*48, (24), pp. 4129-4141, 1993.

Farooq, S. Sorption and Diffusion of Oxygen and Nitrogen in Molecular-Sieve RS-10. *Gas. Sep. Purif.* Vol. 9. No.3, pp. 205-212, 1995.

Farooq, S., Q. Huang and S. M. Sundaram. Diffusion of Oxygen and Nitrogen in CMS Micropores at High Coverage and its Impact on Kinetically Controlled PSA Separation. In AICHE Annual Meeting, Reno, Nevada, Nov. 2001.

Farooq, S., Q. Huang and IA Karimi. Identification of Transport Mechanism in Adsorbent Micropores from Column Dynamics, *Ind. Eng. Chem. Res*., 41, pp. 1098-1106, 2002.

Freitas, M.M.A., and J.L. Figueiredo. Preparation of Carbon Molecular Sieves for Gas Separations by Modification of Pore Sizes of Activated Carbons, *Fuel*, 80, 2000.

Fatehi, AI, KF. Loughlin and MM. Hassan. Separation OF Methane-Nitrogen Mixtures by Pressure Swing A adsorption Using a Carbon Molecular Sieve, *Gas. Sep. Purif.*, 9 (3): pp.199-204, 1995.

Glueckauf, E. and J. J. Coates. Theory of Chromatography. Part IV. The Influence of Incomplete Equilibrium on the Front Boundary of Chromatograms and on the Effectiveness of Separation. *J. Chem. Soc*. p1315, 1947.

Gupta, R. and S. Farooq. Numerical Simulation of a Kinetically Controlled Bulk PSA Separation Process Based on a Bidispersed Pore Diffusion Model. Proceedings of the 8th *APCChE Congress*, Vol. 3, pp. 1753-1756, August 16-19, Soul, Korea, 1999.

Gupta, R. Kinetically Controlled Separation by Pressure Swing Adsorption, Master Thesis, National University of Singapore, 2000.

Hayashi,S., H. Tsuchiya and K. Haruna. Process for Obtaining High Concentration Argon by Pressure Swing Adsorption, US patent 4,529,412, 1985.

Hayashi,S., M. Kawai and T. Kaneko. Dynamics of high purity oxygen PSA, *Gas. Sep. Purif*. Vol. 10. No.1, 1996.

Horie, K., M. Ohyagi, C. Napoli and K. Ishizaki. Gas separation by superconducting filter using meissner effect, *Scripta mater*, 44, 2001.

Huang, Q., S. M. Sundaram and S. Farooq. Dual resistance model for the transport of gases in carbon molecular sieve. Presented at the AIChE annual meeting, Reno, Nevada, Nov. 4 –9, 2001.

Huang, Q. Multicomponent Diffusion of Gases in the Micropores of Carbon Molecular Sieves, PhD thesis, National University of Singapore, 2002.

Huang, Q., S. M. Sundaram and S. Farooq. Revisiting Transports of Gases in Micropores of Carbon Molecular Sieves, *Langmuir*, 19, pp. 393-405, 2003a.

Huang, Q., S. Farooq and I. A. Karimi, Binary and Ternary Adsorption Kinetics of Gases in Carbon Molecular Sieves, *Langmuir*, 19, pp. 5722-5734, 2003b.

Kandybin, A. I., R. A. Anderson and D. L. Reichley. Separation of oxygen from argon/oxygen mixture, US Patent 5,470,378, 1995.

Kapoor, A and RT Yang. Kinetic Separation of Methane Carbon-Dioxide Mixture by Adsorption on Molecular Sieve Carbon, Chem. Eng. Sci. 44, pp. 1723-1733, 1989.

Kawazoe, K., M. Suzuki and K. Chihara. Chromatographic Study of Diffusion in Molecular Sieve Carbon, *J. Chem. Engg. Japan*, 7, pp. 151-157, 1974.

Kikkinides, E. S. and R. T. Yang. Simultaneous SO_2/NO_x Removal and SO_2 Recovery From Flue Gas by PSA, *IEC Res*., 30, pp. 1981-1989, 1991.

Kovak, K.W., R. Agrawal and J. C. Peterson. Method for Purifying Argon through Cryogenic Adsorption, US Patent 5,159,816, 1992.

LaCava, A. I., V. A. Koss and D. Wickens. Non-Fickian Adsorption Rate Behaviour of some Carbon Molecular Sieves, *Gas Sep. Purif.*, 3, pp. 180-186, 1989.

Loughlin, K. F., M. M. Hassan, A. I., Fatehi and M. Zahur. Rate and Equilibrium Sorption Parameters for Nitrogen and Methane on Carbon Molecular Sieve. *Gas Sep. Purif.*, 7, pp. 264-273, 1993.

Liu, H. and D. M. Ruthven. Diffusion in Carbon Molecular Sieve, In Fundamentals of Adsorption, ed., by Levan, M. D., pp. 529-536. Boston: Kluwer Academic Publishers, 1996.

Ma, Y. H., W. Sun, M. Bhandarkar, J. Wang and Georg W. Miller. Adsorption and Diffusion of Nitrogen, Oxygen, Argon, and Methane in Molecular Sieve Carbon at Elevated Pressures, *Sep. Technol*, 1, pp. 90-98, 1991.

Malek, A. A Study of Hydrogen Purification from the Refinery Fuel Gas by Pressure Swing Adsorption, PhD Thesis, National University of Singapore, 1996.

Malek, A. and S. Farooq. Determination of Equilibrium Isotherms Using Dynamic Column Breakthrough and Constant Flow Equilibrium Desorption, *J. Chem. & Eng. Data*, 41 (1), pp. 25-32, 1996.

Mitchell, J. E. and L. H. Shedalman. A Study of Heatless Adsorption in the Model System Co in H. II, *AICHE Symp. Ser.,* 69, P. 25, 1973.

Nguyen, C. and D. D. Do. Dual Langmuir Kinetic Model for Adsorption in Carbon Molecular Sieve Materials, *Langmuir*, 16 (4), pp. 1868-1873, 2000.

Raghavan, N. S. and D. M. Ruthven. Simulation of Chromatographic Response in Columns Packed with Bidispersed Structure Particles, Chem. Eng. Sci., 40(5), pp.699-706, 1985.

Rao, MB and S. Sircar. Thermodynamic Consistency for Binary Gas Adsorption Equilibria, *Langmuir*, 15 (21), pp. 7258-7267, 1999.

Rege, S. U., and R. T. Yang. Kinetic Separation of Oxygen and Argon Using Molecular Sieve Carbon, *Adsorption* 6, pp. 15-22, 2000.

Reid, C. R., I. P. O'koye and K. M. Thomas. Adsorption of gases on carbon molecular sieves used for air separation, *Langmuir*, 14, pp. 3206-3218, 1998.

Ruthven, D. M. and RI Derrah. Diffusion of Monatomatic and diatomatic gases in 4A and 5A zeolite, *Faraday Transaction,* 1, 71, pp. 2031-2044, 1975.

Ruthven, D. M. Principles of Adsorption and Adsorption Applications, John Wiley & Sons, 1984.

Ruthven, D. M., N. S. Raghavan and M. M. Hassan. Adsorption and Diffusion of Nitrogen and oxygen in a Carbon Molecular Sieve, *Chem. Eng. Sci.*, 41, pp. 1325-1332, 1986.

Ruthven, D. M. Diffusion of Oxygen and Nitrogen in Carbon Molecular Sieve, *Chem. Eng. Sci.*, 47, pp. 4305-4308, 1992.

Ruthven, D. M., S. Farooq and K. S. Knaebel. Pressure Swing Adsorption, VCH Publishers, New York, 1994a.

Ruthven, D. M and S. Farooq. Concentration of a trace Component by Pressure Swing Adsorption, *Chem. Eng. Sci.*, 49, pp. 51-60, 1994b.

Rutherford, S. W. and D. D. Do. Adsorption Dynamics Measured by Permeation and Batch Adsorption Methods. *Chem. Eng. J.,* 76, pp. 23-28, 2000b.

Rynders, R. M., M. B. Rao and S. Sircar. Isotope Exchange Technique for Measurement of Gas Adsorption Equilibria and Kinetics, *AIChE J.*, 43, pp. 2456-2470, 1997.

Shin, H. S. and K. S. Knaebel. Pressure Swing Adsorption: A Theoretical Study of Diffusion-Induced Separation, AICHE J., 33, pp. 654-662, 1987.

Srinivasan, R., S. R. Auvil and J. M. Schork. Mass Transfer in Carbon Molecular Sieves- an Interpretation of Langmuir Kinetics, *Chem. Eng. J.*, 57, pp. 137-144, 1995.

Teague, K.G. and T. F. Edgar. Predictive Dynamic Model of a Small Pressure Swing Adsorption Air Separation Unit, *Ind. Eng. Chem. Res*, 38, pp. 3761-3775, 1999.

Wakao, N. and T. Funazkri. Effect of Fluid Dispersion Coefficients on Particle-to-Fluid Mass Transfer Coefficients in Packed Beds, *Chem. Eng. Sci*, 33, pp. 1375-1384, 1978.

Xu, J. and J. A. Hopkins. Process to produce oxygen and argon using devided argon column, US Patent 5,768,914, 1998.

Youshida, M., A. Kodama, M. Goto and T. Hirose. Enrichmentof a Trace Components in Air by PSA, the 4th China-Japan-USA Symposium on Advanced Adsorption Science and Technology, Guangzhou, China, 1997, pp.264-269.

Yuan, Y. X. Adsorption and Diffusion of Oxygen and Nitrogen in Carbon Molecular Sieve, Master Thesis, National University of Singapore, 1997.

Appendix: Collocation Form of the PSA Model Equations

The notations and definitions of the variables are in accordance with those used in the PSA program in FORTRAN codes.

A.1 Dimensionless Form of the PSA Model

Following dimensionless variables are defined:

$$X2 = \frac{c_A}{C_T} \ , \quad XAP2 = \frac{c_{AP}}{C_L} \ , \quad XBP2 = \frac{c_{BP}}{C_L} \ ,$$

$$X = \frac{z}{L} \ , \quad RX = \frac{R}{R_P}(particle) \quad or \quad \frac{r}{r_c}(micropore) \ , \quad V2 = \frac{v}{v_0}, \quad T = \frac{t}{L/v_0} \ ,$$

$$EM = \frac{1-\varepsilon_b}{\varepsilon_b} \ , \quad PV = \varepsilon_p,$$

$$PEM = \frac{v_0 L}{D_L} \text{ (PEL for low-pressure operations)},$$

$$DELTAH = \frac{k_f R_P}{\varepsilon_P D_P} \text{ (DELTAL for low-pressure operations)},$$

$$BETAH = \frac{D_P L}{R_P^2 v_0}\frac{P_L}{P} \text{ (BETAL for low-pressure operations)},$$

$$\overline{\overline{YA2}} = \frac{\overline{\overline{q_A}}}{q_s} \ , \quad \overline{\overline{YB2}} = \frac{\overline{\overline{q_B}}}{q_s}, \quad QC = \frac{q_s}{C_T}$$

$$YCA2 = \frac{q_A}{q_s} \ , \quad YCB2 = \frac{q_B}{q_s},$$

$$GAMMAA = \frac{D_{A0}^* / r_c^2}{v_0 / L} \ , \quad GAMMAB = \frac{D_{B0}^* / r_c^2}{v_0 / L}$$

It should be point out that only the spatial variables, *z*, *R* and *r*, must be made dimensionless for the use of orthogonal collocation method. Whether and how the other variables are made dimensionless depend on the clarity of physical meanings and

programming convenience. For example, column pressure is left to be of absolute pressure unit in the model.

Substituting the above definitions into Eq. 5.1, 5.1a, 5.1b, 5.2, 5.4, 5.4a, 5.4b, 5.5 and 5.13, the following dimensionless equations can be obtained:

Component mass balance equation and its boundary conditions

$$
\begin{cases}
\dfrac{\partial X2}{\partial T} = \dfrac{1}{PEM} \times \dfrac{\partial^2 X2}{\partial X^2} - X2 \times \dfrac{\partial V2}{\partial X} - V2 \times \dfrac{\partial X2}{\partial X} - EM \times \dfrac{\partial \overline{\overline{YA2}}}{\partial T} \times QC \\[4mm]
\left.\dfrac{\partial X2}{\partial X}\right|_{X=0} = -PEM \times V2|_{X=0}\left(X2|_{X=0^-} - X2|_{X=0^+}\right) \\[4mm]
\left.\dfrac{\partial X2}{\partial X}\right|_{X=1} = 0
\end{cases}
\tag{A.1}
$$

Continuity condition

$$
\sum X_i = 1
\tag{A.2}
$$

Overall mass balance equation and its boundary conditions

$$
\begin{cases}
\dfrac{\partial V2}{\partial X} = -EM \times \dfrac{\partial\left(\overline{\overline{YA2}} + \overline{\overline{YB2}}\right)}{\partial T} QC - \dfrac{1}{P}\dfrac{\partial P}{\partial T} \\[4mm]
V2|_{X=1} = 0 \quad or \\[4mm]
V2|_{X=0} = 1
\end{cases}
\tag{A.3}
$$

Adsorption term

$$
\dfrac{\partial \overline{\overline{YA2}}}{\partial T} QC = 3 \times BV \times BETAH \times \left.\dfrac{\partial XAP2}{\partial RX}\right|_{RX=1}
\tag{A.4a}
$$

$$
\dfrac{\partial \overline{\overline{YB2}}}{\partial T} QC = 3 \times BV \times BETAH \times \left.\dfrac{\partial XBP2}{\partial RX}\right|_{RX=1}
\tag{A.4b}
$$

Column mass balance

$$\frac{1}{P}\frac{dP}{dT} = V2\Big|_{X=0} - V2\Big|_{X=1} - EM \times \int_0^1 QC \times \left(\frac{\partial\left(\overline{\overline{YA2}} + \overline{\overline{YB2}}\right)}{\partial T}\right) dX \tag{A.5}$$

Macropore mass balance equation and its boundary conditions become:

$$\begin{cases} \dfrac{\partial XAP2}{\partial T} = BETAH \times \nabla^2 XAP2 - 3 \times GAMMAA \times QC\,\dfrac{1-PV}{PV} \times \\[2mm] \qquad \left[\dfrac{(1-YB2)\dfrac{\partial YA2}{\partial RX} + YA2\dfrac{\partial YB2}{\partial RX}}{1-YA2-YB2}\right]_{RX=1} \\[6mm] \dfrac{\partial XAP2}{\partial RX}\bigg|_{RX=1} = DELTAH\left[\dfrac{P}{P_L}X2 - XAP2\big|_{RX=1}\right] \\[4mm] \dfrac{\partial XAP2}{\partial RX}\bigg|_{RX=0} = 0 \end{cases} \tag{A.6}$$

Micropore mass balance equation and its boundary conditions become:

$$\begin{cases} \dfrac{\partial YA2}{\partial T} = \dfrac{GAMMAA}{1-YA2-YB2}\left[(1-YB2)\nabla^2 YA2 + YA2\nabla^2 YB2\right] + \dfrac{GAMMAA}{(1-YA2-YB2)^2} \\[2mm] \qquad \times\left[(1-YB2)\dfrac{\partial YA2}{\partial RX} + YA2\dfrac{\partial YB2}{\partial RX}\right]\left[\dfrac{\partial YA2}{\partial RX} + \dfrac{\partial YB2}{\partial RX}\right] \\[4mm] \dfrac{\partial YA2}{\partial RX}\bigg|_{RX=1} = \dfrac{b_A \times XAP2}{1/C_L + b_A \times XAP2 + b_B \times XBP2} \\[4mm] \dfrac{\partial YA2}{\partial RX}\bigg|_{RX=0} = 0 \end{cases} \tag{A.7}$$

A.2 Collocation Form of the Model Equations

Using orthogonal collocation method, the spatial differentials in the dimensionless equations are discretized, resulting in a set of ODEs in time and algebraic equations. The values of *X2, V2, RX, XAP2, XBP2, YCA2* and *YCB2* at collocation points form matrixes (in various dimensions) of the same names. The "2"s denote bed number.

Substituting Eq.A.3 and A.4 in Eq. A.1, the component mass balance equation and its boundary conditions become:

$$
\left\{
\begin{array}{l}
\dfrac{\partial X2(j)}{\partial T} = \displaystyle\sum_{i=1}^{M+2}\left(\dfrac{1}{PEM}\times BX(j,i) - V2(j)\times AX(j,i)\right)X2(j) \qquad (A.8) \\[2mm]
+\, 3\times EM \times PV \times BETAH \times \displaystyle\sum_{i=1}^{N1}\left[(X2(j)-1)A(N1,i)XAP(j,i) + X2(j)A(N1,i)XBP2(j,i)\right] \\[4mm]
\displaystyle\sum_{i=1}^{M2} AX(1,i)X2(i) = -PEM \times V2(1)\times(XFEED - X2(1)) \\[4mm]
\displaystyle\sum_{i=1}^{M2} AX(M2,i)X2(i) = 0
\end{array}
\right.
$$

Substituting Eq.A.4 to A.3, the overall mass balance equation and its boundary condition for the pressurization and blowdown steps become:

$$
\left\{
\begin{array}{l}
\displaystyle\sum_{i=2}^{M2} AH(j,i)V2(i) = -3\times EM \times PV \times BETAH \times \qquad (A.9a) \\[4mm]
\qquad\qquad \displaystyle\sum_{i=1}^{N1}\left[(X2(j)-1)A(N1,i)XAP(j,i) + X2(j)A(N1,i)XBP2(j,i)\right] \\[4mm]
V2(M2) = 0
\end{array}
\right.
$$

and for the high pressure adsorption step:

$$\left\{ \begin{array}{l} \sum_{i=1}^{M1} AY(j,i)V2(i) = -3 \times EM \times PV \times BETAH \times \\ \\ \qquad \sum_{i=1}^{N1} [(X2(j)-1)A(N1,i)XAP(j,i) + X2(j)A(N1,i)XBP2(j,i)] \\ \\ V2(0) = 1 \end{array} \right. \qquad \text{(A.9b)}$$

Substituting Eq.A.4 to A.5, the column mass balance equation becomes:

$$\frac{1}{P}\frac{dP}{dT} = V2(0) - V2(1) - 3 \times EM \times PV \times BETAH \times \qquad \text{(A.10)}$$

$$\sum_{j=2}^{M2} \frac{\sum_{i=1}^{N1} A(N1,i)[XAP2(j,i) + XBP2(j,i) + XAP2(j-1,i) + XBP2(j-1,i)]}{2 \times [X(j) - X(j-1)]}$$

Macropore mass balance equation and boundary conditions: (A.11)

$$\frac{\partial XAP2(j,k)}{\partial T} = BETAH \times P/P_L \times \sum_{i}^{N1} B(k,i)XAP2(j,i) - 3 \times GAMMAA \times \frac{1-PV}{PV} \times \frac{QCS}{C_L} \times$$

$$\left[\frac{(1 - YB2(j,k,N1))\sum_{i=1}^{N1} A(N1,i)YA2(j,k,i) + YA2(j,k,N1)\sum_{i=1}^{N1} A(N1,i)YB2(j,k,i)}{1 - YA2(j,k,N1) - YB2(j,k,N1)} \right]$$

$$\sum_{i=1}^{N1} A(1,i)XAP2(j,i) = 0 \qquad \text{(A.11a)}$$

$$\sum_{i=1}^{N1} A(N1,i)XAP2(j,i) = DELTAH \times \left[\frac{P_L}{P} XA2(j) - XAP2(j,N1) \right] \qquad \text{(A.11b)}$$

Micropore mass balance equation and its boundary conditions: (A.12)

$$\frac{\partial YA2(j,k,l)}{\partial T} = \frac{GAMMAA}{1-YA2(j,k,l)-YB2(j,k,l)}\left[\begin{array}{l}(1-YB2(j,k,l))\sum_{i=1}^{N1}B(1,i)YA2(j,k,i)+\\[2ex]YA2(j,k,l)\sum_{i=1}^{N1}B(1,i)YB2(j,k,l)\end{array}\right]+$$

$$\frac{GRAMMAA}{[1-YA2(j,k,l)-YB2(j,k,l)]^2}\left[\begin{array}{l}(1-YB2(j,k,l))\sum_{i=1}^{N1}A(1,i)YA2(j,k,i)+\\[2ex]YA2(j,k,l)\sum_{i=1}^{N1}A(1,i)YB2(j,k,i)\end{array}\right]\times$$

$$\left[\sum_{i=1}^{N1}A(1,i)YA2(j,k,i)+\sum_{i=1}^{N1}A(1,i)YB2(j,k,i)\right]$$

$$\sum_{i=1}^{N1}A(1,i)YA2(j,k,i)=0 \tag{A.12a}$$

$$YA2(j,k,N1)=\frac{b_A\times XAP2(j,k)}{\frac{1}{C_L}+b_A\times XAP2(j,k)+b_B\times XBP2(j,k)} \tag{A.12b}$$